UNIVERSITY
OF WOLLONGONG
AUSTRALIA

Synthetic Gauge Potentials for Light in Time-Dependent Media

Daniel Hey

This thesis is presented as part of the requirements for the conferral of the degree:

Bachelor of Science (Physics) (Honours)

Supervisor:
Dr. Enbang Li

The University of Wollongong
School of Physics

2017

Declaration

I, *Daniel Hey*, declare that this thesis is submitted in partial fulfilment of the requirements for the conferral of the degree *Bachelor of Science (Physics) (Honours)*, from the University of Wollongong, is wholly my own work unless otherwise referenced or acknowledged. This document has not been submitted for qualifications at any other academic institution.

———————————————————

Daniel Hey

October 20, 2017

Abstract

The principle of reciprocity ensures that the transfer of light is symmetric between any two points in both space and time. Non-reciprocal devices that are essential to modern photonics rely exclusively on magneto-optic materials, severely limiting their applicability. In this thesis, it is shown that the influence of a time-dependent medium on light can be described in terms of a gauge potential that is directly connected to the electromagnetic properties of the medium itself. This potential arises from the breaking of reciprocity, and is demonstrated through finite difference time and frequency domain simulations. It is shown how such gauge potentials can be exploited to demonstrate the Aharonov-Bohm effect for light, and a broadband optical isolator based on this technique is designed and numerically validated, showing complete non-reciprocal frequency conversion. For the isolator demonstrated here, an even mode is completely converted to an odd mode in the left to right direction whilst counter-propagating modes are not affected. In doing so, implementations of vastly more efficient finite difference methods are presented, with a two-fold order of magnitude improvement over time-domain simulations. By suitably tailoring the non-reciprocal phase, an emerging gauge field for light can be created which perfectly mimics the dynamics of charged particles in real magnetic fields. Such artificial fields allow for the demonstration of quantum effects typically associated with electrons, and as has been recently shown non-trivial topological properties of light.

Acknowledgments

Firstly, I would like to thank my supervisor Dr. Enbang Li for his advice and support throughout the writing of this thesis. I am grateful to Martin Morillas, for his patient oversight and induction of the Terahertz Imaging lab as well as his assistance in my experimental work.

I owe a great debt of gratitude to Dr. Shanhui Fan of Stanford University for his insightful comments and suggestions on my paper. Likewise, I am indebted to Dr. Jerry Shi who provided invaluable tips on implementing his numerical method, without which this thesis would not have been possible. My thanks also go to Dr. Ardavan Oskooi of the Ab Initio research group for answering my simulation questions as well as providing the immensely useful *MPB* band-structure program.

To my friends and family: I could not have done this without you. In particular, my parents Dorothy and Tony, who have continually supported me. I dedicate this thesis to my grandmother Helen Koletti, and hope she would have been proud.

Contents

List of Figures

List of Tables

Chapter 1

Introduction

Reciprocity is a fundamental principle governing transmission in physical systems. It ensures that the transfer of some physical quantity, such as light, motion, or even electrical charge is identical between any two points regardless of geometric asymmetries in the intervening space [1]. Physical intuition suggests that when reversing the position of a source and detector in some wave-like experiment, the observed signal will not change [2]. This principle holds for many physical systems, and in-fact many systems rely upon it - the detection of earthquakes [3], operation of interferometers, and even the identification of cracks in concrete [4], [5] exploit reciprocity to some degree. However, reciprocal transmission is not always a desirable trait in physical systems. There is growing demand for the ability to isolate a region of space to allow wave transmission in one direction, while blocking it in the other. Significant research has gone into searching for such techniques to induce non-reciprocity. Formally, a system is said to be non-reciprocal if it is asymmetric under time-reversal (*TR*) and parity-transformation (*PT*) symmetry. That is to say, a non-reciprocal system is one in which the laws governing it change when the direction of time and spatial locations is reversed ($t \rightarrow -t$, $r \rightarrow -r$) [6]. This is achieved by the application of an external force, such as a mechanical velocity or magnetic field which impose a preferential direction, or *bias*, on the system.

Reciprocity is not a property specific to light, but also one of numerous phenomena involving the transmission of wavelike phenomena - including acoustics and structural analysis. Both acoustic and mechanical non-reciprocity are active fields of research [1]. Such acoustic non-reciprocity forces sound to travel in one direction only, and has been borne from ideas originally formulated in electromagnetic non-reciprocity. Devices that exploit non-reciprocal wave transmission may lead to solutions to long-standing problems across many branches of physics - such as energy conversion, signal processing, and energy harvesting.
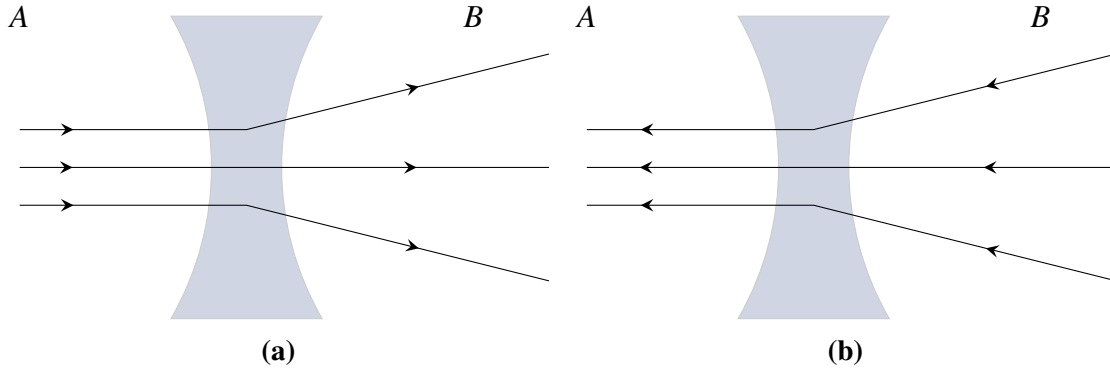
Figure 1.1: Reciprocity in a double concave lens for light rays travelling from **(a)** A to B, and **(b)** B to A. Since reciprocity holds for the system, light travelling along its time reversed path (B to A) will return back to its original state. This is true for *any* scattering event, not just the divergence of rays through a lens.

For electronic systems, breaking reciprocity relies on the existence of a magnetic field. Photons, however, are uncharged spin-1 Bosons and as a result there exists no naturally occurring gauge potential through which to control light. Manipulating the propagation of light at the nano-scale has been a long-standing hurdle in the development of integrated photonics [7]–[13]. With the development of artificial photonic structures such as photonic crystals and meta-materials [14], on-chip integrated photonics has been realised as not just a possibility, but increasingly more simple to achieve.

1.1 Reciprocity in electromagnetism

In electromagnetism reciprocity is known under the guise of *Lorentz reciprocity*, which mathematically expresses the idea of parity and time-reversal (PT) symmetry for an electromagnetic wave. In general terms, Lorentz reciprocity demands that if light can travel from some region *A* to another region *B*, then the reverse also holds (Fig 1.1). Consider for example the random scattering of a laser in a medium. If it were possible to selectively take all the scattered wavelets and reverse their direction, then reciprocity would ensure that the they would recombine back into a coherent beam that emerges at the original angle of incidence [15]. In other words, if the propagation of a light wave were to be reversed then the properties of its transmission would remain unaffected [16]. It is evident that this is a direct consequence of the more generalised form of reciprocity as described above, as reciprocity requires that waves which propagate along time-reversed paths exhibit identical properties of transmission, regardless of how complicated such a path might be [3].

Although reciprocal propagation of light is sometimes a desirable facet of optical devices, being able to dynamically constrain and manipulate the direction light can travel

has tremendously useful applications, ranging from the reduction of noise in optical experiments [17], to exhibiting novel quantum effects of light [18]. The most commonly employed method of breaking reciprocity in photonics is through the magnetic biasing of a system (where the magnetic field B is a pseudo-vector, making it odd under time-reversal [19]). In optics, magnetically biased techniques are crucial to the function of optical isolators, non-reciprocal devices that permit forward propagation of light while restricting counter-propagation [20], effectively constituting *diodes* for light. Such commercially available isolators make use of the magneto-optic Faraday effect, where the plane of polarisation of a light source is rotated along the path of its trajectory. However, practical implementation of the Faraday effect in integrated photonics remains largely infeasible, owing to the incompatibility of binding magneto-optic materials to standard metal-oxide semiconductors [21] as well as the difficulty in scaling to optical frequencies [22]. Additionally, since the rotation of the plane of polarisation is dependent on the path length the light travels through, any optical device constructed with this approach must be large enough to accommodate a sufficient rotation. These restrictions impose a fundamental limit on both the size and potential applications of non-reciprocal devices that make use of a magneto-optic biasing. Despite this, there is good reason why magneto-optics has remained the de-facto standard of non-reciprocal devices; magneto-optically active materials are inexpensive, widely available, and simple to work with, making them attractive from an engineering standpoint in devices where size limitations are not strictly enforced.

Small-scale compatibility of non-reciprocal optics forms a primary hurdle in the realisation of fully-fledged photonic circuits. This has motivated a significant amount of interest in searching for alternative methods for inducing non-reciprocity without bulk magneto-optics [23]–[26]. Being able to isolate signals from one another is crucial to integrated photonics, which are currently hampered by significant noise and backscattering, leading to coherent interference in experiments and noise-sensitive designs. Nature however, provides startlingly few options to break reciprocity for light. As of yet there are only three known classes of techniques that are non-reciprocal. These includes the aforementioned magneto-optic biasing, non-linearities of materials, and the use of media that possess a *time-dependence*.

1.1.1 Relation to time-reversal symmetry

In most literature, reciprocity and time-reversal symmetry are often used synonymously. Despite this being the case for a majority of reciprocal processes, there are several situations where a breaking of TR-symmetry does not imply a reciprocity violation. Lorentz reciprocity occurs when a wave satisfies a symmetry property that connects a scattering

process with the reversed one. However, this is a generalisation of the principle of TR-symmetry, and the two are not always interchangeable in the realm of optics. This is because Lorentz reciprocity relates input and output waves in pairs, irrespective of the presence (or lack thereof) of other waves in the system. For optical systems reciprocity can be applied even when absorption in a material takes place - a process that is TR asymmetric, but still reciprocal [16].

1.2   Non-reciprocity in time-dependent systems

Consider a glass of water with light incident upon its surface. Now, assume that the water is dispersionless, and to a large degree incompressible. As the light passes through the water, it will gain an overall phase shift while its other properties will remain unchanged. But what if the water is then set into motion? It is found that the light develops an interference structure that is dependent on the velocity of the medium [27]. Even coherent light - lasers, will slightly bend in their trajectory whilst passing through the water. The amount of dragging the light experiences is directly proportional to the velocity and refractive index of the medium, a phenomenon that has been well known since Fizeau's experiment (1851) on the speed of light in water. Most importantly however, the symmetry of light transmission in the water is non-reciprocal: a slight phase shift is acquired when the light propagates with the water flow. On the other hand, light propagating in the reverse direction will acquire a negative phase shift. This idea of a medium that possesses some kind of time-dependent bias forms an important class of non-reciprocal devices.

Lorentz reciprocity is derived on the grounds of time-independent media and time-harmonic fields [6]. It is apparent then that an optical medium that exhibits some kind of time-dependence can not be constrained by the reciprocity theorem. A moving medium will induce a non-reciprocal phase shift for light. This can be intuitively understood due to the flow vector v of the water being odd under time-reversal, akin to the pseudo-vector in magneto-optically active materials. The phase shifts obtained by the light are not directly observable. Similarly to how voltage can only be measured as a potential difference, the phase of light can only be measured relative to the phase of another electromagnetic wave. This measurement is exclusively made by examining the interference pattern of the light [28].

1.3   Outline

This thesis will focus primarily on non-reciprocity in time-dependent media, and discuss how such non-reciprocal phases give rise to a synthetic gauge potential for light. The

introduction of a gauge potential gives rise to a photonic analogue of the Aharonov-Bohm effect which is demonstrated through full-wave finite difference methods.

In Chapter 2, a review of recent developments in the field of synthetic gauge fields is presented. The review explores how non-reciprocal phases give rise to a photonic gauge field, and how suitable tailoring of the phases culminates in effective magnetic fields. These effective magnetic fields for light are vital in the nascent field of topological photonics.

Chapter 3 presents a theoretical derivation of the effective gauge potential arising from a moving medium - and how such motion is equivalent to a modulation of the permittivity of a waveguide. It is then shown how a photonic analogue of the Aharonov-Bohm effect can be demonstrated with a rotating dielectric medium and a modulated waveguide.

In Chapter 4, the finite-difference method for electromagnetic simulations is discussed and implemented for the purpose of demonstrating non-reciprocal phases in modulated waveguides. Both time and frequency domain simulations are considered.

Finally, in Chapter 5, non-reciprocal mode conversion is numerically validated and demonstrated, as well as a photonic Aharonov-Bohm effect for the purposes of optical isolation. Discussions of the feasibility of such devices is considered, and both implementations of numerical methods are then compared.

Chapter 2

Review of synthetic gauge fields in photonics[1]

To achieve fine-control over light one may use so-called synthetic gauge fields. A synthetic gauge field is the tailoring of specific conditions such that some quantity of neutral particles emulates the dynamics of charged particles in a magnetic field. The rotation of a trapping of neutral atoms constitutes one such field: the Coriolis force, $F_C = -2m\Omega \times v$ couples to the atoms in a manner analogous to the classical Lorentz force, $F_L = q(v \times B)$ [29]. Conversely, the mechanism for generating a synthetic gauge field for cold atoms relies on changing some internal degree of freedom to impart a phase to the wave function over time [30]. Similar synthetic gauge fields have also been explored in opto-mechanics [31], [32] and acoustics [33], [34]. This lends itself to the question of whether it is possible to achieve similar conditions for light, and has motivated significant research into the field of synthetic gauge fields in photonics [35], [36].

These synthetic gauge fields have proved instrumental in the nascent field of topological photonics, where a transfer of edifice from electronic systems has created a wealth of research ideas, ranging from the observation of protected edge states of light, where light moves along the edge of a system [37]–[41] to Floquet topological insulators, devices that are characterised by edge states immune to disorder [42]–[47]. In photonics, spatial periodicity of a lattice is combined with a synthetic gauge field, leading to 2D energy bands that are distinguished by the topological invariant known as the first Chern number. Suitable engineering of synthetic gauge fields thus has the potential to explore higher dimensional topologies, and the first experimental work on 3D lattices has unveiled particularly intriguing topological features, including the elusive Weyl points. Going further, recent work has begun on examining 4D topologically non-trivial effects of light [48].

---

[1]This chapter is reproduced in part with permission, from Hey & Li *"Advances in Synthetic Gauge Fields through Dynamic Modulation"* 2017, submitted to *Optics Communications* for publication.
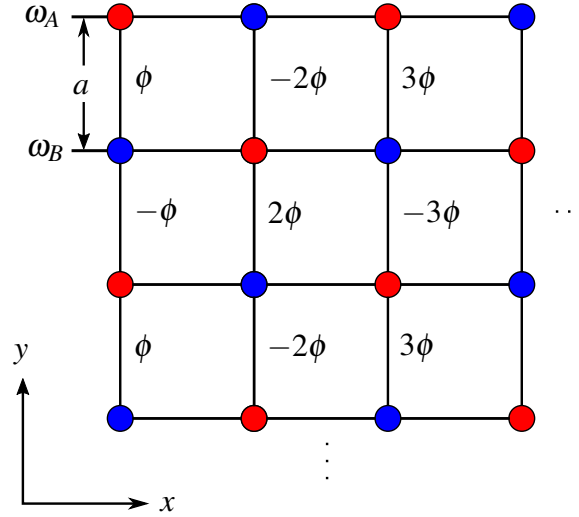
Figure 2.1: A 2D dynamically modulated lattice of photonic resonators, with two square sub-lattices of respective frequencies ω_A (red) and ω_B (blue). There is nearest neighbour coupling so that photons can only 'hop' between points via suitable modulation, acquiring a non-reciprocal phase. The phase on the horizontal bonds is 0 (not shown), whereas the phase on the vertical bonds is linearly proportional to the column index, with a sign flip every 2nd index. This modulation choice corresponds to the Landau gauge. Image re-drawn from [51].

2.1   Inducing a photonic gauge field

Originally, the concept of generating a synthetic gauge field for photons was limited to a static ring resonator lattice that is carefully engineered to impart direction-dependent phases to photons with opposite spins [49]. On a single dielectric ring, light will resonate when it constructively interferes with itself after making a full round-trip [50], in what are known as 'whispering gallery' modes, so named for their acoustic origin in St Paul's cathedral where whispered sounds propagate along the circumference of the circular interior. In a periodic array of these resonators, it is possible for photons to 'hop' between different rings, in a manner that is analogous to electrons tunnelling between atoms in a crystal. As a result, the edge modes of opposite spins propagate in opposite directions, realising a photonic analogue of the quantum spin Hall effect, a phenomena typically associated with electrons that is characterised by propagation only on the surface of a material. However, structures engineered in this way are susceptible to backscattering, since TR-symmetry is not broken.

By applying a *time-dependent* harmonic modulation to a photonic systems refractive index, it is possible to break this TR-symmetry and introduce a gauge field for light [51], as in Figure 2.1. This process, known as dynamic modulation was first conceived by Fang et al. and later extended to a network of resonating lattices [23]. In applying the modulation, the phase of light becomes direction-dependent. This phase is strictly non-
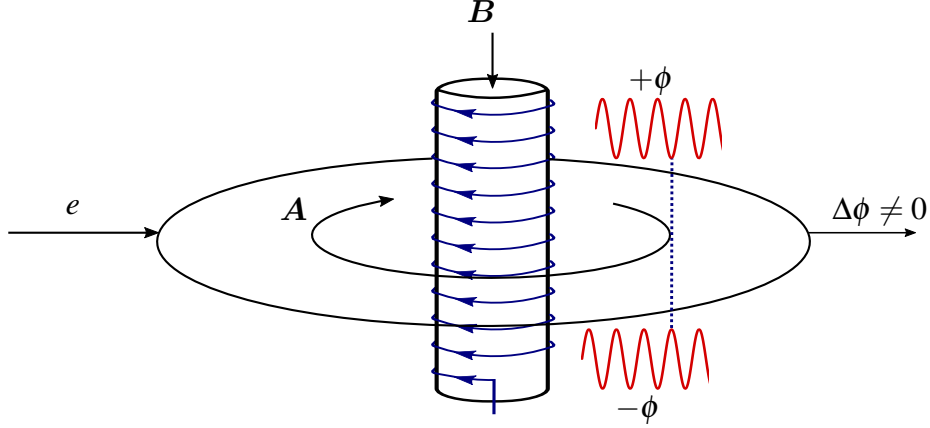
Figure 2.2: The Aharonov-Bohm effect for electrons. An infinitely long solenoid has its magnetic flux confined entirely within its core. Surrounding the cylinder, the **B** field vanishes but the magnetic vector potential **A** remains. The potential causes the electrons to gain a negative or positive phase depending on their path through the potential.

reciprocal, and consequently, possesses a broken TR-symmetry; reverting the direction of propagation will reverse the sign of phase. As far as the photon is concerned, the phase of some wave function cannot be directly measured, only differences in phase, and thus represents a gauge degree of freedom. This phase possesses the same gauge ambiguity as that of the phase acquired in an electronic gauge potential along an open path. Likewise, reverting the direction of propagation results in a change of sign. Consequently, this phase has the same properties as the electronic Aharonov-Bohm (AB) phase, so that demonstrating non-reciprocity is equivalent to showing the existence of a gauge potential for photons.

2.1.1   The electronic Aharonov-Bohm effect

Classically, for charged particles the AB effect is characterised by the acquisition of phase of a charged particle as it traverses a path-dependent potential where both the electric **E** and magnetic **B** fields vanish as in Figure 2.2 [52]. The magnetic vector potential of the fields is non-vanishing in this region and mediates interactions with the magnetic field. In circulating around the potential, the electron acquires a positive or negative phase which can only be observed through interference of both paths. The Aharonov-Bohm effect demonstrates the importance of the gauge potential in quantum systems, and in fact is a prerequisite for the existence of such potentials [52]. The AB effect has been widely demonstrated for electrons and other charged particles [53], however it was only recently shown by Fang et al. (2013) that the gauge potential from non-reciprocal phases of light can be exploited to demonstrate an optical equivalent to the AB effect for light at radio frequencies [54].

2.1.2 An effective magnetic field for light

Non-reciprocal phases of light in time-varying systems have been shown to give rise to an important phenomenon - effective magnetic fields for light. Fang et al (2012) first demonstrated that an effective magnetic field for light can arise if the phase of the light were non-reciprocal [23]. The effective magnetic field is directly linked to the idea of a gauge potential, similar to how the classical electromagnetic field B arises from the magnetic vector potential A. In fact, the non-reciprocal phase shift acquired by light in a moving medium discussed in the beginning of section 1.2 satisfies the requirements for generating a gauge potential. This is incredibly useful from an optical standpoint, as photons, being neutral particles, do not naturally couple to magnetic fields.

Fang et al. later went on to demonstrate that such effective magnetic fields can arise from the aforementioned dynamic modulation of a ring resonator lattice [55]. By imposing a specific arrangement of non-reciprocal phases for light in the structure, the resulting arrangement corresponds to a uniform magnetic field for light. Despite acknowledging the possibility of the harmonic modulation to give rise to any kind of directed effective field, Fang et al. only simulated a uniform field causing the light to move in circular motion. Additionally, practical creation of a lattice with the required levels of finesse are noted to be highly difficult from an engineering standpoint.

Other non-reciprocal phase induced fields also consider an array of resonators that impose a static direction dependent phase [56]. However, all of these suffer from a similar flaw - practical implementation of the resonators is incredibly difficult, and the final system is static in nature, in contrast to dynamically modulated systems. It has been noted by Lin and Fan (2015) that the resonators themselves provide no essential role with respect to the effective field generated, beyond simplifying the theoretical treatment [57]. As a result, they have derived a 'resonator-free' system that is based instead on a purely two-dimensional network of waveguides.

Resonators and waveguides are not the only methods of inducing a non-reciprocal phase (and consequently, a gauge potential for light). Li et al. (2014) demonstrated that photon-phonon interactions within acousto-optic crystals introduces a non-reciprocal phase for light [26]. From this, they demonstrated an optical Aharonov-Bohm effect at visible frequencies, one the first of such kind observed through non-reciprocal phases. The possibility of realising an effective magnetic field for photons gives rise to an important number of effects that are similar to phenomena exhibited by electrons in a magnetic fields, such as a Lorentz force [51], quantum Hall effects, and topologically protected one-way edge modes [55]. While some of these effects have been noted to be possible with magneto-optics [58], [59], dynamic modulation is both more versatile and offers a greater coupling strength at optical frequencies.

2.1.3 Fluid moving media

The idea of exploiting non-reciprocal phase shifts to demonstrate an AB effect has been naturally extended to the simpler cases of light in moving media. Vieira et al (2014) discussed an implementation for inducing non-reciprocal phases in light by submerging a rotating cylinder in a viscous medium. The rotation of the cylinder imparts an angular *biasing* to the medium, which creates a non-reciprocal phase for the light by mediating interactions between the cylinder and light in a manner similar to how the magnetic vector potential mediates interactions with the magnetic field [60]. In this method, the effective magnetic field for the light is given by the vorticity (the local rotation of the vector field) of the medium in which it is present, again similar to how the magnetic field is the curl (or vorticity) of the magnetic potential.

Vieira's result is not the first for wavelike phenomena in rotating media. It has previously been shown by de Rosny et al. (2005) that a rotational flow can break the reciprocal transmission of ultrasound waves, along with Leonhardt's [61]–[63] pioneering formulations of the effective gauge potentials for light. In Leonhardt's work, not only was a possible AB effect suggested, but it was also shown that a medium with high enough viscosity and refractive index can bend and trap light similarly to a black hole, a result that has been subsequently proven in multiple experiments [64].

2.2 Topological photonics

Dynamically modulated resonator lattices also support one-way propagation along the edges (edge modes). However, time-harmonic modulations of more than a few resonators simultaneously is a challenging feat at optical wavelengths [65]. Rechtsman et al. (2013) showed that it is possible to shift the modulation from the frequency to the spatial domain to observe photonic analogues of the quantum Hall effect at optical frequencies [66], corresponding to the first experimentally viable Floquet topological insulators [67]. Instead of breaking TR-symmetry in their system, the authors instead broke spatial symmetry along the *z*-axis, and identified their system as being suitably analogous to a breaking of TR-symmetry, culminating in protected edge modes.

Most previous works have focused solely on the regime where the modulation strength is far less than the modulation frequency [59], allowing for the application of the rotating-wave approximation (RWA), where slowly varying terms are ignored. On the other hand, there has been recent interest in light-matter interactions in the ultra-strong coupling regime [68], [69], where the RWA is no longer valid. In such ultra-strong coupling systems, it has been shown that topologically protected one-way edge states in dynamic modulation are less susceptible to intrinsic losses [36]. In addition to this, a unique topologi-

cal phase transition was found to be associated with variations in the modulation strength [70]. Such phase transitions are not found in rotating-wave counterparts.

2.2.1   Synthetic dimensions

Studies in topology have long hinted at rich possibilities of physics in higher dimensions, namely analogues of the quantum Hall effect in even-dimensional spaces [71]. Traditional systems in condensed matter physics however, are locked out of examining such effects. Only recently have new approaches in simulating higher dimensional topological models, so-called 'synthetic dimensions' have been proposed, that generate a gauge field for neutral particles by exploiting additional degrees of freedom [72]–[74]. These ideas were first proposed in ultra-cold atomic gases[75], [76], where the atoms possess an internal spin degree of freedom. Photons naturally possess many internal degrees of freedom: frequency, orbital angular momentum, spin angular momentum, polarization, and so on. These additional degrees of freedom can form synthetic lattice dimensions for light, leading to possible experimental analysis of higher dimensional topological photonics. Due to the long-range interactions of light in synthetic dimensions however, there is a difficulty associated with exploring quantum Hall effects [77], [78].

Here, a basic method of achieving synthetic dimensions via dynamic modulation is demonstrated. Consider one of the most elementary photonic structures - the ubiquitous ring resonator. In the absence of group velocity dispersion (where the group velocity depends on the wavelength), the single ring supports a set of equally spaced resonant frequencies. The spacing of the modes Ω is based on the spectral range of the resonator, and is related to the round-trip time T by $\Omega = 2\pi/T$.

By dynamically modulating the ring structure, as in Figure 2.3, modes on the ring undergo transitions to higher order sidebands, separated by the modulation frequency Ω_M. If the modulation frequency is then chosen to be equal to the mode spacing of the resonator Ω, there will be a resonant coupling of the modes that are separated by the free-spectral range of the ring (the frequency spacing naturally supported by the ring). Consequently, this system can be described by a *1D* tight-binding model, despite being a *0D* structure, as the spacing of the frequencies represent an additional degree of freedom for the light. This can naturally be extended to the case of a 1*D* array of ring resonators that are coupled together to form a waveguide [79]. Each ring has a controlled phase of modulation, which gives rise to *2D* physics model on a 1*D* structure. The phase of the modulation corresponds then to the hopping phase along the frequency axis.

It is possible to generate a topologically non-trivial bulk correspondence by considering boundaries in real and synthetic space. In real space, the boundary is given by the physical edges of the ring. However, in frequency space, a boundary is introduced by the group
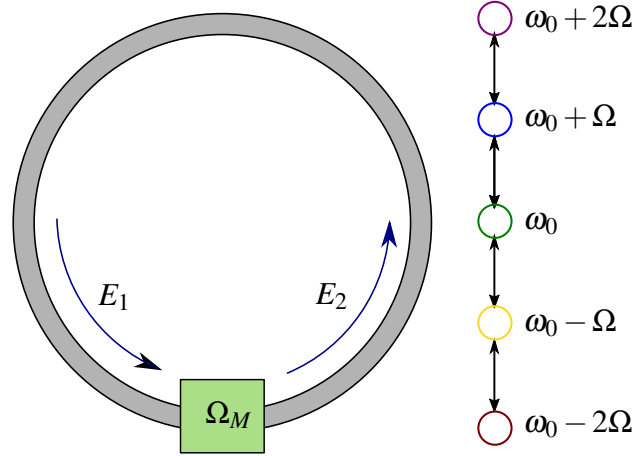
Figure 2.3: A ring resonator undergoing dynamic modulation of frequency Ω_M, which supports several equally spaced resonant modes. The resonator modes form a synthetic dimension along the frequency axis, and by transitioning the light between different frequencies, it is possible to examine *1D* physics on the *0D* ring structure. Although the light is propagating effectively in *3D* in the ring, the single mode can be considered to be point-like *0D*.

velocity dispersion (GVD) of the ring instead (how the ring affects the duration of optical pulses propagating within it). Around the zero-GVD point, most frequencies are equally spaced so the modulators induce an on-resonance coupling. On the other hand, away from the zero-GVD point, the frequencies are no longer equally spaced and thus cannot support coupling, leading to an effective *boundary* in frequency space. Thus, light propagating along the system will encounter a boundary composed of the real physical size of the rings in combination with the GVD. Finally, we note that outside of applications in topological photonics discussed below, synthetic dimensions in dynamic modulation have also recently been shown to support efficient frequency manipulation of light [80].

2.2.2 Weyl points

In condensed matter systems, the Weyl point describes a magnetic monopole in momentum space, that is, a 'source' or 'sink' of Berry curvature. As such, the Weyl point is perceived as topological nodal points in 3D momentum space. Weyl points are topologically robust, in the sense that they cannot be destroyed by any perturbation that preserves translational symmetry. The Hamiltonian of a Weyl system is $H = k_x\sigma_x + k_y\sigma_y + k_z\sigma_z + E_0 I$ where $\sigma_{x,y,z}$ are the Pauli spin matrices, and *I* is the *2x2* identity matrix, which together form a complete basis for *2x2* Hermitian matrices. There has been a massive effort devoted to investigating Weyl points and their associated phenomena in electronic systems [81], [82], and have also been found in photonic crystals [83], [84], as well as acoustic [85] and plasmonic structures [86].
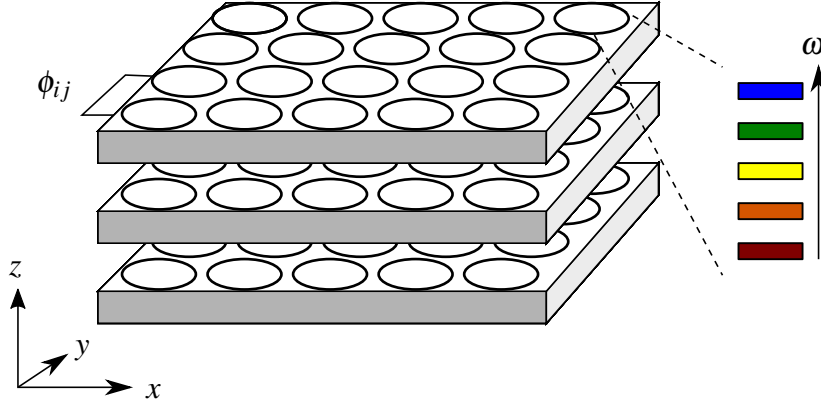
Figure 2.4: An example resonator structure for examining 4D topological photonics. Dynamic coupling between rings allows for 3D propagation. The supported frequencies of the resonators, ω, as usual provide the synthetic dimension allowing for the possibility of examining 4D topological physics with light.

To explore a Weyl point in a planar 2D geometry, one may use a synthetic dimension to simulate the third spatial dimension, by again considering arrays of ring resonators – this time arranged in a honeycomb lattice. The size of the synthetic dimension, which corresponds to the number of modes in each individual ring can be chosen to be almost arbitrarily large without increasing the system complexity. In a recent paper, Lin et al suggested that it is possible to investigate a synthetic 3D space through dynamic modulation of 2D on-chip ring resonators [87]. Each resonator supports a set of discrete modes equally spaced in resonant frequency. The synthetic dimension then originates from these discrete modes, manifesting as a synthetic periodic lattice so that the entire system can be envisaged as a 3D space. This on-chip dynamic modulation is readily feasible, as compared with previous complex electromagnetic or acoustic structures for realizing Weyl points [88], [89], a planar 2D approach is more flexible owing to the dynamic nature of the system, and can be achieved with the previously discussed extension of dynamic modulation in synthetic dimensions, allowing for on-chip investigation of Weyl points.

2.2.3   Towards 4D photonics

Naturally, the quantum Hall effect was first generalized to higher dimensions for electronic systems [71]. It is a standard extension of our discussion on 3D photonic systems to then consider a 3D array of resonators in the three spatial dimensions x, y, z and then extending into the synthetic frequency dimensions ω to probe elusive 4D quantum Hall effects.

A 4-dimensional model making use of 3D resonating lattices with plaquettes has only recently been proposed by Price et al., based on the authors previous works in 4D quantum Hall effects for ultra-cold atoms [90]. This model differs to a potential synthetic

dimension with dynamic modulation in Figure 2.4, as their lattice model does not break TR-symmetry. Because of this, photons with positive angular momentum can backscatter into states with a negative angular momentum. However, it has been noted that such backscattering can be minimised during fabrication [91]. Finally, we note that achieving a 4D topological effect for light would not only be possible under a dynamic modulation regime, but also would involve a broken TR-symmetry, leading to one-way edge modes propagating on the boundaries of a 3D frequency space.

Chapter 3

Gauge potentials in time-dependent media

From the previous chapter, the generation of a synthetic gauge *field* relies completely on the presence of a synthetic gauge *potential* which arises from the existence of non-reciprocal phases. Creating these phases for light invariably requires breaking reciprocity. Here, it is shown that the influence of the velocity field on light in a moving medium can be formulated in terms of a gauge potential, which will lead to observable measurements of a direction-dependent phase. The more constrained case of a potential arising from the motion of water in both a linear waveguide and surrounding a rotating cylinder dielectric will then be shown to act as an effective magnetic potential for light, introducing a non-reciprocal phase that can be exploited to demonstrate an optical analogue to the Aharonov-Bohm effect. This phase can also be generated through dynamic modulation of a waveguide, and the gauge potential emerging from such modulations is derived based on the work of Fang et al. [51].

3.1 Moving media

To show how a moving media forms an effective vector potential for light, first consider the curl components of Maxwell's equations for moving media without sources [92],

$$\nabla \times \boldsymbol{E} = -\frac{\partial \boldsymbol{B}}{\partial t}, \tag{3.1}$$

$$\nabla \times \boldsymbol{H} = \frac{\partial \boldsymbol{D}}{\partial t}. \tag{3.2}$$

Let $\boldsymbol{v}(\boldsymbol{r})$ represent the velocity field associated with the motion of a medium of re-

fractive index n, moving along $v\hat{x}$. Then, by taking a first order approximation of the Minkowski relations A.11 and A.12, where $\mathbf{v}/c \ll 1$,

$$\boldsymbol{B} = \mu\boldsymbol{H} - (n^2 - 1)\frac{\boldsymbol{v}}{c^2} \times \boldsymbol{E}, \tag{3.3}$$

$$\boldsymbol{D} = \varepsilon\boldsymbol{E} + (n^2 - 1)\frac{\boldsymbol{v}}{c^2} \times \boldsymbol{H}. \tag{3.4}$$

These relations allow us to rewrite the curl components of Maxwell's equations in the form

$$\nabla \times \boldsymbol{E} - \frac{\partial}{\partial t}\left[(n^2 - 1)\frac{\boldsymbol{v}}{c^2} \times \boldsymbol{E}\right] = -\frac{\partial}{\partial t}(\mu\boldsymbol{H}), \tag{3.5}$$

$$\nabla \times \boldsymbol{H} - \frac{\partial}{\partial t}\left[(n^2 - 1)\frac{\boldsymbol{v}}{c^2} \times \boldsymbol{H}\right] = -\frac{\partial}{\partial t}(\varepsilon\boldsymbol{E}). \tag{3.6}$$

To solve these equations explicitly, we shall assume the light in the media to be a monochromatic plane wave with electric and magnetic fields defined as

$$\begin{bmatrix} \boldsymbol{E}(\boldsymbol{r},t) \\ \boldsymbol{H}(\boldsymbol{r},t) \end{bmatrix} = \begin{bmatrix} \boldsymbol{E}(\boldsymbol{r}) \\ \boldsymbol{H}(\boldsymbol{r}) \end{bmatrix} e^{-i\omega t}, \tag{3.7}$$

which simplifies equations 3.5 and 3.6 to

$$\left(\nabla + i\omega(n^2 - 1)\frac{\boldsymbol{v}}{c^2}\right) \times \begin{bmatrix} \boldsymbol{E} \\ \boldsymbol{H} \end{bmatrix} = i\omega\begin{bmatrix} \mu\boldsymbol{H} \\ -\varepsilon\boldsymbol{E} \end{bmatrix}. \tag{3.8}$$

To elucidate the relationship between the quantum and classical approach used here, Equation 3.8 is multiplied by $-i\hbar$, where $\hbar$ is Planck's reduced constant to obtain

$$(\hat{p} + q\boldsymbol{v}) \times \begin{bmatrix} \boldsymbol{E} \\ \boldsymbol{H} \end{bmatrix} = \hbar\omega\begin{bmatrix} \mu\boldsymbol{H} \\ -\varepsilon\boldsymbol{E} \end{bmatrix}. \tag{3.9}$$

Straight-away, the quantum momentum operator can be identified: $\hat{p} = -i\hbar\nabla$, as well as the effective charge for the photon in the medium,

$$q = \frac{\hbar\omega}{c^2}(n^2 - 1). \tag{3.10}$$

This charge, q, forms the *effective* charge for the light in the medium. Furthermore, the relationship between the gauge potential $\boldsymbol{A}$ and flow vector $\boldsymbol{v}$ of the medium as simply

$$\boldsymbol{A}(\boldsymbol{r}) = \boldsymbol{v}(\boldsymbol{r}). \tag{3.11}$$
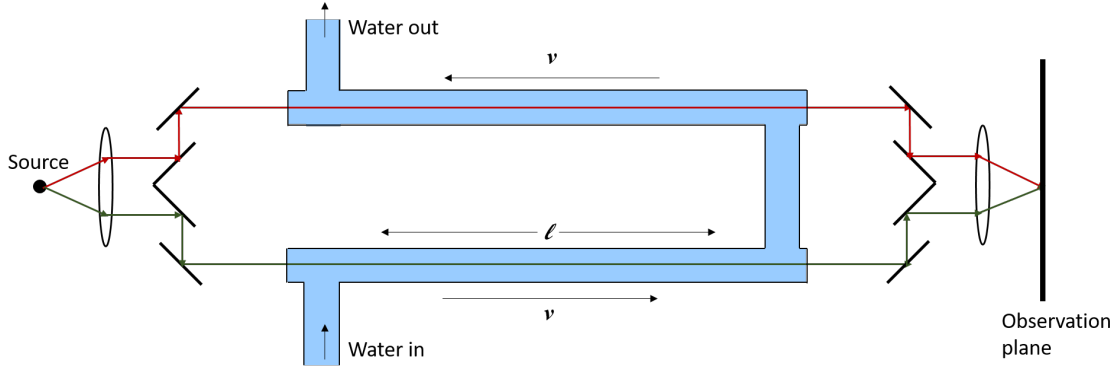
Figure 3.1: A traditional form of the Fizeau experiment. A source of light is split into two beams, propagating with and against the flow vector of the water respectively. The dragging of the light by the medium forms a non-reciprocal phase, which can be observed by the resulting interference pattern.

This result shows that a relative movement introduced in a medium can be formulated in terms of an effective vector potential, along with an associated 'charge' for the light in the medium.

3.1.1 Non-reciprocal phase from a Fizeau-like apparatus

Now, consider what happens if a photon were to flow through a medium moving with a linear velocity along *x*, as depicted in Figure 3.1. To derive the phase shift it will gain, we will begin with Maxwell's equations from 3.1 to 3.2. Rearranging the magnetic field intensity and displacement field, yields

$$\nabla \times \boldsymbol{E} = -\frac{\partial \boldsymbol{B}}{\partial t}, \tag{3.12}$$

$$\nabla \times \boldsymbol{B} = \mu\varepsilon\frac{\partial \boldsymbol{E}}{\partial t}. \tag{3.13}$$

Taking the curl of 3.12 yields,

$$\nabla \times (\nabla \times \boldsymbol{E}) = \nabla \times (-\frac{\partial \boldsymbol{B}}{\partial t}) = -\frac{\partial}{\partial t}(\varepsilon\mu\frac{\partial \boldsymbol{E}}{\partial t}), \tag{3.14}$$

where the divergence of the $\boldsymbol{E}$ field is 0, reducing the above equations to the three dimensional Cartesian form of the electromagnetic wave equation,

$$(\frac{n^2}{c^2}\nabla^2 - \frac{\partial^2}{dt^2})\boldsymbol{E} = 0. \tag{3.15}$$

Equation 3.15 transforms under the appropriate Lorentz boost along $v\hat{x}$, defined in Appendix A.4 as

$$\left[1 - \left(\frac{nv}{c}\right)^2\right]\nabla^2 \boldsymbol{E} - \frac{2}{c^2}(n^2 - 1)\boldsymbol{v} \cdot \nabla \frac{\partial E}{\partial t} + \left[\frac{v^2 - (nc)^2}{c^4}\right]\frac{\partial^2 E}{\partial t^2} = 0. \tag{3.16}$$

When the medium is moving slowly with respect to c we can assume $v/c \ll 1$, then the above equation further reduces to the more manageable form

$$\nabla^2 \boldsymbol{E} - \frac{2}{c^2}(n^2 - 1)\boldsymbol{v} \cdot \nabla \frac{\partial E}{\partial t} - \frac{n^2}{c^2}\frac{\partial^2 \boldsymbol{E}}{\partial t^2} = 0. \tag{3.17}$$

Again assuming a monochromatic plane wave solution (3.7) Equation 3.17 reduces to

$$\nabla^2 E - 2i\frac{w^2}{c^2}(n^2 - 1)\frac{\boldsymbol{v}}{c} \cdot \nabla E + (n\frac{w}{c})^2 E = 0. \tag{3.18}$$

Now, recall the time-independent Schrödinger equation for an electron in some potential $\boldsymbol{A}(\boldsymbol{r})$ [93],

$$\frac{1}{2m}\left(\frac{h}{i}\nabla - \frac{e}{c}\boldsymbol{A}\right)^2 \psi = E\psi \tag{3.19}$$

which can be expanded out to give

$$\nabla^2 \psi - \frac{ie}{\hbar c}\left[\boldsymbol{A} \cdot \nabla \psi + (\nabla \cdot \boldsymbol{A})\psi\right] + \left(\frac{2mE}{\hbar^2} + \frac{e^2}{\hbar^2 c^2}\boldsymbol{A}^2\right)\psi = 0. \tag{3.20}$$

By visual inspection alone, it is evident that equations 3.20 and 3.18 share a similar form in the low velocity regime to the first order, identical to our result in the previous section. To show this, consider the mapping of 3.20 to the following relations; $\psi \to E$, $\boldsymbol{A} \to \boldsymbol{v}/c$, $e/\hbar c \to k(n^2 - 1)$, and $2mE/\hbar^2 \to (nk)^2$, from which

$$\nabla^2 E - ik(n^2 - 1)\left[\frac{\boldsymbol{v}}{c} \cdot \nabla E + (\nabla \cdot \frac{\boldsymbol{v}}{c})E\right] + \left(n^2 k^2 + (k(n^2 - 1))^2\frac{\boldsymbol{v}}{c}\right)E = 0. \tag{3.21}$$

Which, in the first order approximation of $\mathbf{v}/c$ becomes Equation 3.18. Now, the known solution of the above expanded Schrödinger solution is simply

$$\psi(\boldsymbol{r}) = \psi_0 \exp\left[\frac{ie}{\hbar}\int^{s(\boldsymbol{r})} \boldsymbol{A}(\boldsymbol{r}') \cdot d\boldsymbol{s}'\right], \tag{3.22}$$

for a line integral over any path such that the final point $s(\boldsymbol{r}) = \boldsymbol{r}$ and the curl of $\boldsymbol{A}$ is vanishing.

The interference between two phases traversing different paths is then

$$\Delta\varphi = \frac{q}{\hbar}\left(\int_{P_1} \boldsymbol{A} \cdot d\boldsymbol{s} - \int_{P_2} \boldsymbol{A} \cdot d\boldsymbol{s}\right), \tag{3.23}$$

whereby application of Stoke's theorem,

$$\Delta\varphi = \frac{q}{\hbar}\int \nabla \times \boldsymbol{A} \cdot \hat{n}\mathbf{dS}, \tag{3.24}$$

which is the quantum AB effect for electrons. It is evident that this is also a solution for the interference of 3.18, where the electromagnetic vector potential $\boldsymbol{A}$ is replaced with $\boldsymbol{v}$,

$$\varphi = \frac{w}{c^2}(n^2 - 1)\int_S \nabla \times \boldsymbol{v} \cdot d\boldsymbol{S}. \tag{3.25}$$

If the velocity of the medium in both arms of the Fizeau apparatus is assumed to be uniform, then we can assume $\nabla \times \boldsymbol{v} = 0$ for both propagation paths of length l. In this case the interference term becomes

$$\varphi = \frac{\omega}{c^2}(n^2 - 1)(2vl). \tag{3.26}$$

Thus we see that not only does a moving media form a synthetic gauge potential for photons, but that such a potential imparts *direction dependent* phases on the light in question.

3.1.2 Photonic Aharonov-Bohm effect for a rotating dielectric

The potential is not constrained to exist only for linear motion. Here, it is shown that the rotation of a medium is sufficient to mimic the Aharonov-Bohm effect for light. The rotation of the medium forms an effective field that is synonymous with the rotation of the magnetic vector potential. In fact, the curl of the rotation itself gives rise to a gauge field, exactly how the magnetic field is the manifestation of the curl of the magnetic potential ($\boldsymbol{B} = \nabla \times \boldsymbol{A}$).

Consider first a dielectric cylinder of radius R, rotating with an angular velocity $\Omega\hat{z}$ while submerged in a uniform medium of constant viscosity as in Figure 3.2. Light traversing the medium will be shown to attain a non-reciprocal phase that is dependent on the radius and angular velocity of the dielectric, despite no interactions with the dielectric taking place. In the Aharonov-Bohm effect, the potential mediates interactions with the field. Here, the rotation of the medium instead mediates interactions with the dielectric cylinder [60].

The angular velocity imparted to the medium is proportional to the distance from the cylinder. In cylindrical coordinates (r, θ, z) the velocity of the cylinder and the surrounding medium is separated into two regions. One, for the inside of the cylinder ($0 \leq r \leq R$), and another for the medium surrounding the cylinder ($r > R$).
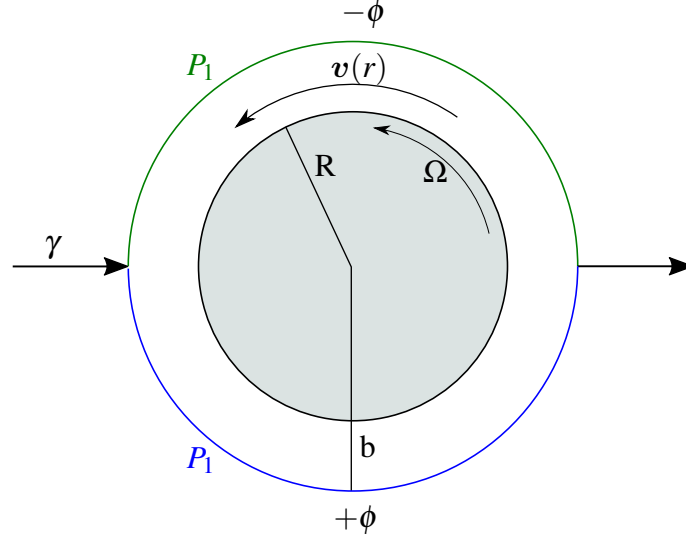
Figure 3.2: Proposed rotating cylinder for demonstrating an optical AB effect. A beam of photons is split into 2 paths, P_1 and P_2 of radius b, propagating around a rotating cylinder of angular frequency Ω immersed in a viscous medium. The light acquires a positive or negative phase depending on whether it is propagating with or against the rotation, leading to an optical AB phase.

$$v(r) = \begin{cases} \Omega r \hat{\theta}, & 0 \leq r \leq R \\ \dfrac{\Omega R^2}{r} \hat{\theta}, & r > R. \end{cases} \tag{3.27}$$

As such, there are two effective potentials dependent on the rotation of the cylinder. The effective field that the photon 'feels' is then

$$H = \nabla \times v = \begin{cases} \Omega \hat{z}, & 0 \leq r \leq R \\ 0, & r > R. \end{cases} \tag{3.28}$$

As expected, the effective field H is only non-vanishing inside the cylinder. Likewise, similar to electromagnetic fields, a vanishing of the magnetic field does not imply that the potential is also 0. In fact, the vector potential is not uniquely defined, since any number of arbitrary curl-free components can be added without changing the effective field. As long as the cylinder is rotating at a constant angular velocity, the strength of the effective field as 'felt' by the photon is independent of the position inside the cylinder.

Now, consider a light source propagating through the uniform medium surrounding the cylinder with respect to an observer in the rest frame (Fig 3.2. Surrounding the rotating cylinder, it has been shown that despite the effective magnetic field vanishing, an effective gauge potential of $\frac{\Omega R^2}{r} \hat{\theta}$ remains. Suppose that the packet of light is split into two separate paths of radius b, with path 2 (P_1) propagating in the direction of rotation, and path 1 (P_2) propagating along the opposite direction. In propagating along these paths, the wave-

function of the light acquires a phase,

$$\phi_{1,2} = \frac{q}{\hbar} \int_{P_{1,2}} A \cdot dr. \tag{3.29}$$

So that the relative phase shift of the light along the paths P_1 and P_2, which both share the same initial and final points, is given by

$$\Delta\phi = \frac{q}{\hbar} \int_{P_1} A \cdot dr - \frac{q}{\hbar} \int_{P_2} A \cdot dr = \frac{q}{\hbar} \oint A \cdot dr. \tag{3.30}$$

An important distinction to make in the above equations is that they are independent of the time taken to traverse the closed path. In other words, a photon moving at close to the speed of light will acquire exactly the same phase as a photon travelling significantly slower. Upon substitution of appropriate quantities, where q is the effective charge of the photon derived in Equation 3.10,

$$\phi = \frac{\omega}{c^2}(n^2 - 1) \int_0^{2\pi} \frac{\Omega R^2}{b} \hat{\theta} \cdot b d\theta \hat{\theta}. \tag{3.31}$$

Explicitly calculating this phase difference yields the result

$$\phi = \frac{2\pi\omega}{c^2}(n^2 - 1)\Omega R^2, \tag{3.32}$$

where n is the refractive index of the medium. That is, the phase difference of the interfering light is dependent on several properties of the dielectric cylinder. This result is exceedingly similar to the result for the linearly moving medium. The water still plays the same role as that of an effective potential, however the vorticity is no longer vanishing, and represents instead the effective field of the medium.

It is important to reiterate that both these processes are strictly non-reciprocal. Consider instead injecting photons from the right-hand side and measuring interference at the left. The photons previously propagating along the direction of rotation will now be circulating opposite to the media, and gain a negative phase shift. The phases of the light ϕ_1 and ϕ_2 impose a gauge potential for the photons. For a single photon, the phase of a single electromagnetic wave is not observable, representing a gauge degree of freedom. The phase obtained from the line integral of the gauge potential in the electronic AB effect has the same ambiguity. The phase difference between two paths however, is a detectable quantity through interferometry. Moreover, reverting the direction of propagation of the photons results in the change of the sign of the phase difference. Because of this, demonstrating the non-reciprocal phase is equivalent to a demonstration of the gauge potential for photons.
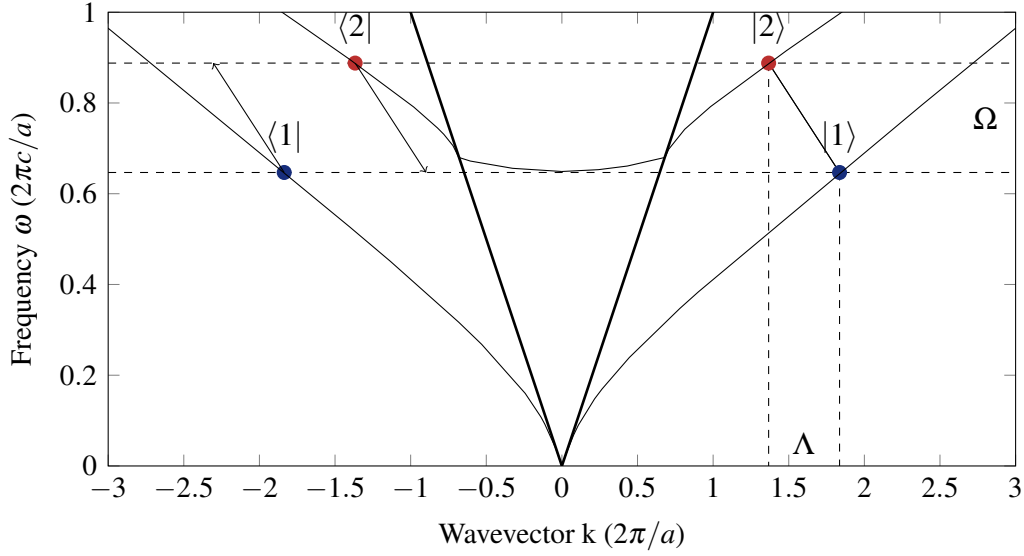
Figure 3.3: An example dispersion relation for the first two transverse electric bands in a waveguide, demonstrating a transition between modes $|1\rangle$ and $|2\rangle$. a is a normalisation constant set to $1\mu m$. The black $\omega = ck$ lines represent the light-cone. Any mode that exists near or between these lines are known as 'leaky' modes. To shift the wavevector, the phase-matching condition requires a spatial modulation of $\Lambda = k_1 - k_2$, whereas a shift in frequency requires a temporal modulation $\Omega = \omega_2 - \omega_1$. In the backward ($\langle 1|$) and time-reversed ($\langle 2|$) directions the modulation does not match any pairs of modes with each-other, so no transition can occur.

3.2 Dynamically modulated photonic structures

The question of dynamic media is subtle - what truly constitutes motion? The movement of a dielectric medium is an obvious one, but perhaps more subtle is the modulation of the refractive index of a medium in which light is propagating. As far as a photon is concerned, a moving medium is nothing more than a region of space in which the refractive index is time-dependent. In materials of unity permeability, the refractive index is simply $n = \sqrt{\varepsilon}$. Thus, by applying a time-dependent change to the permittivity of a photonic structure, the refractive index also becomes time-dependent.

All photonic structures possess a dispersion relation, which is a collection of wavevectors k and frequencies ω of allowed solutions to Maxwell's equations for a given set of boundary conditions. The dispersion relation dictates which *modes* of light are allowed to propagate, and are separated into their component transverse electric TE and transverse magnetic TM. Here, only TE modes are considered, so that the first two bands on the dispersion relation are the TE_0 even and TE_1 odd modes as seen in Figure 3.3. Modes that exist below the light cone of $\omega = ck$ are known as guided, whereas those in the light cone are 'radiation' or 'leaky' modes, so named for the exponential loss of the electric field of the mode as it propagates in the waveguide.

3.2.1 Interband transitions through permittivity modulations

When a photonic system is subject to a *time-dependent* modulation of its refractive index, the propagating modes of light can undergo what are known as interband transitions, in a manner analogous to electronic transitions in semiconductors [94]. These transitions cause the mode to jump between bands on the dispersion relation.

Consider a slab waveguide of permittivity ε with light propagating along the x direction. The waveguide supports two bands of transverse electric (so that the non-vanishing fields are E_z, H_x, H_y [1]) modes, with an even and odd symmetry with respect to the centre of the waveguide. An interband transition between two modes on these bands, $|1\rangle$ and $|2\rangle$ with frequencies and wavevectors (ω_1, k_1), (ω_2, k_2) located in these two bands can be accomplished by modulating a section of a waveguide with an additional dielectric perturbation

$$\varepsilon(x,t)' = \delta \cos(\Omega t + \Lambda x) \tag{3.33}$$

where $\Omega = \omega_2 - \omega_1$ is the frequency of modulation, δ is the strength of the modulation, and $\Lambda = k_1 - k_2$ is the difference in wavevectors. Note that here, bra-ket notation is used for the mode pairs, so that $TE_0 \equiv |1\rangle$ and $TE_1 \equiv |2\rangle$. Two types of transitions are possible: direct, where the initial and final mode exist at the same wavevector on different bands, or indirect, where the modes are on different bands and wavevectors. The transition is not instantaneous - rather it occurs as the photon traverses the length of the region being modulated. Indeed, if the modulated region is not large enough to completely transition the modes (this length is the *coherence length L_c*), then the mode only partially transition. For simplicity, assume that the transition occurs only between these two modes so that inside the modulated region of the waveguide, the electric field is a superposition of both modes,

$$E(x,y,t) = a_1(x)E_1(y)e^{-i(k_1 x - \omega_1 t)} + a_2(x)E_2(y)e^{-i(k_2 x - \omega_2 t)} \tag{3.34}$$

where $E_{1,2}(y)$ are the modal profiles normalised such that $|a_n|^2$ is the photon number flux carried by the nth mode. By substituting the above equation into Maxwell's equations, the coupled-mode equation describing transitions between two modes can be determined [95],

$$\frac{d}{dx} \begin{bmatrix} a_1 \\ a_2 \end{bmatrix} = \begin{bmatrix} 0 & iCe^{-(i\Delta kx)} \\ iCe^{(i\Delta kx)} & 0 \end{bmatrix} \begin{bmatrix} a_1 \\ a_2 \end{bmatrix} \tag{3.35}$$

---

[1]Here, TE refers to a non-vanishing E_z, H_x and H_y field components, propagating along x. Although commonly referred to as the TM modes, this choice is standard in the field of nanophotonics.

where the coupling strength

$$C = \frac{\varepsilon_0}{8} \int_{-\infty}^{\infty} \delta(x) E_1(x) E_2(x) dx. \tag{3.36}$$

By assuming the amplitude of the first mode at time $t = 0\,s$ is normalised to unity, and the amplitude of the second mode vanishes, Equation 3.35 can be solved to yield

$$a_1(x) = e^{-ix\Delta k/2} \cos(x\eta) + \frac{i\Delta k/2}{\eta} \sin(x\eta), \tag{3.37}$$

$$a_2(x) = ie^{-ix\Delta k/2} \frac{C}{\eta} \sin(x\eta), \tag{3.38}$$

where $\eta = \sqrt{C^2 + (\Delta k/2)^2}$. In the case where the transition is perfectly phase-matched ($\Delta k = 0$), η reduces to the coupling strength C, and so a photon in mode $|1\rangle$ will transition completely to $|2\rangle$ after propagating a distance of $L_c = \pi/2|C|$. When a strong phase mismatch occurs ($\Delta k \gg 0$), the transition can not occur.

The behaviour of an indirectly modulated system is strongly non-reciprocal. The modulation of the permittivity does not phase-match the mode at $|1\rangle$ with any other mode of the system in the reverse direction ($-k$) as seen in Figure 3.3. Thus, while $|1\rangle$ can undergo a complete photonic transition in the forward direction, its time-reversed $\langle 2|$ and parity transformed $\langle 1|$ counterparts are not affected at all. This non-reciprocity arises from the breaking of both PT and TR symmetries - the permittivity modulation is not invariant with either $t \rightarrow -t$ or $x \rightarrow -x$.

It is worth pointing out that a time-reversal operation on a mode is equivalent to a phase conjugation - that is, a time-reversed wave has its wavevector flipped ($k \rightarrow -k$). This only differs from the property of parity transformation by the fact that the TR wave is the reversed output of the original mode after undergoing a transition [96]. For example, consider an indirect transition from mode $|1\rangle$ at (ω_1, k_1) to $|2\rangle$ at (ω_2, k_2). To test time-reversal, the output mode $|2\rangle$ must be flipped around and re-injected from it's point of exit, so that the time reversed wave of (ω_1, k_1) is $(\omega_2, -k_2)$. These are summarised in Table 3.1.

Direction	$|1\rangle$	$|2\rangle$
Left to right (LR)	(ω_1, k_1)	(ω_2, k_2)
Right to left (RL)	$(\omega_1, -k_1)$	$(\omega_2, -k_2)$

Table 3.1: Mode frequencies and wavevectors for transverse electric modes propagating along x. A parity transformation (spatial inversion) flips the wavevector around, whilst a time-reversal operation flips the wavevector of the output mode.
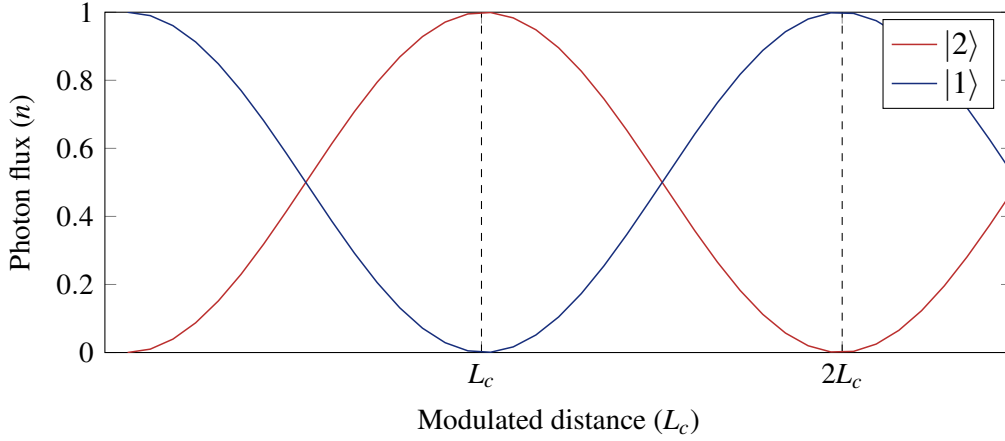
Figure 3.4: Modal evolution for multiple coherence lengths. Assuming no losses, the modes will completely transition every integer multiple of the coherence length. Even with an additional phase added to the modulation, the transitions themselves will not physically change, a manifestation of the gauge invariance of the modulation.

3.2.2 The gauge potential emerging from modulation

Consider now a direct transition so that the modulation has no spatial dependence ($\delta\cos(\Omega t)$). If the modulation is applied to the entire length of a waveguide, a mode injected in state $|1\rangle$ will harmonically transition to state $|2\rangle$ after passing through one coherence length (L_c). If this modulation is extended *beyond* the coherence length, the modes will continue transitioning back and forth, as in Figure 3.4.

However, there is an ambiguity in choosing the time-origin of the modulation. The act of shifting the modulation in time by an amount t_0 incorporates an additional phase factor into the modulation,

$$\varepsilon'(t) = \delta\cos(\Omega(t-t_0)) = \delta\cos(\Omega t + \phi). \tag{3.39}$$

The phase ϕ represents a gauge degree of freedom in the modulation, since adjusting the time-origin (a gauge transformation) does not affect the underlying physics in the mode evolution. That is, Figure 3.4 will not change regardless of the phase of the modulation and represents a gauge invariance. Both modes will continually transition between each-other in exactly the same shape. In the case of a direct transition with an additional modulation phase, Equation 3.35 becomes

$$i\frac{d}{dx}\begin{bmatrix} a_1 \\ a_2 \end{bmatrix} = \begin{bmatrix} 0 & Ce^{-(i\phi)} \\ C^\star e^{(i\phi)} & 0 \end{bmatrix}\begin{bmatrix} a_1 \\ a_2 \end{bmatrix}. \tag{3.40}$$

Thus, an upward transition from $|1\rangle \to |2\rangle$ will impart a positive phase ϕ, whereas a downward transition from $|2\rangle \to |1\rangle$ imparts a $-\phi$ phase. This is in direct analogy

to a tight-binding model of electrons on a lattice [97]. To show this, let i and j represent separate electron sites on a $1D$ lattice, with $b_{i,j}^\dagger$ and $b_{i,j}$ being the creation and annihilation operators of the electrons at their respective sites. Without a magnetic field and assuming no interaction terms, the Hamiltonian is given by

$$H = C_{i,j}b_i^\dagger b_j + C_{j,i}b_j^\dagger b_i, \tag{3.41}$$

where $C_{i,j}$ and $C_{j,i}$ are the 'hopping' coefficients between sites i, j. In the presence of a magnetic field with corresponding vector potential $\boldsymbol{A}$, the Hamiltonian undergoes a gauge transformation [98] to

$$H' = C_{i,j}\exp(i\frac{e}{\hbar}\int_j^i \boldsymbol{A}\cdot d\boldsymbol{l})b_i^\dagger b_j + C_{j,i}\exp(i\frac{e}{\hbar}\int_i^j \boldsymbol{A}\cdot d\boldsymbol{l})b_j^\dagger b_i. \tag{3.42}$$

In this case, the exponent terms are associated with a constant phase ϕ (the AB phase),

$$H' = C_{i,j}e^{i\phi}b_i^\dagger b_j + C_{j,i}e^{-i\phi}b_j^\dagger b_i, \tag{3.43}$$

so that the phase can be linked with the vector potential through

$$\frac{e}{\hbar}\int_i^j \boldsymbol{A}\cdot d\boldsymbol{l} = \phi. \tag{3.44}$$

Similarly, for the coupled-mode equations 3.40, the corresponding Hamiltonian for the photonic system is given by

$$H = Ce^{-i\phi}a_1^\dagger a_2 + Ce^{i\phi}a_2^\dagger a_1, \tag{3.45}$$

where $a_{1,2}^\dagger$ and $a_{1,2}$ are creation and annihilation operators for the photons in states $|1\rangle$ and $|2\rangle$. This is directly equivalent to the tight-binding Hamiltonian of the electronic system in Equation 3.41 - the photonic gauge potential can be made explicit by associating

$$\int_1^2 \boldsymbol{A}\cdot d\boldsymbol{l} = \phi, \tag{3.46}$$

where 1 and 2 represent the spatial locations of the photonic states $|1\rangle$ and $|2\rangle$ respectively[1]. Importantly, since the line integral of equation 3.46 depends on the direction of propagation, reversing the location of photonic states flips the sign of phase, which shows that a temporal modulation of a permittivity is sufficient to impart a direction dependent phase. Now, consider the device of Figure 3.5, consisting of two waveguides coupled together through a dynamic modulation which induces a transition between photonic states $|1\rangle$ and $|2\rangle$. Both upwards and downwards paths are physically passing through the same

[1]Although quantum mechanical in nature, the spatial locations of these photonic states can simply be defined as the centre the photon distribution
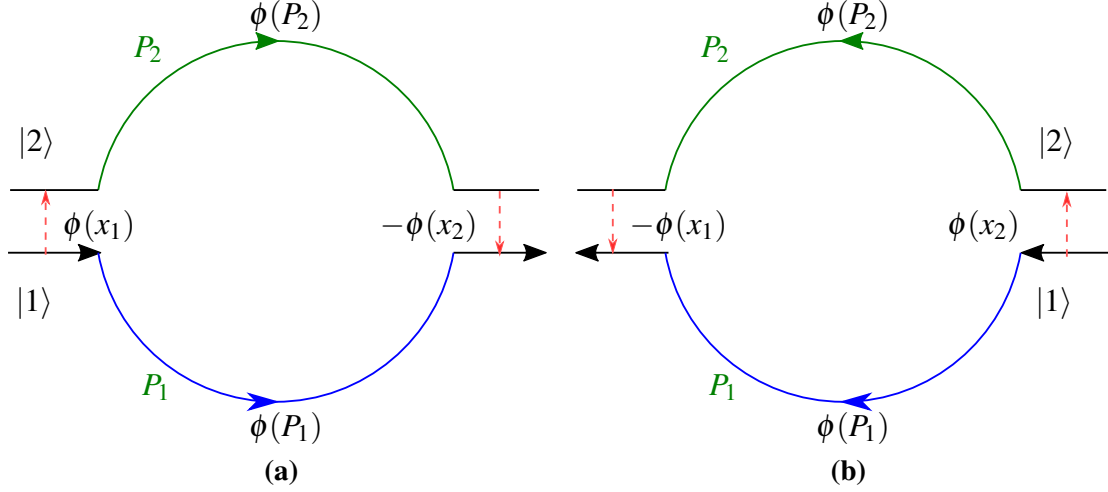
Figure 3.5: The Aharonov-Bohm effect for either photonic states $|1\rangle$ and $|2\rangle$ in the **(a)** forward and **(b)** time-reversed paths. The structure consists of two waveguides, coupled together through a dynamic modulation (dashed red) that induces a photonic transition between states which imparts an additional phase. Image re-drawn from [55].

space, however it is possible to choose different phases for different states along the path. The left hand side is modulated with an additional $\phi(x_1)$ phase, whereas the right hand side is modulated with a $-\phi(x_2)$ phase. For a photon of state $|1\rangle$ injected in the left waveguide coupler, there are two paths it can follow. In the first path, the photon is transitioned to a state $|2\rangle$, propagates along the upper arm in path P_2, and transitions back to $|1\rangle$ on the right. In doing so, it acquires a total phase

$$\phi = \int_1^2 \boldsymbol{A}(x_1) \cdot d\boldsymbol{l} + \phi(P_2) - \int_1^2 \boldsymbol{A}(x_1) \cdot d\boldsymbol{l}. \tag{3.47}$$

If no modulation is initially applied to the photon, it will remain in state $|1\rangle$ and propagate along the lower path of the interferometer, acquiring only a phase of $\phi(P_1)$. Because of this, the phase difference between both pathways is

$$\Delta\phi = \phi(P_2) - \phi(P_1) + \int_1^2 \boldsymbol{A}(x_1) \cdot d\boldsymbol{l} - \int_1^2 \boldsymbol{A}(x_1) \cdot d\boldsymbol{l}. \tag{3.48}$$

The line integral is free to be chosen such that it is non-vanishing only at the waveguide couplers, so that

$$\int_1^2 \boldsymbol{A}(x_1) \cdot d\boldsymbol{l} - \int_1^2 \boldsymbol{A}(x_1) \cdot d\boldsymbol{l} = \oint \boldsymbol{A} \cdot d\boldsymbol{l} = \phi(x_1) - \phi(x_2). \tag{3.49}$$

This phase difference is identical to the phase difference in the AB effect. On the time-reversed path (Fig 3.5b), the phase difference is instead $\phi(x_2) - \phi(x_1)$. The only physically observable quantity is then non-reciprocal.

Chapter 4

Numerical methods in nanophotonics

To numerically analyse the non-reciprocity of dynamically modulated structures, a method is required to solve Maxwell's equations for arbitrary permittivity distributions. In almost every case, the electromagnetic problems presented here are difficult, if not impossible to solve analytically. Usually only simple geometries can be considered. Thus, we turn our attention towards numerical solutions instead - namely the finite difference methods, which are a broad class of numerical techniques that solve differential equations by approximating derivatives between finite differences [99].

The finite difference method replaces all partial derivatives in a differential equation by *approximations*. For a 1D function, this can be done by taking the gradient between two points separated by h

$$\frac{\partial f(x)}{\partial x} = \lim_{h \to 0} \frac{f(a+h) - f(a)}{h} \approx \frac{f(a+h) - f(h)}{\Delta h}, \tag{4.1}$$

where the accuracy increases as Δh approaches 0. For electromagnetic fields however, the $\boldsymbol{E}$ and $\boldsymbol{H}$ fields are coupled by nature of Maxwell's equations. To discretise these fields in space, the fields are staggered on a 2D grid structure known as the Yee grid [100], where the electric and magnetic field components are stored at set i, j points on the grid. As shown in Figure 4.1a, the Yee algorithm centres its $\boldsymbol{E}$ fields on the faces of a square (in 2D TE), and its $\boldsymbol{H}$ fields on the edges. This choice ensures that every $\boldsymbol{E}$ field component is surrounded by four circulating $\boldsymbol{H}$ components [101], naturally satisfying the divergence free conditions.

In deriving these finite differences, the simulation is first assumed to be in 2D such that $\partial_z = 0$. Likewise, only the transverse electric (non-vanishing E_z, H_x, and H_y) propagation is considered, and the permeability and permittivity tensors are assumed to be diagonally anisotropic ($\mu_{lm} = \varepsilon_{lm} = 0$ if $l \neq m$). From this, the curl components of Maxwell's equations,

(a) **(b)**
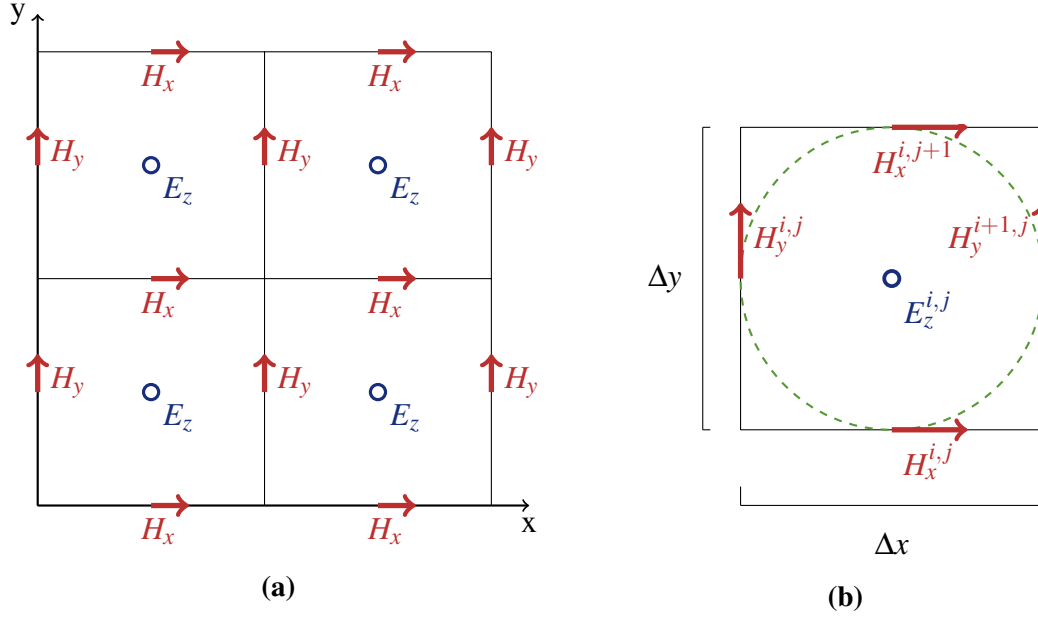
Figure 4.1: a) Yee grid placement of non-vanishing E_z (blue) and H_x, and H_y (red) fields. **b)** A single cell of the Yee grid, with coordinate placements of the fields. The H field is shown to naturally satisfy the divergence free condition. Likewise, the E_z field sits in the exact centre of the curl.

$$\nabla \times \boldsymbol{E}(\boldsymbol{r},t) = -\mu \frac{\partial \boldsymbol{H}(\boldsymbol{r},t)}{\partial t}, \tag{4.2}$$

$$\nabla \times \boldsymbol{H}(\boldsymbol{r},t) = \varepsilon \frac{\partial \boldsymbol{E}(\boldsymbol{r},t)}{\partial t}, \tag{4.3}$$

can be fully vectorised,

$$\partial_y E_z = -\mu_{xx} \partial_t H_x, \tag{4.4}$$

$$\partial_x E_z = \mu_{yy} \partial_t H_y, \tag{4.5}$$

$$\partial_x H_y - \partial_y H_x = \varepsilon_{xx} \partial_t E_z. \tag{4.6}$$

The partial derivatives are calculated by taking finite differences on the Yee grid, as in Figure 4.1b. The notation used here for a single point on the Yee grid is given as $(i,j) = (i\Delta x, j\Delta y)$ where Δ is the spatial discretisation. Further, any function f evaluated at some discrete point is referred to as $f(i,j) = f^{i,j}$, so that the spatially finite differences take the form

$$\partial_y E_z = C_x^E|^{i,j} = \frac{1}{\Delta y}(E_z^{i,j+1} - E_z^{i,j}), \tag{4.7}$$

$$\partial_x E_z = C_y^E|^{i,j} = \frac{1}{\Delta x}(E_z^{i+1,j} - E_z^{i,j}), \tag{4.8}$$

$$\partial_x H_y - \partial_y H_x = C_z^H|^{i,j} = \frac{1}{\Delta x}(H_y^{i,j} - H_y^{i-1,j}) - \frac{1}{\Delta y}(H_x^{i,j} - H_x^{i,j-1}), \tag{4.9}$$

where C is used to refer to the curl component of the field at the i, j point on the grid.

4.1 Finite difference time domain

In the finite difference time domain (FDTD) method, *time* is discretised as well as space, and at every time-step all the fields in the simulation are updated based on the previous value of the fields. However, the difficulty in adapting the time domain method to simulate *active* nanophotonic materials is that there is no pre-existing framework for modifying the permittivity tensor while the simulation is running. The effects of motion can be emulated by using a separate source to change the refractive index of the material, but this method introduces its own problems - the pump source can and in most cases will interfere with the original source. The most obvious way to bypass these problems is to directly update the permittivity of the simulation at each time-step. Although this requires having to re-calculate the update coefficients of the simulation every time-step, it is by far the easiest method to implement. Here, a vastly improved convergence time is proposed by moving the equations that are dependent on the permittivity to a single field update equation. In this case, only one update coefficient needs to be calculated per time-step (as opposed to 6) and as will be shown, this coefficient is a relatively inexpensive piecewise matrix division. The only downside of choosing such an update method is that the material permeability tensor becomes entwined in every other coefficient. However, since the permeability coefficients only need to be calculated once, the simulation is not adversely affected.

4.1.1 Formulation of the time-domain method

In the time-domain formulation, $\boldsymbol{H}$ fields are calculated at half time steps $(t + \frac{\Delta t}{2})$ and the electric fields at integer steps (t), in a central difference scheme, since taking a finite central difference over time would not ensure that the electric fields are located in the mid-point of the magnetic field steps and vice versa. In general, the electric field is much stronger than the magnetic field leading to floating point errors. To rectify this, the electric field is normalised against the impedance,

$$\tilde{\boldsymbol{E}} = \sqrt{\frac{\varepsilon}{\mu}} \boldsymbol{E}. \tag{4.10}$$

The partial derivatives are discretised in time as

$$C_x^E|_t^{i,j} = -\mu_{xx}|^{i,j}(c\Delta t)^{-1}\left[H_x|_{t+\frac{\Delta t}{2}}^{i,j} - H_x|_{t-\frac{\Delta t}{2}}^{i,j}\right], \tag{4.11}$$

$$C_y^E|_t^{i,j} = -\mu_{yy}|^{i,j}(c\Delta t)^{-1}\left[H_x|_{t+\frac{\Delta t}{2}}^{i,j} - H_x|_{t-\frac{\Delta t}{2}}^{i,j}\right], \tag{4.12}$$

$$C_z^H|_{t+\frac{\Delta t}{2}}^{i,j} = -\varepsilon_{zz}|^{i,j}(c\Delta t)^{-1}\left[E_z|_{t+\Delta t}^{i,j} - E_z|_{t-\Delta t}^{i,j}\right], \tag{4.13}$$

where C refers to the spatial curls of Equations 4.7, 4.8, and 4.9. The above equations can be rearranged to solve for the *future* fields in terms of the past fields,

$$H_x|_{t+\frac{\Delta t}{2}}^{i,j} = H_x|_{t-\frac{\Delta t}{2}}^{i,j} - c\Delta t(\mu_{xx}|^{i,j})^{-1}C_x^E|_t^{i,j}, \tag{4.14}$$

$$H_y|_{t+\frac{\Delta t}{2}}^{i,j} = H_y|_{t-\frac{\Delta t}{2}}^{i,j} - c\Delta t(\mu_{yy}|^{i,j})^{-1}C_y^E|_t^{i,j}, \tag{4.15}$$

$$\tilde{E}_z|_{t+\Delta t}^{i,j} = \tilde{E}_z|_{t-\Delta t}^{i,j} + c\Delta t(\varepsilon_{zz}|^{i,j})^{-1}C_z^H|_{t+\frac{\Delta t}{2}}^{i,j}. \tag{4.16}$$

yielding the update equations. Notably, by replacing $\boldsymbol{E}$ with $\boldsymbol{D}\varepsilon^{-1}$, the last field update equation instead becomes

$$\tilde{D}_z|_{t+\Delta t}^{i,j} = \tilde{D}_z|_{t-\Delta t}^{i,j} + c\Delta tC_z^H|_{t+\frac{\Delta t}{2}}^{i,j}, \tag{4.17}$$

where the E_z field can be obtained by,

$$\tilde{E}_z|_{t+\Delta t}^{i,j} = (\varepsilon_{zz}|^{i,j})^{-1}\tilde{D}_z|_{t+\Delta t}^{i,j}. \tag{4.18}$$

These equations are implemented using *MATLAB*, and form the basis of the time-domain simulations (Appendix B.1.1). However, there are several other components of the simulation that also require taking into account - namely the boundary conditions and source excitations.

4.1.2   Boundary conditions & the Perfectly Matched Layer

The Perfectly Matched Layer (PML) is an artificial medium that is developed to absorb EM waves incident from any direction with minimal reflection [102]. Since EM waves incident on PML do not reflect backwards, a simulation domain surrounded by PML effectively represents an open space, and is used commonly in finite difference methods to simulate spatially unbounded systems (such as waveguides with infinite length, or a point
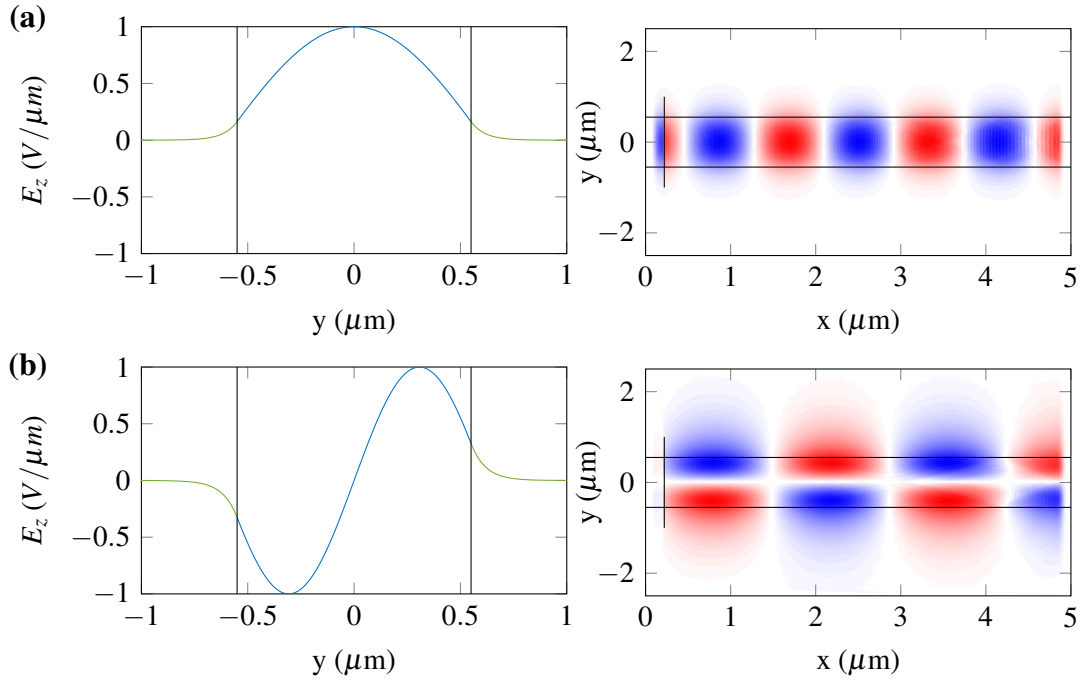
Figure 4.2: The first even and odd modes of a slab dielectric waveguide, **(a)** $|1\rangle$ (even) and **(b)** $|2\rangle$ (odd), normalised to unity as returned by the dispersion solver. Blue lines indicate regions inside the waveguide (guided modes), and green lines indicate regions outside the waveguide. On the right, the corresponding shape of the E_z field profile is shown. To excite a total line source, the returned field profile is paired with a sinusoidal oscillation that is written directly into the E_z field at every time-step.

source radiating). Strictly speaking, PML is not a boundary condition, but rather a special type of absorbing material placed adjacent to the boundaries of the simulation. In all simulations presented here, a PML layer of 20Δ is applied on the boundaries, where Δ is the chosen spatial discretisation ($\Delta x = \Delta y$). In the case where the discretisation is different along x and y, the PML layer extends inward depending on the given discretisation (i.e. the PML width on the left and right sides of the simulation would be $20\Delta x$, while the width along the top and bottom would be $20\Delta y$).

4.1.3   Modal source

Since all fields in the simulation are initialised to zero, an excitation of the fields is required. To excite a mode in a wave guide it is insufficient to merely place a point sinusoidal source at some arbitrary location near the guide. Even with a priori knowledge of the mode wavevector k and frequency ω, the source will excite several modes within a range of frequencies. To examine complete mode conversion, an exact known mode is required. If there are multiple modes passing through a modulated region, each will be transitioned up a band of the dispersion relation in turn. The typical method used to excite

guided modes in FDTD is to place a *gaussian* source of the form

$$g(t) = e^{-\left(\frac{t-t_0}{\tau}\right)^2}, \tag{4.19}$$

in some off-centre location, where t_0 is the pulse centre and τ is the 'spread'. Such a Gaussian source possesses an effectively infinite range of frequencies. After propagating through the waveguide, modes within range of the spread frequency are excited.

Instead of attempting to generate modes via Gaussian sources, a waveguide dispersion relation solver is implemented in *MATLAB* to both calculate dispersion relations, and return electric field amplitudes in the exact shape of the required mode (Appendix B.1), by numerically solving the transcendental equation [103]

$$\begin{bmatrix} \tan(k_x d) \\ -\cot(k_x d) \end{bmatrix} = \left[\frac{\omega^2 \mu_0 (\varepsilon_1 - \varepsilon_2)}{k_z^2} - 1 \right]^{\frac{1}{2}}, \tag{4.20}$$

where k_x and k_z are wavevector components in x and z respectively, ω is the given frequency, ε_1 is the waveguide permittivity, ε_2 is the surrounding permittivity, and d is the width of the waveguide.

To verify the implementation wherever dispersion relations are calculated, a comparison is also made to the open source *MPB* photonic bandstructure program [104], which instead makes use frequency iterative methods. Having a numerical solver for the bands means that a source can be excited directly by choosing an input region, passing the parameters of the wave guide to the dispersion solver, and obtaining a mode at a pre-defined frequency (or equivalently, wavevector). This mode shape is then paired with a sinusoidally oscillating source at the given frequency. This is demonstrated in Figure 4.2, where the output of the mode solver is shown for the first even $|1\rangle$ and odd $|2\rangle$ TE modes for a waveguide of width $1.1\mu m$ and relative permittivity 10.

4.1.4 Demonstration of direct photonic transitions

Here, a direct mode conversion is demonstrated through FDTD as a method of verifying the *MATLAB* implementation of the update equations (4.16). The waveguide is chosen to be of length $23\,\mu m$ and width $1.1\,\mu m$. From a dispersion relation calculation, such a waveguide supports the TE modes $|1\rangle$ at frequency $\omega_1 = 0.129\,(2\pi c/a)$, and $|2\rangle$ at $\omega_2 = 0.199\,(2\pi c/a)$, at the same wavevector k. A modulation of $\delta \cos(\Omega t + \phi)$ is initially applied from $2\,\mu m$ to $21\,\mu m$. This modulation here is a direct transition, as $\Delta k = 0$ [1]. A

---

[1] Such a choice of spatially independent modulation leads to a strictly *reciprocal* mode conversion. On the reverse path (RL), phase matching is still satisfied (no wavevector shift is applied) allowing the back-propagating mode to transition regardless.
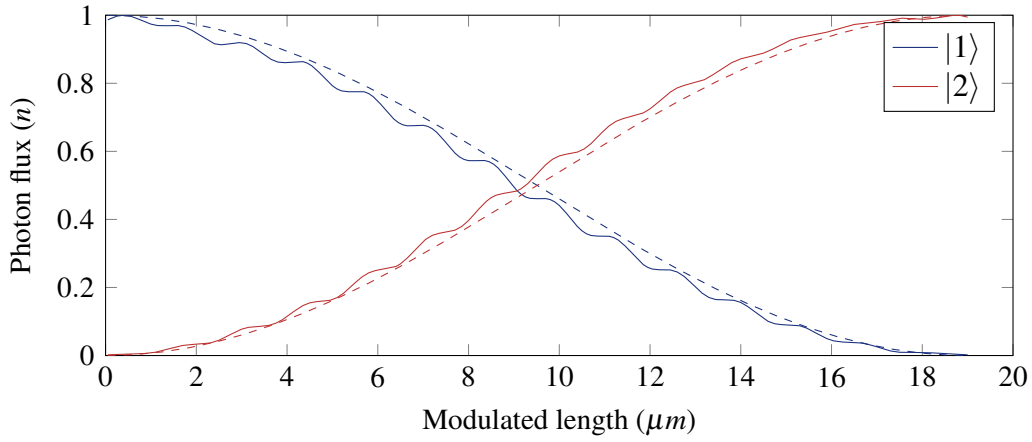
Figure 4.3: Normalised amplitude of the modes along the modulated region. Simulation results are in solid lines. Theoretical results from equation 3.38 are shown in dashed lines. Mode $|1\rangle$ vanishes at $19\,\mu m$, giving the value of the coherence length. As the amplitude of the first mode decreases, the second mode increases in turn. The discrepancy between theoretical and simulation is largely due to the generation of spurious side band frequency components, which theoretical treatments can not accurately predict.

modal line source is excited at $x = 1\,\mu m$ that extends from $y = 1$ to $y = 3\,\mu m$, with the spatial discretisation chosen as $\Delta x = \Delta y = 0.04\,\mu m$. To obtain the coherence length, the amplitudes of both modes are sampled throughout the modulated region continuously, by calculating a Fourier transform over the length simulation.

A detector (D_2) is placed at $22\,\mu m$ to collect the incident field after modulation, and another detector (D_1) placed in the region between the source and the beginning of modulation ($1.5\,\mu m$). To ensure the steady state solution is reached, the simulation is run for 10000 time steps (corresponding to a time of around $850\,fs$). To obtain the coherence length, the modulation region is first extended to $25\mu m$, and the amplitudes of modes $|1\rangle$ and $|2\rangle$ are sampled with a Fourier transform along the entire length of the waveguide, as shown in figure 4.3. The coherence length is then numerically determined to be $19\mu m$, based on how the first mode vanishes at that point. Note the discrepancy between theoretical and simulation, this is largely because the theoretical treatment of photonic transitions is restricted to only coupling between two adjacent modes. In reality, the modulation can generate backward propagating modes (such that $k \to -k$), as well as modes at higher sidebands, and thus power is lost to these spurious modes - which the semi-analytic coupled mode theory can not predict. With only a temporal modulation, scattering in the guide can transition backward reflected waves into higher order modes. This only occurs because reciprocity is not broken in the waveguide so that light is free to pass in both directions. Coupled mode theory does not predict such oscillations, as it is derived to assume the coupling is only between two exact modes.

Importantly, perfect mode conversion is observed in Figure 4.4 agreeing with the ex-
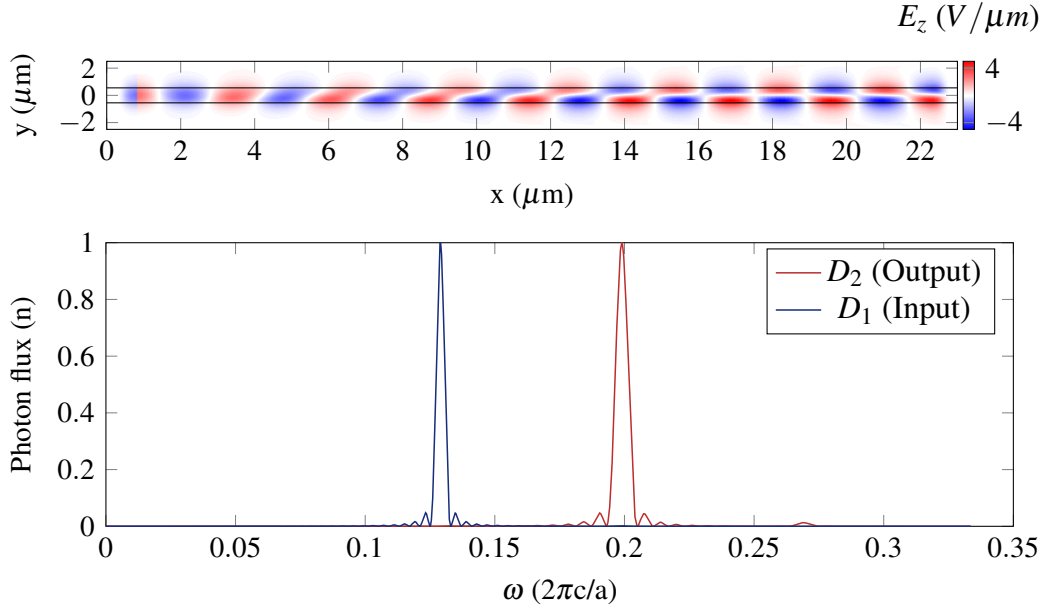
Figure 4.4: Complete mode conversion in a modulated waveguide between frequencies $0.129\,(2\pi c/a)$ and $0.199\,(2\pi c/a)$ in the left to right direction.

pected theory. The Fourier transform of the detector outputs illustrates the input $|1\rangle$ mode at $\omega_1 = 0.129\,(2\pi c/a)$ and output in mode $|2\rangle$ at $\omega_2 = 0.199\,(2\pi c/a)$. Additionally, a weak higher order mode $|3\rangle$ is observed at frequency $\omega_3 = 0.269\,(2\pi c/a)$ in the output. The existence of the higher order mode is attributed to a further direct transition of the 2nd mode.

4.2 Motivation for development of frequency domain solutions

Simulating effective modulations of wave-guide structures is evidently a computationally intensive process. Generally, devices that modulate permittivities operate in the gigahertz range, whilst the carrier waves are in the terahertz range. To observe a mode transition in a simulation would then require an average of 10^2 optical cycles of the carrier wave. This huge discrepancy in frequencies is not amenable to time-domain simulations since the discrete time-step must be chosen based on the highest frequency present. Such a massive gap between the optical source frequency and the modulation frequency lead to slow convergence times, since the input wave must pass through at minimum one cycle of the modulation. There are however several benefits granted by the harmonic nature of the modulation. The first is that the modulation generates sidebands at *known* frequencies, $\omega_n = \omega_0 \pm n\Omega$, where Ω is the modulation frequency and n is the set of integers. This is

incredibly advantageous: every possible frequency that can exist in the simulation space is known before the simulation begins. The second benefit granted is that the modulation is harmonic in nature, and it is this harmonicity that allows for a method of expressing the time dependent modulations in frequency space. Thus, a method is sought in the frequency domain, where *frequency* is discretised instead of *time*.

4.3 Finite difference frequency domain

The finite difference frequency domain represents an alternative method to obtaining full-wave solutions to Maxwell's equations, complementary to the time domain. By a suitable transformation of Maxwell's equations into the frequency domain, the problem of time-step based simulations instead becomes one of solving a large system of linear equations of the form $Ax = b$, where A is the *wave matrix*, x is a vector that contains the entire electromagnetic field, and b is a current source. Fortuitously, in two dimensions the most efficient method of solving for the field distributions is through the standard matrix inversion, $x = A^{-1}b$, which has the trivial solution of $x = 0$ for a zero source simulation ($b = 0$). In solving for x, one obtains the steady-state solution directly embedded in the matrix, that is the point at which there is no transient response in the fields - the only variation is in the phase.

4.3.1 Formulation of FDFD

In the frequency domain, Maxwell's equations take the form [105]

$$\nabla \times \boldsymbol{E}(\boldsymbol{r}, \omega) = -i\omega\mu(\boldsymbol{r}, \omega)\boldsymbol{H}(\boldsymbol{r}, \omega) - \boldsymbol{M}(\boldsymbol{r}, \omega), \tag{4.21}$$

$$\nabla \times \boldsymbol{H}(\boldsymbol{r}, \omega) = i\omega\varepsilon(\boldsymbol{r}, \omega)\boldsymbol{E}(\boldsymbol{r}, \omega) + \boldsymbol{J}(\boldsymbol{r}, \omega), \tag{4.22}$$

where $\boldsymbol{E}$ and $\boldsymbol{H}$ are as usual the electric and magnetic fields respectively, and $\boldsymbol{J}$ and $\boldsymbol{M}$ are the electric and magnetic current source densities. The field solutions can then be obtained by solving the general matrix equation

$$\begin{bmatrix} -i\omega\varepsilon & \nabla\times \\ \nabla\times & i\omega\mu \end{bmatrix} \begin{bmatrix} \boldsymbol{E} \\ \boldsymbol{H} \end{bmatrix} = \begin{bmatrix} \boldsymbol{J} \\ -\boldsymbol{M} \end{bmatrix}. \tag{4.23}$$

Equation 4.23 is evidently of the form $Ax = b$. However in attempting to solve for the fields x, the wave matrix A will become ill-conditioned - a characteristic of matrices which is unfavourable to numeric solvers. Such ill-conditioning arises because the $\boldsymbol{E}$ field is usually several orders of magnitude stronger than the $\boldsymbol{H}$ field. In the time-domain, this

discrepancy in field magnitude was corrected by normalising the field variables. On the other hand, in the frequency domain a more precise solution can be obtained by eliminating the $\boldsymbol{H}$ field completely from equation 4.21 to obtain

$$\nabla \times \mu^{-1} \nabla \times \boldsymbol{E} - \omega^2 \varepsilon_s \boldsymbol{E} = -i\omega \boldsymbol{J} - \nabla \times \mu^{-1} \boldsymbol{M}. \tag{4.24}$$

$\boldsymbol{H}$ is chosen to be eliminated because nanophotonic objects, which are the focus of these simulations, are in most cases smaller than the source wavelength (that is, $|\omega^2 \varepsilon \boldsymbol{E}| \ll |\nabla \times \mu^{-1} \nabla \times \boldsymbol{E}|$). This allows for the approximation of the operator on the left hand side in Equation 4.24 by $\nabla \times \mu^{-1} \nabla \times$, especially in the case where μ is unity - the operator becomes much more favourable to numeric solvers.

In solving 4.24,the magnetic current source $\boldsymbol{M}$ can be safely ignored without loss of generality [2]. The equation to solve using finite difference methods then takes the form

$$\nabla \times \mu^{-1} \nabla \times \boldsymbol{E} - \omega^2 \varepsilon \boldsymbol{E} = -i\omega \boldsymbol{J}. \tag{4.25}$$

As an additional benefit to eliminating $\boldsymbol{H}$, the size of the simulation is effectively halved, since only one field is calculated. Once 4.25 is solved for $\boldsymbol{E}$, $\boldsymbol{H}$ can be obtained by back-substitution into the frequency domain equations 4.24.

4.3.2   The multi-frequency method (MF-FDFD)

The difficulty in using the frequency domain formulation to simulate modulated waveguides is that it is only capable of handling one frequency per simulation. Likewise, the necessary modulation can not be accounted for with any single type of time-independent permittivity tensor, since it can not be altered once the wave matrix has been built. Based on the work of Shi et al., the FDFD method is here extended to accommodate an effectively infinite number of frequencies [106], in what is known as the multi-frequency finite difference frequency domain (MF-FDFD) method.

The essence of MF-FDFD is that a permittivity modulation imparts an additional polarisation density at a frequency ω, causing Equation 4.25 to take the modified form,

$$\nabla \times \mu^{-1} \nabla \times \boldsymbol{E} - \omega^2 \varepsilon \boldsymbol{E} = -i\omega \boldsymbol{J} + \omega^2 \boldsymbol{P}. \tag{4.26}$$

To account for such a polarisation density in the simulation, consider first the nature of the modulation itself;

---

[2]This is because for any given $\boldsymbol{J}$ and $\boldsymbol{M}$, a new current source density $\boldsymbol{J}' = \boldsymbol{J} + \frac{1}{i\omega}\nabla \times \mu^{-1}\boldsymbol{M}$ and $\boldsymbol{M}' = 0$ will always result in the same right hand side of 4.24

$$\varepsilon(t)' = \delta\cos(\omega t + \phi) = \frac{\delta}{2}\left[e^{i(\Omega t + \phi)} + e^{-i(\Omega t + \phi)}\right]. \tag{4.27}$$

In this case, the modulation gives rises to a time-dependent polarisation $P(t)$ of the form

$$P(t) = \frac{\delta}{2}\left[e^{i(\Omega t + \phi)} + e^{-i(\Omega t + \phi)}\right]E(t). \tag{4.28}$$

Whereby using the standard Fourier transform,

$$f(t) = \int_{-\infty}^{\infty} \hat{f}(\omega)e^{2\pi i \omega t}\,d\omega, \tag{4.29}$$

gives the polarisation in frequency space,

$$\tilde{P}(\omega) = \frac{\delta}{2}e^{i\phi}E(\omega - \Omega) + \frac{\delta}{2}e^{i\phi}E(\omega + \Omega). \tag{4.30}$$

In the case where a photonic device is excited with a current density source J at frequency ω_1, dynamic generate n sidebands at frequency components $\omega_n = \omega_1 + n\Omega$. Then, under modulation the total electric field in the time domain $E(t)$ is the superposition of electric field components at each sideband $E_z(\omega_n)$ through the linearity of Maxwell's equations,

$$E(t) = \Re\{\sum_n E(\omega_n)e^{i\omega_n t}\}. \tag{4.31}$$

Although there are effectively an infinite number of such sidebands $n \in Z$, the simulation is chosen to be truncated between $-N$ to N sidebands. Substituting equations 4.30 through 4.31 into 4.24 yields the set of n equations,

$$\nabla \times \mu(\omega_n)^{-1}\nabla \times E(\omega_n) - \omega_n^2\varepsilon_{wg}(\omega_n)E(\omega_n) - \frac{1}{2}\omega_n^2\delta e^{i\phi}E(\omega_{n+1}) = -i\omega J(\omega_0)\delta_{n0}$$
$$\tag{4.32}$$

where δ_{n0} is the Kronecker delta function. The finite difference method is implemented to solve the above equation in two dimensions (Appendix B.1.2), by discretising the frequencies of Equation 4.32. Such discretisation results in the matrix equation $Ax = b$, which is solved through *MATLAB's* UMFPACK iterative matrix solver. Since the fields are still located on the Yee grid, the formulation of the spatial derivatives is identical to that of the time-domain. Similarly, the PML construction and modal source input do not differ.

Chapter 5

Simulation results and discussion

In this chapter, the results of applying the MF-FDFD method are presented to demonstrate non-reciprocity in modulated waveguides. 'a' is used regularly in the units of frequency, and is a normalisation constant which allows the simulation to be scaled to any size, a common procedure in electromagnetic simulations. For all results presented here, $a = 1\,\mu m$.

5.1   Numerical validation of FDFD

As a preliminary verification of the MF-FDFD implementation, an identical simulation to the time-domain one of Section 4.1.4 is calculated over one sideband. The waveguide is again of width $1.1\,\mu m$ and length $23\,\mu m$, with a modulation of $\varepsilon'(t) = 0.1\cos(\omega t)$ applied between 2 to $21\,\mu m$. The upper and lower halves of the waveguide are modulated with a π phase difference, and the waveguide is injected with a modal source at $1\,\mu m$ of frequency $0.129\,(2\pi c/a)$. The amplitude of the modes are extracted along the length of the modulation region, and compared to the results of FDTD. As an additional benefit to the FDFD method, the field evolution of the mode can be visualised completely, as in Figures 5.1b and 5.1c.

There is excellent agreement between FDFD and FDTD as seen in Figure 5.1a. Both simulations predict the characteristic minor oscillations during modulations, however FDTD predicts that power is lost at a faster rate. This is likely because the FDFD simulation will only operate over the number of sidebands specified. Since small amounts of power are naturally lost to higher order sidebands, the frequency domain simulation can not completely predict the modal variation. However, it is worth pointing out that both simulations perfectly agree on the convergence of the coherence length at $19\,\mu m$.
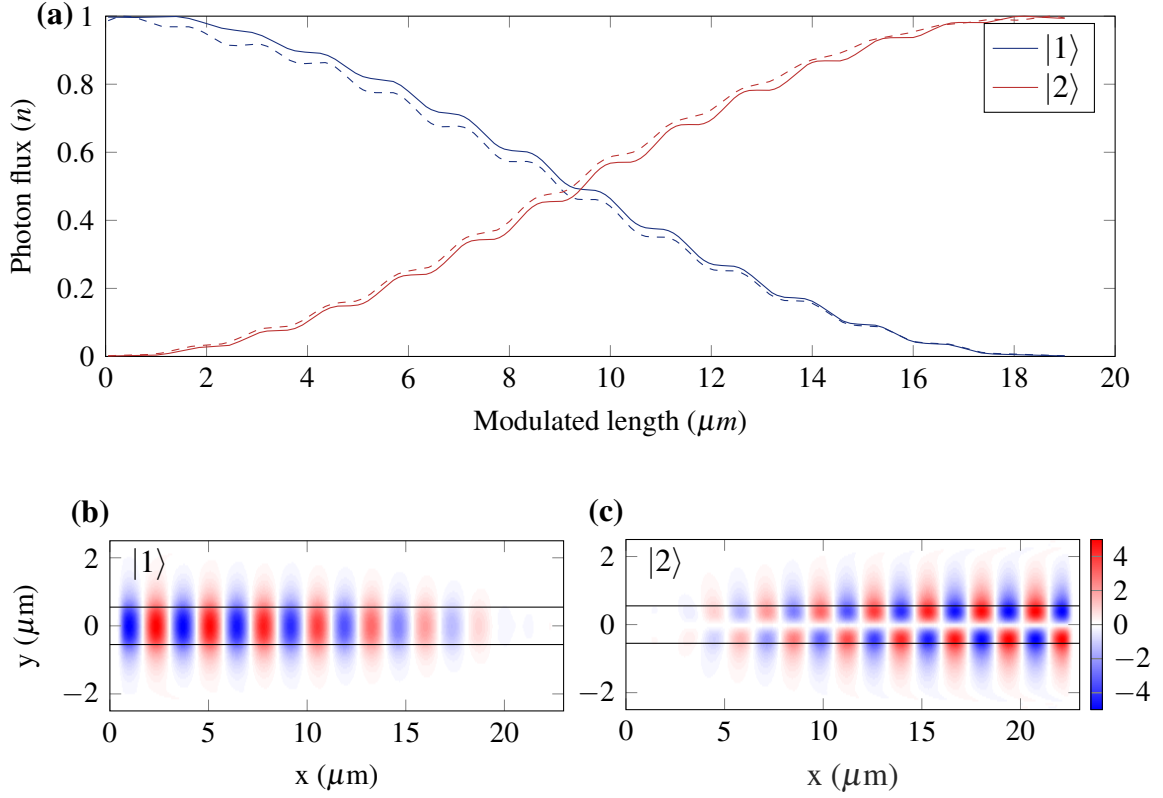
Figure 5.1: **(a)** Amplitude of both modes $|1\rangle$ and $|2\rangle$ for the time and frequency domain simulations, with the time domain in dashed lines. **(b)**Mode evolution of $|1\rangle$ as it propagates through the waveguide, and likewise for **(c)** $|2\rangle$. Note how $|1\rangle$ completely vanishes after reaching the coherence length.

5.1.1 Direct validation through coupled-mode theory

The finite difference method simulates modes over any number of given sidebands. However, the implementation of the time domain method provided here is incapable of extracting these sidebands. Thus, to independently verify the frequency domain implementation, a simulation of a dynamically modulated waveguide over several sidebands is performed and compared to coupled-mode theory. Since the previously shown coupled mode-theory assumes only transitions between two modes (Equation 3.38), a differential equation that describes transitions between n modes is derived in Appendix A.2. This allows for the comparison of the MF-FDFD implementation against a semi-analytic result.

The simulation considers a slab waveguide of relative permittivity $\varepsilon = 4$ surrounded by vacuum in a region $10 \times 4 \, \mu m$ discretised to $\Delta = 0.04 \, \mu m$. The waveguide is $10 \, \mu m$ long and $0.75 \, \mu m$ wide, which leads to a choice of an even mode of $\omega_1 = 0.667 \, (2\pi c/a)$ at $k_1 = 0.841 \, (2\pi/a)$ and an odd mode at $\omega_2 = 0.645 \, (2\pi c/a)$ and $k_2 = 1.097 \, (2\pi/a)$. A permittivity modulation of $0.1\varepsilon_0 \cos(\Omega t)$ is applied between 1.5 and $9 \, \mu m$, where the
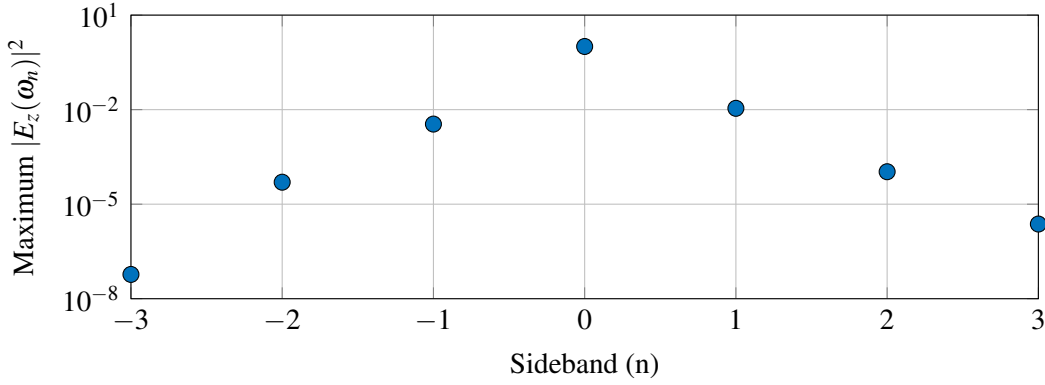
**Figure 5.2:** The maximum field amplitude calculated for each sideband n on a log scale. The field intensity decreases exponentially with n. Note that the amplitude of the sidebands is not symmetric about $n = 0$.

top and bottom halves of the waveguide are modulated with a π phase difference to maximise coupling. This weak choice of modulation is insufficient to transition a mode, however coupled mode theory becomes exact in the limit of small modulations. Thus, it is perfectly suited to analysing the response of FDFD. The simulation is truncated to 5 frequency sidebands for $\omega_n = \omega_1 + n\Omega$ where $n \in [-4, 4]$, and a continuous wave input of the first mode is excited at location $1\,\mu m$ using the standard solver, whose power is normalised to $1\,W\mu m^{-1}$. For each frequency sideband the amplitude of the mode is extracted and compared to the semi-analytic results provided by the coupled-mode theory equation A.28.

The maximum $|E_z|^2$ field at each sideband ω_n is first extracted and shown in figure 5.2. At the initial band ω_1, the field amplitude is normalised to unity. The fields exponentially decrease with $|n|$. However, the higher sidebands decrease at a slower rate than that of the negative sidebands. Importantly, this means that the impact of reducing the sideband count in the simulation is minimal for a weak modulation. Since the final fields are the sum of each field component at all the sidebands calculated, any missing sidebands will lead to a slight inaccuracy in the final result. Here, the combined second sideband frequencies have a maximum amplitude of less than 0.0001% of the initial mode.

The results of the simulation for the modal profile and corresponding amplitudes in each mode are shown in Figure 5.3. There is an excellent agreement between CMT and FDFD in Figure 5.3b. However, FDFD shows minor oscillations along the length of the waveguide that CMT can not predict, identical to the oscillations in previous simulations with only temporal modulations. By performing a standard Fourier transform on the modal amplitude at frequency sideband $\omega_1 + \Omega$, the minor oscillation is found to be at a period of $T = 0.075\,\mu m$. This period corresponds exactly to the generation of backward propagating modes, $0.075\,\mu m = 1/(k_1 + k_2)$.
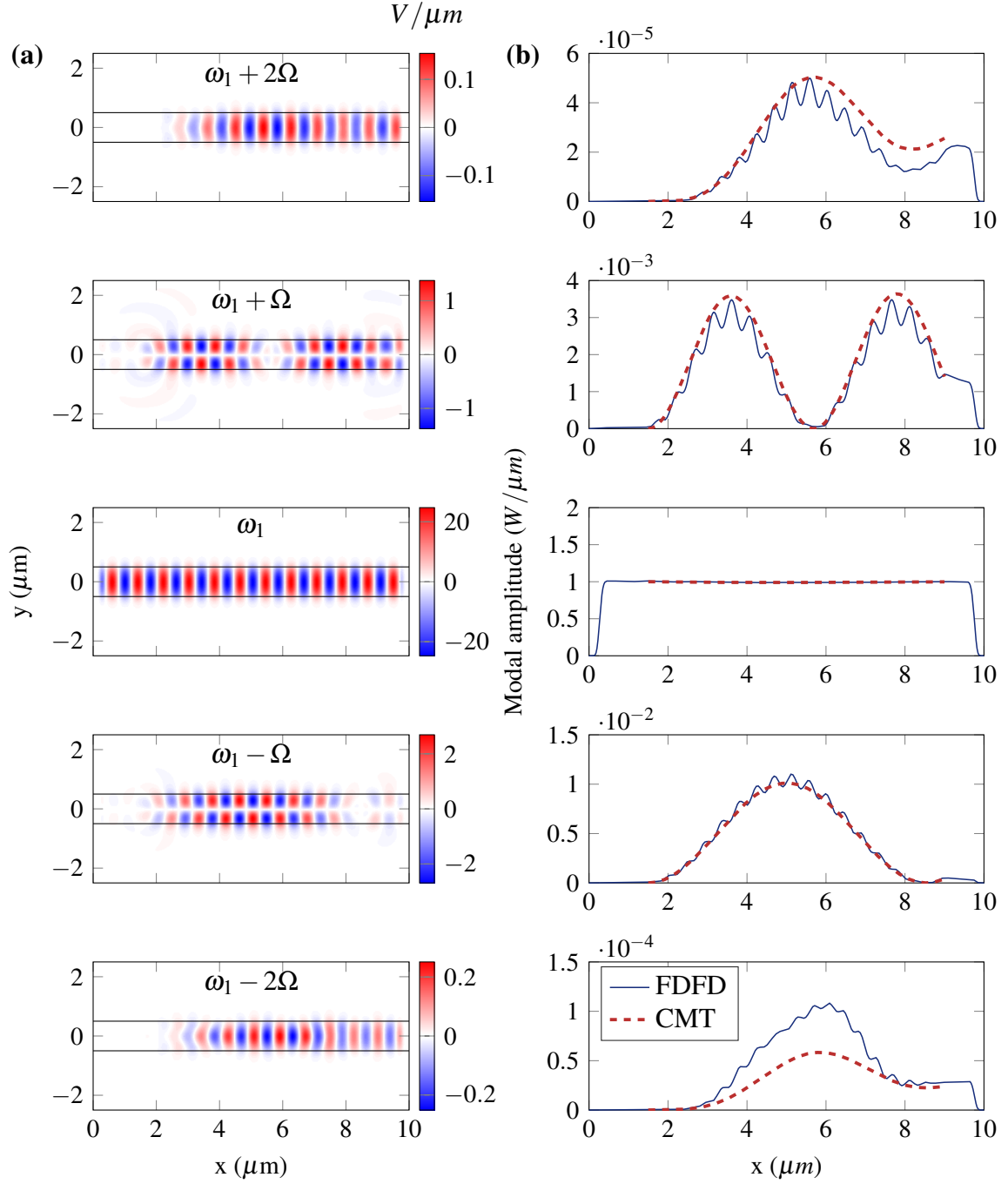
Figure 5.3: (a) The modal field profiles of the transverse electric field E_z propagating along the length of the waveguide structure. Each graph represents a sideband of the original frequency ω_1 separated by integer multiples of the modulation frequency $n\Omega$. **(b)** The corresponding modal amplitudes of each sideband along the structure as calculated theoretically via CMT (dashed) and through the FDFD simulation (solid).

5.2 Non-reciprocal mode conversion through indirect transitions

Having extensively validated the implementation of the frequency domain method, non-reciprocal mode transition is now demonstrated for a spatio-temporal direct permittivity modulation. The simulation is chosen to be a thin slab dielectric waveguide of width $0.22\,\mu m$ and permittivity $\varepsilon = 12.25$, corresponding to that of silicon. This particular waveguide is chosen as it possesses highly parallel bands in the dispersion relation (Fig 5.4). Being parallel, there will almost always be a phase-matched pair of modes in the forward $(+k)$ direction. So that for any even mode $|1\rangle$, a single modulation profile will ensure a transition to a corresponding odd mode $|2\rangle$ over a wide range of frequencies. This is ideal from an optical isolation point of view, which requires an ideally infinite frequency operation range. Likewise, in the backward propagating direction $(-k)$, there is no single phase-matched pair of modes for a transition. Thus, a single modulation between the even and odd modes on this choice of waveguide provides highly *broadband* optical isolation.

The simulation is run for an even and odd mode pair at frequencies $\omega_1 = 0.647\,(2\pi c/a)$ and $\omega_2 = 0.8879\,(2\pi c/a)$ respectively, chosen from the calculated dispersion relation of Figure 5.4. These modes have corresponding wavevectors $k_1 = 1.189\,(2\pi/a)$ and $k_2 = 0.912\,(2\pi/a)$. A permittivity modulation of the form $\varepsilon(x,t)' = \delta\cos(\Omega t + \Lambda x)$ is applied between $2.5\,\mu m$ and $7.5\,\mu m$ $(L_c = 5\,\mu m)$ where $\Omega = \omega_2 - \omega_1$ is the modulation frequency and $\Lambda = k_2 - k_1$. The upper and lower halves of the waveguide have a π phase difference.
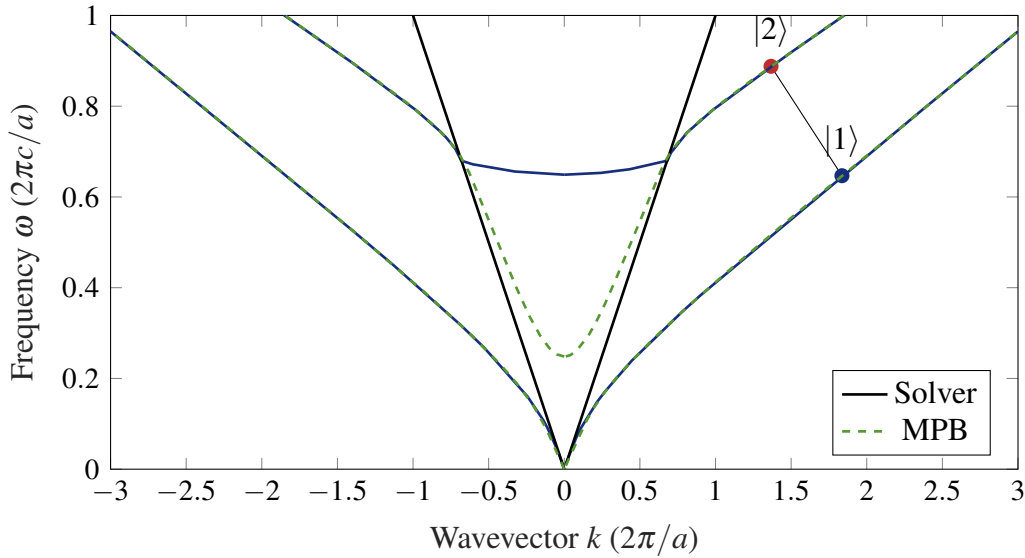
Figure 5.4: Dispersion relation for the waveguide of width $0.22\,\mu m$ and relative permittivity $\varepsilon = 12.25$, compared between the analytic solver and the open-source *MPB*.
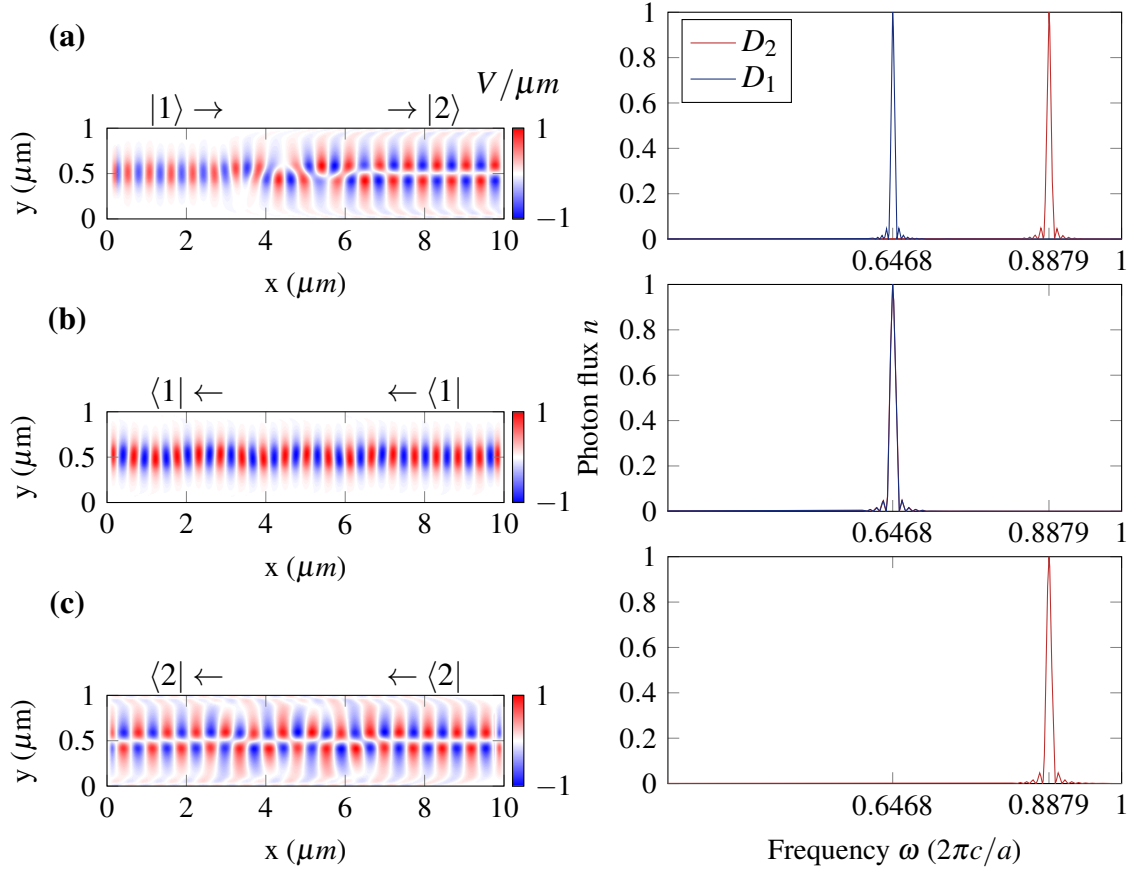
Figure 5.5: Phase matched non-reciprocal mode conversion in a modulated structure for **a)** LR, **b)** LR, and **c)** TR directions. On the left are the E_z fields, and on the right are the corresponding frequencies for detectors D_1 and D_2. Note that in all the Fourier graphs, results are shown for both detectors. However, in the case of the *RL* and *TR* directions, the input and output are identical.

The coherence length was determined by extending the modulation over a wider range and sampling the mode amplitudes as usual, with a strong modulation of $\delta = 1$. A modal source is excited at $1\,\mu m$, and frequencies are extracted at positions $D_1 = 1.5\,\mu m$ and $D_2 = 9\,\mu m$ over 5 sidebands at a spatial discretisation of $\Delta = 0.04\,\mu m$.

Figure 5.5 shows the results of the simulation for the forward, backward, and time-reversed simulations. Only the total combined field of all sidebands is shown ($\sum E_z(\omega_n)$), as opposed to each individual sideband. The system exhibits a strongly non-reciprocal response - on the left to right path, the mode completely converts from $|1\rangle$ to $|2\rangle$. However, on the right to left direction the modulation does not cause a transition since there is no corresponding point on the dispersion relation for the mode to 'jump'. Similarly, on the time-reversed path the modulation does not transition the odd mode to the second even mode (the third band on the dispersion relation). These non-reciprocal mode conversions can be removed using standard modal filters, allowing for complete isolation [107], [108].
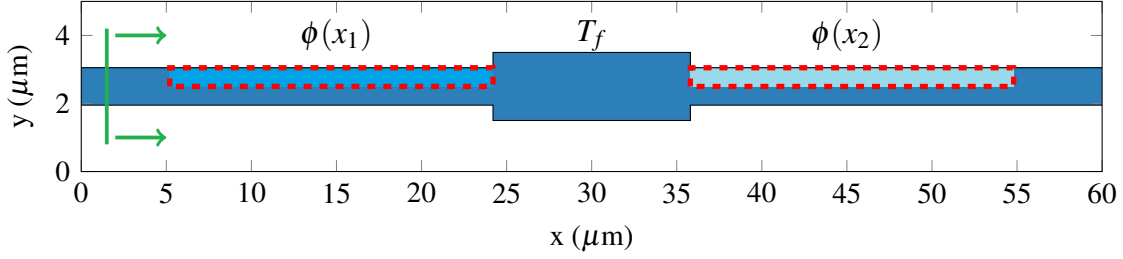
Figure 5.6: The modulated waveguide structure for demonstrating a photonic Aharonov-Bohm effect. The dark blue region is a material of unity permeability and relative permittivity $\varepsilon = 12.25$. The light blue sections enclosed in dashed red lines are regions where the permittivity is modulated by an amount $0.1\varepsilon\cos(\omega t + \phi)$, with $\phi(x_1)$ on the left and $\phi(x_2)$ on the right. The green line indicates the region over which the modal source is injected, in this case, from left to right (LR). The central waveguide imparts a mode-dependent phase on light passing through it, described by the transfer matrix T_f.

5.3   Optical isolation through a photonic AB effect

The difficulty in applying spatio-temporal modulations for the purpose of optical isolation is that the spatial dependence of the modulation is highly difficult to engineer. Currently, such modulations are created by simultaneously controlling the permittivity of hundreds of discrete points in a waveguide at different phases. However, without the wavevector shift the mode transition is purely reciprocal, as modes propagating in the reverse direction are still phase-matched (the transition on the dispersion relation is completely vertical, and so the modulation does not discriminate between left and right propagating modes). Here, based on the work of Fang et al. [51], a broadband tunable optical isolator is constructed and simulated in the frequency domain using only the gauge potential that emerges from the phase of *temporal* dynamic modulations, as discussed in Section 3.2.2. The choice of a direct transition marks the ideal configuration for a modulation, as only two separate regions need to be modulated with no spatial dependence.

Consider first the structure of Figure 5.6, which consists of a single narrow waveguide connected to a central waveguide region. The narrow waveguide supports an even and odd mode $|1\rangle$ and $|2\rangle$ respectively. A modulation of the form

$$\varepsilon(t)' = \delta\cos(\Omega t + \phi(x_1)) \tag{5.1}$$

is applied on the left side of the waveguide, and another modulation

$$\varepsilon(t)' = \delta\cos(\Omega t + \phi(x_2)) \tag{5.2}$$

on the right side to induce reciprocal transitions between the modes. The central waveguide region can be chosen to impart a mode-dependent phase on light passing through

it, so there are effectively two pathways through which light can propagate. The transfer matrix for modes passing through the central waveguide is then

$$T_f = \begin{bmatrix} e^{i\phi(P_1)} & 0 \\ 0 & e^{i\phi(P_2)} \end{bmatrix}. \tag{5.3}$$

In the second path (P_2), a photon of mode $|1\rangle$ is injected from the left and undergoes a transition to state $|2\rangle$, gaining an additional $\phi(x_1)$ phase. Upon passing through the central region, the photon acquires an additional phase $\phi(P_2)$, and undergoes a transition back to $|1\rangle$ in the second modulated region, gaining a final $-\phi(x_2)$ phase. In the first path (P_1), the initial mode is no longer converted and only acquires a $\phi(P_1)$ phase from the central waveguide region.

Thus, the total phase difference between the two pathways is then

$$\Delta\phi_{LR} = \phi(P_2) - \phi(P_1) + \phi(x_1) - \phi(x_2). \tag{5.4}$$

Likewise, in the right to left direction the total phase difference is instead

$$\Delta\phi_{RL} = \phi(P_2) - \phi(P_1) + \phi(x_2) - \phi(x_1), \tag{5.5}$$

which is identical to the discussion of the photonic Aharonov-Bohm effect of Section 5.3. In this case, the two modulated regions play the role of the separate interferometer arms, with the path-dependent phase of the central waveguide being equivalent to the phase acquired by an electron passing through a magnetic vector potential $\mathbf{A}$.

Because of this, despite the nature of the direct modulation itself being reciprocal, the gauge potential can be designed to generate non-reciprocal phases. In particular, non-reciprocal frequency conversion can be demonstrated without requiring a spatial modulation profile by choosing the phases so that $\phi(x_2) - \phi(x_1) = \pi/2$, and $\phi(P_2) - \phi(P_1) = \pi/2$. To allow for interference between modes, the modulated length is chosen as $L = 0.5L_c$, so that only half of the mode will transition (50% of the modal power will transition to the other mode). From these choices, the transfer matrix for modes propagating right to left is then

$$T_{LR} = T(\phi_2)T_f T(\phi_1) = e^{-i(2kL-\phi(P_1))} \begin{bmatrix} 0 & i \\ -1 & 0 \end{bmatrix}, \tag{5.6}$$

On the other hand, in the right to left direction the transfer matrix is instead given by

$$T_{RL} = T(\phi_1)T_f T(\phi_2) = e^{-i(2kL-\phi(P_1))} \begin{bmatrix} 1 & 0 \\ 0 & i \end{bmatrix}. \tag{5.7}$$
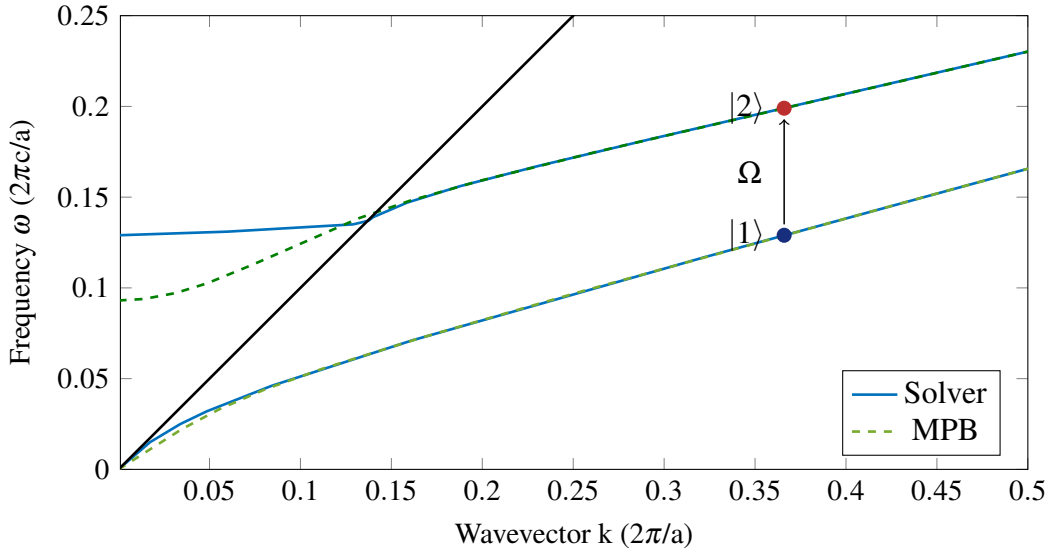
Figure 5.7: Dispersion relation of a waveguide with width $1.1\,\mu m$ and relative permittivity 12.25. Green dashes indicate dispersions obtained through *MPB*, whereas blue lines indicate those calculated analytically using the purpose-written solver. The red line is the direct transition between modes $|1\rangle$ and $|2\rangle$. Since the modulation has no spatial dependence, the modulation does not discriminate between forward and backward propagating modes.

From this, an even mode of state $|1\rangle$ injected from the left of the waveguide will completely convert to an odd mode $|2\rangle$, whereas the same even mode injected from the right will remain an even mode.

This is implemented in the frequency domain simulation by choosing the narrow waveguide to be of width $1.1\,\mu m$ extending from 0 to $60\,\mu m$, and the central waveguide region to be $2.2\,\mu m$ wide and $11.6\,\mu m$ long, with relative permittivity $\varepsilon = 12.25$. For the narrow waveguide, this choice corresponds to the dispersion relation of Figure 5.7. The direct transition is induced between an even mode $|1\rangle$ chosen at $\omega_1 = 0.129\,(2\pi c/a)$ and odd mode $|2\rangle$ at $\omega_2 = 0.199\,(2\pi c/a)$, which share the same wavevector $k_{1,2} = 0.380\,(2\pi/a)$. To satisfy the modulation condition for the above transfer matrix, the waveguide is modulated on the left and right by $0.1\varepsilon\cos(\Omega t + \phi)$, with the phase of modulation set at 0 and $\pi/2$ respectively $(\phi(x_2) - \phi(x_1) = \pi/2)$. The choice of width for the central waveguide $(2\,\mu m)$ ensures that even and odd modes acquire a $\pi/2$ phase difference upon passing through $(\phi(P_2) - \phi(P_1) = \pi/2)$. The length of the modulated regions is half the coherence length $(19\,\mu m)$, so that a mode injected from the left will undergo a 50% transition to the second mode, and vice versa. To test the non-reciprocal conversion, a modal source is excited at $1\,\mu m$ for the left to right direction, and $59\,\mu m$ for the right to left and time-reversed directions. The simulation is performed over 3 sidebands at a spatial discretisation of $\Delta = 0.04\,\mu m$, however only the first set of sidebands are shown.
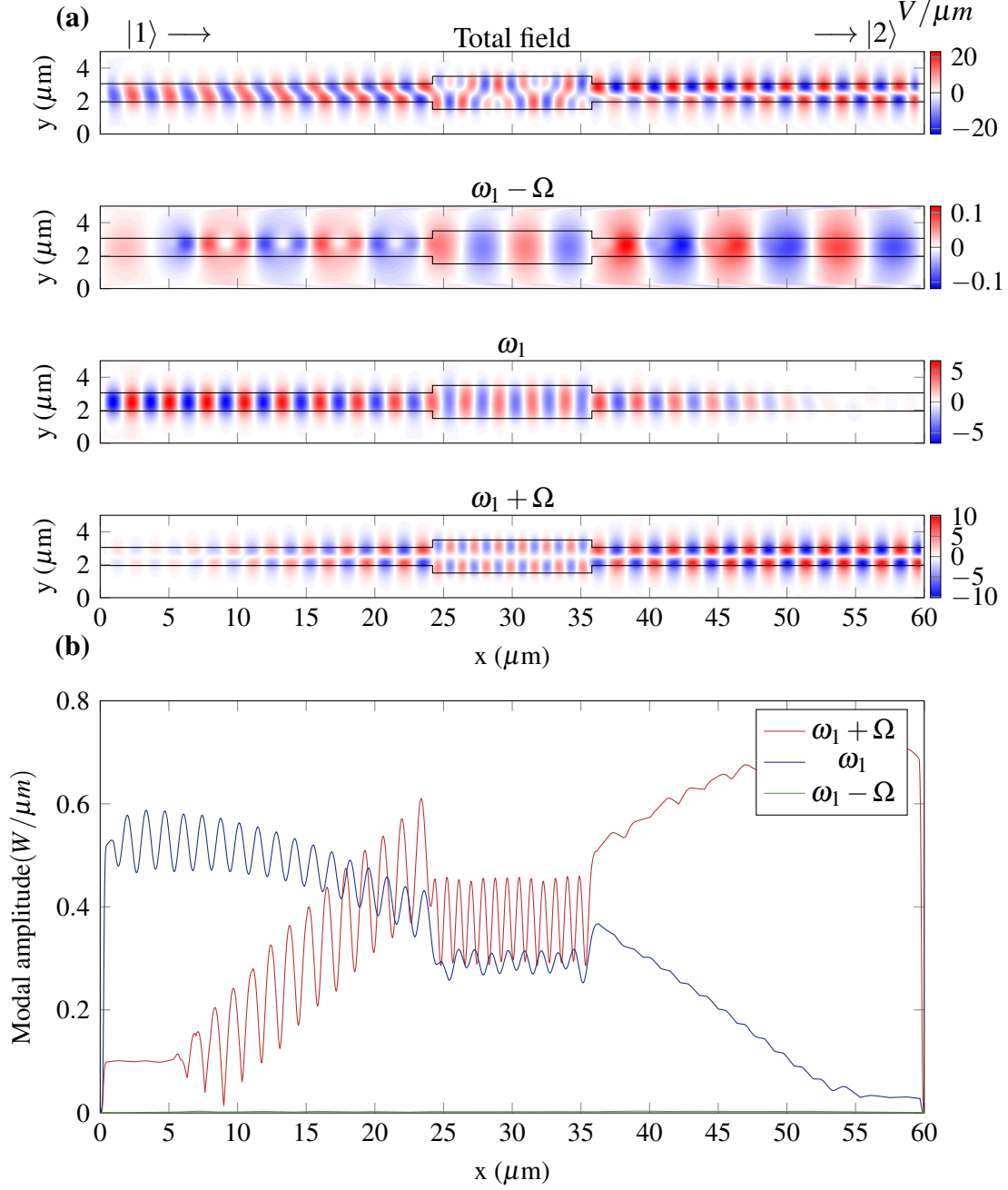
Figure 5.8: Propagation in the forward (RL) direction for the photonic AB effect. **(a)** E_z field profiles of the total field, and its separate components in the first sidebands. **(b)** Corresponding modal amplitudes of each sideband propagating through the modulated region. Mode $|1\rangle$ is completely converted to $|2\rangle$.
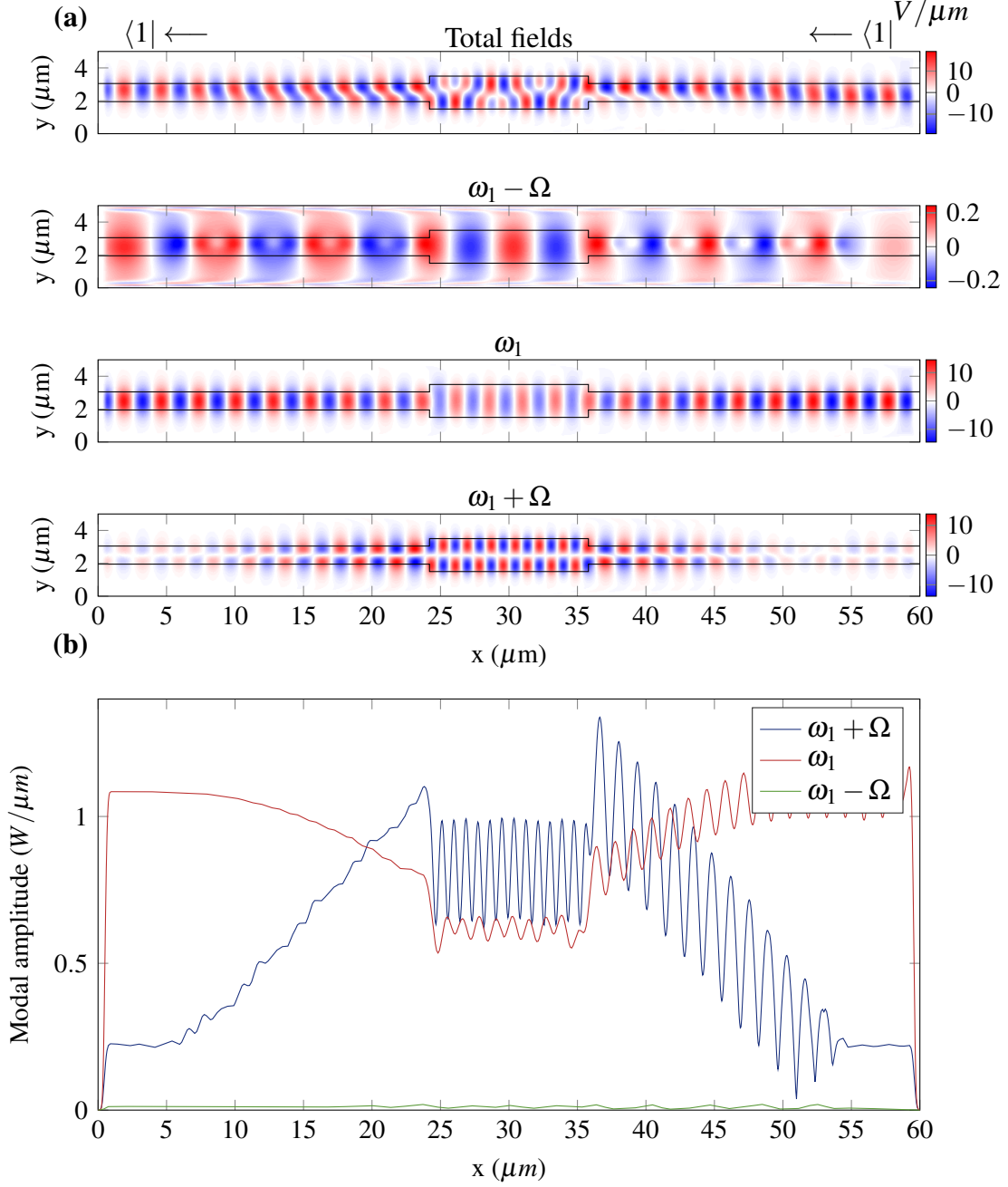
Figure 5.9: Non-reciprocal propagation in the RL direction. **(a)** E_z field profiles of the total field, and its separate components in the first sidebands. **(b)** Corresponding modal amplitudes of each sideband propagating through the modulated region. Mode $\langle 1|$ remains in state $\langle 1|$, implying a broken PT-symmetry.
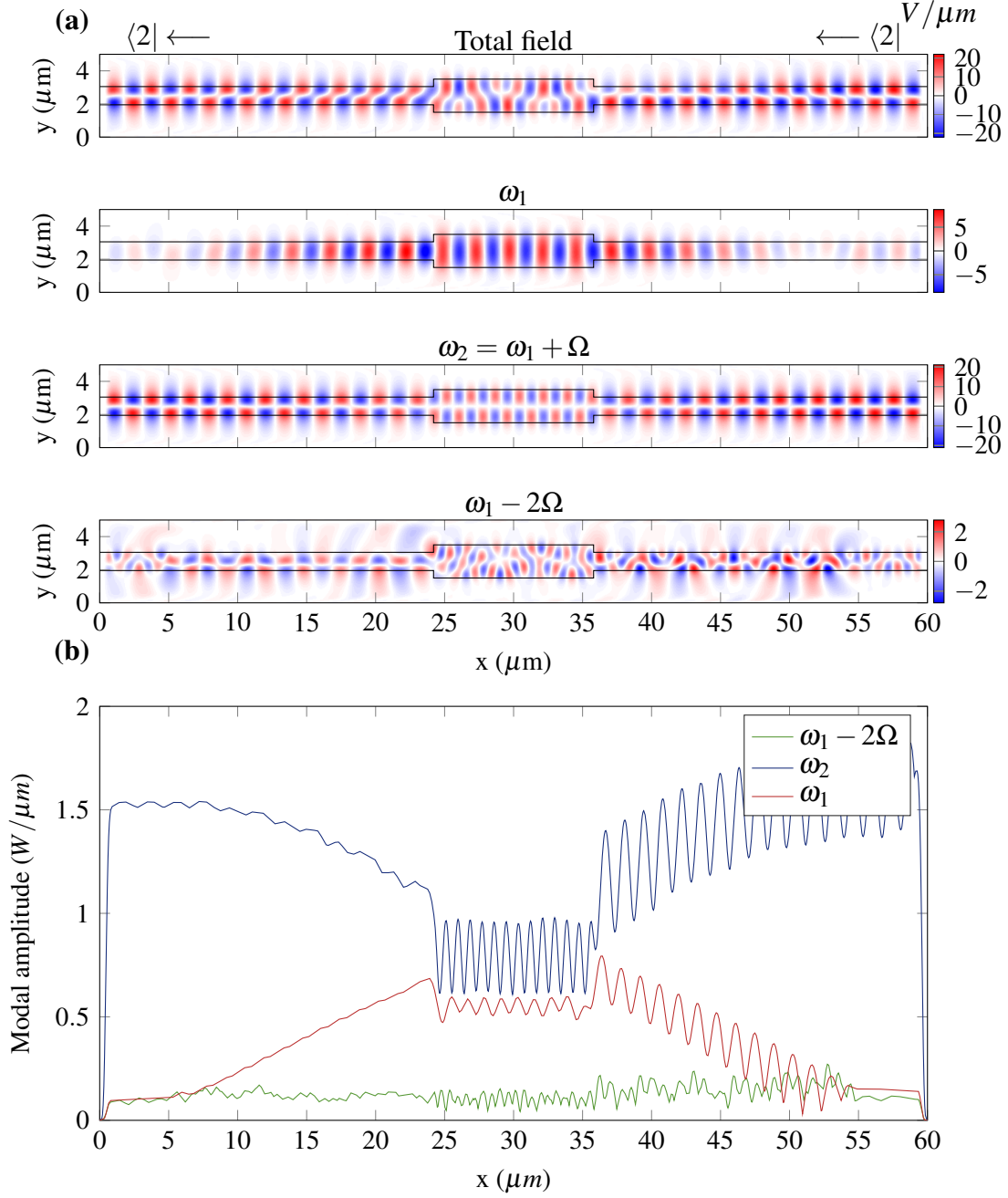
Figure 5.10: Non-reciprocal propagation under a time-reversed operation. Light of mode $\langle 2|$ is injected from the RL direction, mimicking a time-reversal operation.**(a)** E_z field profiles of the total field, and its separate components in the first sidebands. **(b)** Corresponding modal amplitudes of each sideband propagating through the modulated region. Since TR-symmetry is broken, even after propagating through the modulated structure the mode does not transition back to $|1\rangle$, and instead remains in state $\langle 2|$. Note how the field profile at $\omega_1 - 2\Omega$ exists as a superposition of several modes, since it does not have an allowed solution on the band-structure.
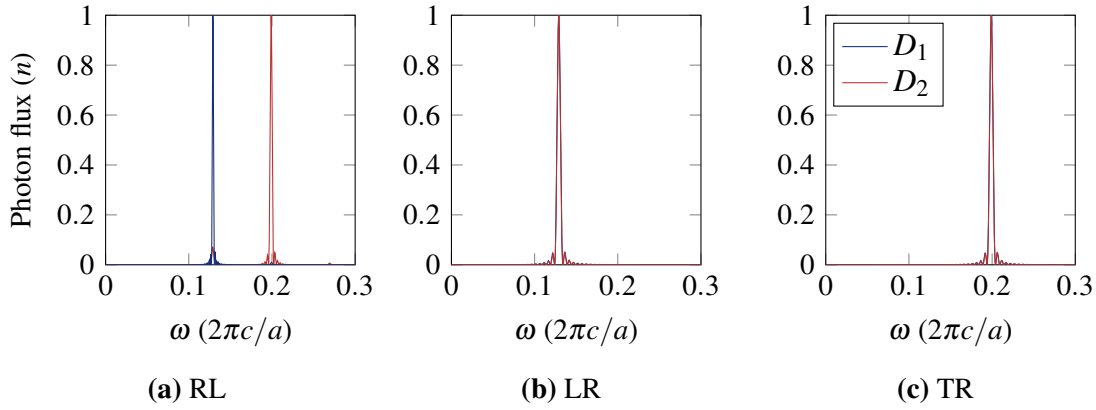
Figure 5.11: Frequencies of the optical Aharonov-Bohm effect for detector D_1 at $1.5\mu m$ and detector D_2 at $58\mu m$ for **(a)** left to right **(b)** right to left, and **(c)** time-reversed directions. Note that for all graphs, both D_1 and D_2 are shown, however there is an overlap in the LR and TR paths.

In Figures 5.8, 5.9, and 5.10 there is an excellent agreement between the transfer matrix formalism and the simulations. Importantly, there is complete TR and PT-symmetry breaking, implying total non-reciprocal mode conversion based on interference through the photonic AB effect. Of interesting consequence is the generation of an additional sidebands at frequencies that are not defined in the dispersion relation ($\omega_1 - \Omega$ and $\omega_1 - 2\Omega$). As such, the field is distributed as a *superposition* of several possible transverse electric modes, which can be safely neglected owing to their low modal amplitude. These spurious modes are 'leaky', implying the superposition contains modes close to or above the light cone of the band-structure. However, the existence of the leaky modes gives insight into the amount of energy lost as a result of modulation. Likewise, the effectively vanishing modal amplitudes near 0 and $60\,\mu m$ are due to the absorbing boundary conditions of the PML layer. In Figure 5.11, the result of extracting the frequencies for additional detectors D_1 and D_2 placed at 1.5 and $58\,\mu m$ respectively are shown. As is expected, the LR direction completely converts $|1\rangle$ to $|2\rangle$, whilst the RL and TR directions are not affected, as summarised in Table 5.1. In comparison with the indirect modulation of 5.2, these modes can be removed using widely available passive modal filters, allowing for broadband optical isolation.

Direction	Input	Output
Left to right (LR)	$|1\rangle$	$|2\rangle$
Right to left (RL)	$\langle 1|$	$\langle 1|$
Time-reversed (TR)	$\langle 2|$	$\langle 2|$

Table 5.1: Summary of mode transitions in the photonic AB effect.

It is worth pointing out that in the gauge potentials discussed for both moving media and dynamic modulations, all operations on the photon modes belong to the group of complex unitary ($U^\dagger = U^{-1}$) 2×2 matrices with determinant 1, known as special unitary $SU(2)$. However, the gauge transformation itself is given by setting a single phase factor between both states $|1\rangle$ and $|2\rangle$. Since there is only a single phase difference that can be set, the gauge degree of freedom belongs to the group of complex unitary 1×1 matrices, $U(1)$. This is identical to the gauge symmetry of the magnetic vector potential in electromagnetism [93].

5.4 Feasibility of modulation strengths

Here, the feasibility of achieving such modulation strengths on a waveguide are discussed. Current state of the art silicon modulators can achieve modulation frequencies upwards of $20GHz$, at a modulation strength of $\delta/\varepsilon = 5 \times 10^{-4}$ [109]. In previous simulations, a significantly larger modulation strength was used ($\delta/\varepsilon = 0.1$). The choice of the stronger modulation strength was two-fold. On one hand, a stronger modulation corresponds directly to a shorter coherence length, allowing the simulation to be far smaller than otherwise practical. Likewise, the response of the mode transitions discussed here are purely linear, that is, the modal transition is independent of the amplitude and phase of the incident light. Owing to this linearity, the photonic AB isolator can be scaled to effectively any frequency within the given constraints. Previous works [54] have demonstrated such a photonic AB effect at radio frequencies, and have a possibility of scaling to the gigahertz frequency range. However, scaling both the waveguides and the modulation to optical frequencies is experimentally demanding. These permittivity modulations in silicon operate by applying an electric field to a material, resulting in an induced birefringence [109].

On top of the weak modulation strength, silicon modulators also suffer from *insertion loss*, which takes into account the amount of optical power that is lost as a result of adding the component to the circuit. These insertion losses scale inversely with device size, as a result of larger interactions with sidewall roughness (a characteristic of the light-matter interaction), however several recent works have noted a significant minimisation of these effects [110], [111]. The dominance of silicon in integrated circuits is unfortunate for photonics, as silicon is inherently restricted as an optical material for the purposes of modulation. This is because the crystal structure of silicon (centrosymmetric) ensures that the electro-optic modulation can never be linear in nature.

Throughout this thesis, the frequencies of light have been in the near-infrared to microwave regime. The ideal optical isolator would possess an infinite operating bandwidth operating at a high contrast ratio, whilst commonly used magneto-optic isolators operate

anywhere between the visible and microwave spectrum. To remain both in the micrometer scale while inducing photonic transitions, modulation strengths of upwards of $\delta/\varepsilon = 0.1$ are necessary.

5.5 Comparisons between FDTD and FDFD

The unique aspect of the FDFD simulation implemented in this thesis is that it can naturally represent electric field profiles and amplitudes at any sideband frequency, without any of the post-processing that would be typically required in time-domain simulations. In the time-domain simulations, obtaining Fourier transform puts further strain on the simulation. This is because the field must be sampled at every time-point - a relatively costly process. Although the Fourier transform can be split into chunks to reduce the memory footprint, field values must still be extracted. On the other hand, FDFD solves for the steady-state in a single calculation (the matrix inversion), and the frequencies can be simply extracted from the field matrix.

However, the matrix inversion on the wave matrix A requires specialised numeric solvers. This is because the wave matrix typically exceeds 50000×50000 entries. At a double-precision, the matrix would encompass several gigabytes of memory - far beyond the capabilities of current solvers, and most computers. Fortunately, a significant number of values in the wave matrix are 0, causing A to be highly sparse. As an example, a simulation of size 100×200 points at any discretisation would yield a wave matrix with $400,000,000$ discrete elements. Since most of these elements are 0, the memory required to store a single sparse matrix of this type is only one megabyte, in comparison to the six gigabytes required for a full matrix.

5.5.1 Convergence times

Here, the convergence times of the frequency and time domain simulations are considered. The difficulty in drawing benchmark comparisons between FDTD and FDFD lie in the inherently different techniques both methods use to approach a full-wave solution. FDTD operates by effectively 'brute-forcing' a solution over each time-step, whereas FDFD generates and then solves a matrix equation, independent of any meaningful time-step. Naturally, the solution obtained by FDFD is dependent not only on the spatial step chosen in the simulation, but also in the number of sidebands calculated.

To compare the speeds of time and frequency domain methods used here, the time until a steady-state for the time domain is obtained and compared to the time to convergence from the frequency domain solution. This is because the frequency domain method
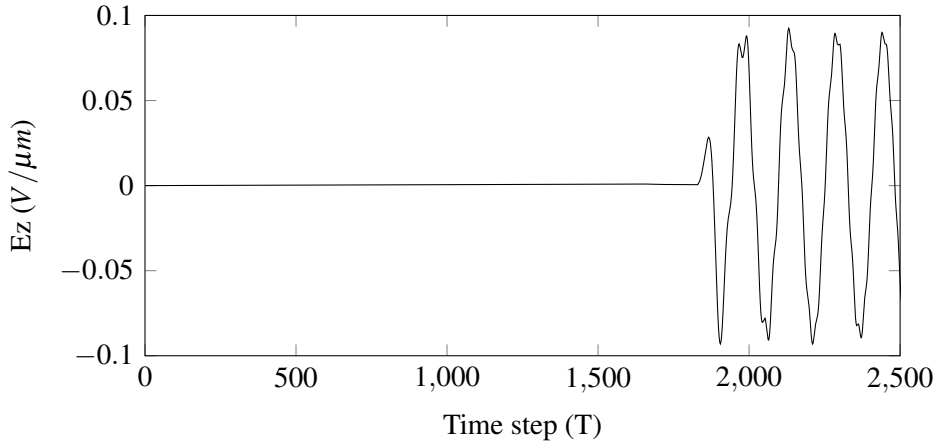
Figure 5.12: Steady state solution for the benchmark problem. A single point of the E_z field is sampled at the far end of the simulation, just within the PML boundary. The simulation is observed to reach a steady state after around 2000 time steps (667 fs in simulation time). Deviations in subsequent oscillations are due to reflections from the PML layer.

always yields the steady-state solution, whereas the time domain can simulate field propagation indefinitely, even after the steady-state is reached. To determine the time until the steady state fields are obtained for the time domain, a single probe is placed at the far end of the simulation, just within the boundaries of the PML layer. The probe collects a single value of the transverse electric field at every time-step. When the steady state solution is reached, the field will have no transient response as seen in Figure 5.12. Since sampling the field itself would slow down convergence, the simulation is run twice: the first time to obtain the *time step* of convergence, and the second without the probe to obtain the convergence till the given step. Convergence time in this case is simply the time (in seconds) for the complete simulation to run until the steady state. This value is different to the simulation time, which is the effective time inside the simulation. For example, it might take a single pulse $10\,s$ of convergence time to simulate $500\,fs$ of simulation time. Multiple convergence times are obtained for different resolutions, from a spatial step of $0.02\,\mu m$ up to $1\,\mu m$, with an average value taken for 3 benchmarks per spatial step. *MATLAB*'s inbuilt *tic* and *toc* functions are used to acquire the convergence time.

The first benchmark is a continuous $1\,\mu m$ wavelength source radiating in a $5 \times 5\,\mu m$ simulation space *in vacuo*, with a PML layer width of $0.1\,\mu m$. No modulation is applied in this case, to measure the impact that continuous updates of permittivity have on the time domain simulation. Similarly, without a modulation the frequency domain solution will have 0 sidebands to calculate over, drastically reducing the size of the wave matrix. The results of the benchmark are shown in Figure 5.13a. For the maximum resolution, the frequency domain takes $0.75 \pm 0.01\,s$ to converge, over an averaged 3 benchmarks per
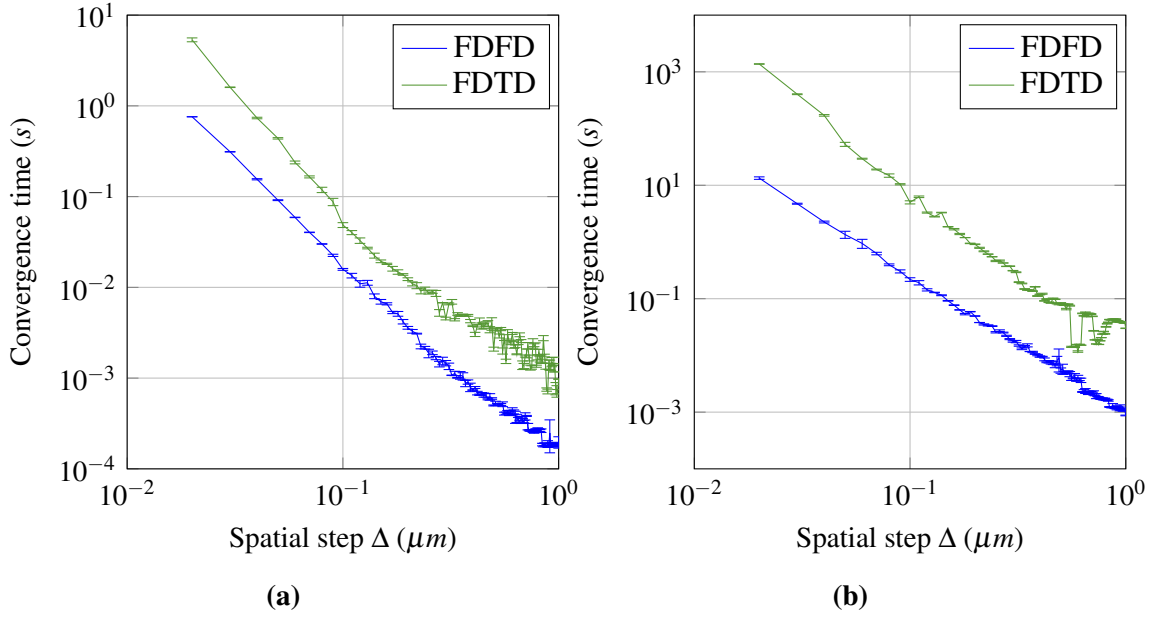
Figure 5.13: **(a)** Benchmark of a simple $5 \times 5\mu m$ simulation with a waveguide of $1.1\mu m$ width extending across horizontally. Only the $N = 0$ sideband is calculated for the FDFD, since no modulation occurs. **(b)** Comparison of convergence times for both the time and frequency domain simulations (with 3 sidebands) for the AB waveguide discussed in the previous chapter. The run-time was calculated by using *MATLABs* inbuilt *tic* and *toc* functions. A smaller spatial step corresponds to a larger resolution and consequently, improved accuracy

spatial step. The time domain takes $5.34 \pm 0.26\,s$ to converge, more than $7\times$ longer than the frequency domain.

The second benchmark program is the optical AB isolator of Section 5.3. This presents two new challenges for the simulation - a much larger computational domain (exceeding $60\,\mu m$) as well as two regions of modulation. Again, benchmarks are taken for spatial steps Δ from $0.02\,\mu m$ to $1\mu m$, with convergence times shown in Figure 5.13b. There is a much larger discrepancy between convergence times for the time and frequency methods. In fact, at the smallest spatial step of $0.02\,\mu m$, the frequency domain method takes $13.39 \pm 0.68\,s$, whereas the time domain method exceeds $1374.70 \pm 14.91\,s$ (around 22.9 minutes). For the purpose of the AB simulation then, the frequency method is just over $100\times$ faster. Of course, these benchmarks are preliminary and would require more thorough testing under different environments. However, the ability to rapidly prototype photonic devices and then simulate is obviously an appealing aspect. As integrated and topological photonics becomes more widespread, faster simulation methods are required. Thus, FDFD is quite well suited to dynamic modulations - the number of modulated regions does not adversely affect the convergence time. On the other hand, in the time domain, each modulation region requires an additional change of the permittivity tensor

at every time-step.

It is worth pointing out that even with the increase in speed FDFD brings, it is not always the ideal choice for simulating active photonics. This is because the frequency domain implementation can not calculate transient responses - that is, the final solution will always be in the steady-state. On the other hand, FDTD will always show the transient response of the system. Thus, *FDFD* is ideally suited in the case when only the steady-state solution is desired.

Although the FDTD code presented here has been extensively optimised, the benchmark would also ideally be performed with a publicly available FDTD solver. The most commonly used of these, *MEEP* [112], does not support time-dependent media. Regardless, a preliminary test in *MEEP* without modulation of the optical AB simulation showed around a 30% increase in speed over the *MATLAB* FDTD code, however the act of modulating the permittivity is a costly process in of itself, and thus no reliable benchmark can be obtained.

5.5.2 Numeric artefacts

Finite difference methods generally provide a good approximation to the real physical behaviour of fields. However, taking *finite* differences of normally continuous functions will inevitably introduce an error. For instance, the group velocity of a wave propagating in the Yee grid will in general differ from *c*. This discrepancy depends on several factors including the spatial grid size, direction of propagation, and even the frequency of incident light. Such errors are known as *dispersion*. Likewise, *FDTD* samples the electromagnetic field at points that are discrete in both time and space. The choice of these steps is thus important for maintaining the *stability* of the solution.

Another property of finite difference methods that can cause spurious results lie in the building of a material on the Yee grid. Since the Yee grid is a square lattice, it is impossible to completely place a curved structure over the grid. In every case, the structure will be represented on the grid as discrete blocks, regardless of the spatial step - an error known as staircasing. Since most of the simulations performed in this thesis were of rectangular or otherwise perfectly straight materials, staircasing will not contribute greatly to an error in the fields. Such effects can be minimised by taking an average of the surrounding permittivities, in a technique known as subpixel averaging.

Conclusion

In this thesis, full-wave finite difference time and frequency domain methods were developed for the investigation of non-reciprocal phase and mode conversions in a medium undergoing dynamic modulation. The frequency domain solution was shown to provide a remarkable increase in convergence time over the time domain solution through preliminary benchmarks, and is uniquely suited to simulating active nanophotonic devices. Since finite difference methods are suitable to solve a large number of differential equations (not being limited to just Maxwell's equations), the multi-frequency method is ideal for simulating devices with arbitrarily separated frequencies. The frequency domain simulations of the photonic gauge potential emerging from modulation marks the first of their kind outside the time-domain. Owing to the slow convergence time of FDTD, previous works relied on a combination of FDTD and coupled-mode theory to probe the dynamics of systems undergoing modulation. However, the frequency domain method is capable of obtaining these dynamics at a much faster speed, and is obviously appealing for rapid prototyping of devices in photonics.

The case of a moving media and a dynamically modulated waveguide were also shown to generate a non-reciprocal phase for light, leading to an invariance that is typical of gauge potentials. In particular, a photonic transition between two states was shown to correlate perfectly with electrons hopping between sites on a $1D$ tight-binding lattice under the influence of a magnetic vector potential. Consequently, the phase in the dynamic modulation scheme is directly equivalent to a gauge degree of freedom. On the macroscopic scale, a similar effect was derived for light in a rotating dielectric.

Non-reciprocal frequency conversion was demonstrated numerically in the case of a spatio-temporal refractive index modulation. However, as applying spatial modulations is significantly more difficult to engineer than temporal modulations, the gauge potential emerging from the phase of dynamic modulation was used to demonstrate a photonic AB effect that was characterised by complete non-reciprocal mode conversion. Despite the photonic AB effect using direct transitions, which are inherently reciprocal, the gauge potential resulted in a non-reciprocal mode conversion between the LR, RL, and TR paths. In comparison to the indirect transition which required a spatio-temporal modulation, the

57

direct transition is far simpler to achieve using current modulation technology. Characteristic oscillations emerging from the direct modulation were also shown to correspond to highly phase mismatched backward propagating modes. The choice of modulation scheme for the AB interferometer forms the absolute minimum number of modulation regions that can be used to generate a gauge potential for light.

Photonic circuits are currently hampered by imperfections in the manufacturing process, so a method to bypass flaws via synthetic gauge fields would be hugely significant. Exploitation of topological effects dramatically improves the robustness of current photonic devices, including optical isolators, which currently require magneto-optic coupling effects and are largely incompatible with integrated photonics. Likewise, the topologically non-trivial properties of light could solve key limitations involving the disorder of light in waveguides and potentially improve coherence in quantum computing. In-fact, protected edge states arising from TR-invariant topological phases would be one-way, even in reciprocal systems, making current optical isolators unnecessary. The main challenge in dynamic modulation schemes mostly lies within engineering difficulties associated with modulating coupled resonators on the micro-scale.

Going further, the recent introduction of synthetic dimensions is potentially an important step towards realising higher-dimensional topology in photonics. The investigation of Weyl points on a 2D planar structure makes it far more experimentally viable than current architectures, and is amenable with integrated photonics in both the infrared and visible wavelengths. The idea of Weyl points in 2D systems with synthetic dimensions can be implemented in more than just dynamically modulated honeycomb lattice systems. Additionally, a 4D quantum hall effect proposed, based on a 3D coupled resonator system with an additional frequency dimension, allows for unique photon-photon interactions in 3D systems, and could potentially realise fractional quantum hall physics for light. Exciting applications of these approaches would obviously be the observation of a 4D quantum Hall effect experimentally. Further, the edge physics associated with a 4D Hall effect would be expected to propagate along the 3D surface of a 4D boundary. Such modes would have useful applications in future optical components, paving the way towards a complete integrated photonic platform for manipulating light at the microscale.

Future work

Experimental demonstration of non-reciprocity would be ideal, and could be accomplished using the theoretical procedures derived in Chapter 2 for either moving media or dynamic modulation. In particular, the macroscopic AB effect from the rotating dielectric is promising, despite being incompatible with integrated photonics. Scaling the photonic AB effect in dynamic modulation up to the range of radio frequencies would allow for experimentally feasible investigation of the synthetic gauge potentials in modulation.

On the simulation front, more rigorous benchmarks of the time and frequency domain simulations are desirable. In particular, instead of sampling one point in the simulation space to obtain the steady-state convergence time for FDTD, all points would be sampled concurrently. Although this would dramatically increase the convergence time, the resulting benchmark would be far more rigorous. Additionally, the impact of the number of sidebands on the convergence in FDFD could be identified.

Rewriting the main FDFD functions in a naturally faster language, such as *C++* would net a significant increase in speed, as well as writing a customised matrix inversion solver that uses iterative techniques instead of *MATLAB's* built-in UMFPACK. UMFPACK is a general purpose matrix solver, and thus it takes several steps of analysis before it decides on a suitable iteration method. Since the wave matrix is highly ill-conditioned, a preconditioning scheme could be developed before inversion is performed. Alternative iterative techniques could include the commonly used biconjugate gradient method [113], or the quasi-minimal residual method [114]. Likewise, the simulation is readily extensible to three dimensions, however at this point any performance gains through the use of FDFD are largely outweighed by the exponential increase in complexity that comes with simulating extra dimensions. Regardless, recent work by Shin et al. (2012) has shown that several methods can be used to greatly increase the speed of FDFD methods by optimal choice of the PML layer type, making it amenable to *3D* implementation [105].

Appendix A

Derivations

A.1 Minkowski relations

The Minkowski relations describe how electromagnetic fields transform between reference frames. Consider the frame Γ' in which a medium is moving with velocity $v\hat{x}$ relative to an observer in the rest frame Γ. In the primed frame, the basic constitutive equations for electromagnetic fields in the media obey

$$\boldsymbol{D'} = \varepsilon \boldsymbol{E'}, \tag{A.1}$$

$$\boldsymbol{B'} = \mu \boldsymbol{H'}, \tag{A.2}$$

where μ and ε represent the permeability and permittivity of the medium respectively, $\mu = \mu_0 \mu_r$ and $\varepsilon = \varepsilon_0 \varepsilon_r$. The most direct method of transforming between reference frames in electromagnetism involves the use of the electromagnetic field tensor $F^{\mu\nu}$ defined in its contravariant form by

$$F^{\mu\nu} = \begin{bmatrix} 0 & E_x/c & E_y/c & E_z/c \\ -E_x/c & 0 & B_z & -B_y \\ -E_y/c & -B_z & 0 & B_x \\ -E_z/c & B_y & -B_x & 0 \end{bmatrix}. \tag{A.3}$$

It is well known that the Lorentz equations transform coordinates between relatively moving reference frames. In the form of a mixed tensor for a Lorentz boost along $\hat{x}$,

$$\Lambda^{\mu}{}_{\nu} = \begin{bmatrix} \gamma & -\gamma\beta & 0 & 0 \\ -\gamma\beta & \gamma & 0 & 0 \\ 0 & 0 & 1 & 0 \\ 0 & 0 & 0 & 1 \end{bmatrix} \tag{A.4}$$

where $\gamma = 1/\sqrt{1-\beta^2}$ and $\beta = v/c$. The electromagnetic field tensor is transformed by the Lorentz boost according to standard tensor notation as

$$F'^{\mu\nu} = \Lambda^{\mu}{}_{\alpha}\Lambda^{\nu}{}_{\beta}F^{\alpha\beta} = \Lambda^{\mu}{}_{\alpha}F^{\alpha\beta}\Lambda^{\nu}{}_{\beta} = (\Lambda F \Lambda^{T})^{\mu\nu}, \tag{A.5}$$

where T represents the transpose of the matrix. For a rank 2 asymmetric tensor, there are only 6 independent terms. Explicitly calculating this transformation yields the tensor in the primed frame

$$F'^{\mu\nu} = \begin{bmatrix} 0 & E_x/c & \gamma(E_y/c - \beta B_z) & \gamma(E_z/c + \beta B_y) \\ -E_x/c & 0 & \gamma(B_z - \beta E_y/c) & -\gamma(\beta E_z/c + B_y) \\ \gamma(\beta B_z/c - E_y) & \gamma(\beta E_y/c - B_z) & 0 & B_x \\ -\gamma(E_z/c + \beta B_y) & \gamma(\beta E_z/c + B_y) & -B_x & 0 \end{bmatrix}, \tag{A.6}$$

which completely describes how the E and B fields transform with respect to motion along the $\hat{x}$ direction. By comparison with the original electromagnetic tensor A.3, the variation of the field components in the primed frame can be examined,

$$E'_x = E_x \qquad E'_y = \gamma(E_y - \beta B_z) \qquad E'_z = \gamma(E_z + \beta B_y) \tag{A.7}$$

$$B'_x = B_x \qquad B'_y = \gamma(\beta E_z + B_y) \qquad B'_z = \gamma(\beta E_z - \beta E_y). \tag{A.8}$$

These field components can further be resolved into their parallel ($\|$) and perpendicular ($\perp$) components relative to $v\hat{x}$,

$$E'_{\|} = (\boldsymbol{E} + \boldsymbol{v} \times \boldsymbol{B})_{\|} \qquad E'_{\perp} = \gamma(\boldsymbol{E} + \boldsymbol{v} \times \boldsymbol{B})_{\perp} \tag{A.9}$$

$$B'_{\|} = (\boldsymbol{B} - \frac{1}{c^2}\boldsymbol{v} \times \boldsymbol{E})_{\|} \qquad B'_{\perp} = \gamma(\boldsymbol{B} - \frac{1}{c^2}\boldsymbol{v} \times \boldsymbol{E})_{\perp}. \tag{A.10}$$

Where the fact that $(\boldsymbol{v} \times \boldsymbol{B})_{\|} = 0$ has been used to incorporate the B field into $E_{\|}$. By replacing $\boldsymbol{E}$ with $c\boldsymbol{D}$ and $\boldsymbol{B}$ by $\frac{H}{c}$, similar relations for the D and H fields can be obtained,

$$H'_{\parallel} = (H - v \times D)_{\parallel} \qquad H'_{\perp} = \gamma(H - v \times D)_{\perp} \tag{A.11}$$

$$D'_{\parallel} = (D + \frac{1}{c^2} v \times H)_{\parallel} \qquad D'_{\perp} = \gamma(D + \frac{1}{c^2} v \times H)_{\perp}. \tag{A.12}$$

Substituting Equations A.9 through A.12 into A.1 and A.2 for both the parallel and perpendicular components, yields the following set of relationships;

$$D + \frac{1}{c^2} v \times H = \varepsilon(E + v \times B) \tag{A.13}$$

$$B - \frac{1}{c^2} v \times E = \mu(H + v \times D). \tag{A.14}$$

A.2   Direct photonic transitions through coupled-mode theory

Here, we provide the derivation of the coupled mode equation that describes the dynamics of power exchange between modes in a waveguide structure undergoing modulation (as used to validate the FDFD method). Beginning with Maxwell's equations for a time-dependent permittivity,

$$\nabla \times E(r,t) = -\mu_0 \frac{\partial H(r,t)}{\partial t} \tag{A.15}$$

$$\nabla \times H(r,t) = \varepsilon_0 \frac{\partial \varepsilon_r(r,t) E(r,t)}{\partial t}. \tag{A.16}$$

For a transverse electric (TE) wave, the electric field is only non-vanishing in z. In this case, the scalar electric field $E(x,y,t) = E_z(x,y,z)$ satisfies the wave equation

$$\nabla^2 E(x,y,t) = \mu_0 \varepsilon_0 \frac{\partial^2 \varepsilon_r(x,y,t) E(x,y,t)}{\partial t^2}. \tag{A.17}$$

Suppose now that we are interested only in $2N + 1$ sideband modes at frequencies that are separated by the modulation frequency, Ω. The electric field can then be written as the sum of modes propagating along x,

$$E(x,y,t) = \Re\{ \sum_{n=-N}^{N} a_n(x) e^{-i\beta_n x} \hat{E}_n(y) e^{i\omega_n t} \} \tag{A.18}$$

where $w_n = w_0 + n\Omega$, a_n is the modal amplitude, $\beta = 2\pi k$ is the propagation constant

at each sideband, and $\hat{E}_n(y)$ is the modal profile of the field. The modal profiles are normalised through the orthogonality condition, so that for a pair of modes $\hat{E}_m(y)$ and $\hat{E}_n(y)$,

$$\int_{-\infty}^{\infty} dy \hat{E}_m^*(y)\hat{E}_n(y) = \frac{2\omega_m\mu_0}{\beta_m}\delta_{mn}, \tag{A.19}$$

such that $|a_n(x)|^2$ gives the power of the n-th mode as usual. Now, consider the standard modulation of the form

$$\varepsilon(t) = \varepsilon_{wg} + \delta\cos(\Omega t + \phi). \tag{A.20}$$

Substituting the above modulation and A.18 into equation A.17 yields

$$\sum_{n=-N}^{N} \left[a_n e^{-i\beta_n x}\partial_y^2 \hat{E}_n(y)e^{i\omega_n t} - (\beta_n^2 a_n + 2i\beta_n \frac{da_n}{dx})e^{-i\beta_n x}\hat{E}_n(y)e^{i\omega_n t} \right] =$$
$$\sum_{n=-N}^{N} \left[\mu_0\varepsilon_0\varepsilon_{wg}(-\omega_n^2)a_n e^{-i\beta_n x}\hat{E}_n(y)e^{i\omega_n t} + \mu_0\varepsilon_0\delta a_n e^{-i\beta_n x}\hat{E}_n \frac{\partial}{\partial t}\left(e^{i\omega_n t}\cos(\Omega t + \phi) \right) \right], \tag{A.21}$$

where $d^2 a_n/dx^2$ has been ignored as it is slowly-varying. For $\hat{E}_n(y)$ to be a mode of an unmodulated waveguide, it must satisfy the mode equation,

$$(\partial_y^2 - \beta_n^2)\hat{E}_n(y) = -\mu_0\varepsilon_0\varepsilon_{wg}\omega_n^2 \hat{E}_n(y). \tag{A.22}$$

Combining the above equation with A.21 reduces it to the form

$$\sum_{n=-N}^{N} 2i\beta_n \frac{da_n}{dx} e^{-i\beta_n x}\hat{E}_n(y)e^{i\omega_n t} = \sum_{n'=-N}^{N} \mu_0\varepsilon_0 \frac{\delta}{2} a_{n'} e^{-i\beta_{n'} x}\hat{E}_{n'}(y)\left[\omega_{n'1}^2 e^{i\omega_{n'+1}t} + \omega_{n'-1}^2 e^{i\omega_{n'-1}t} \right]. \tag{A.23}$$

Maintaining the $n = n' + 1$ and $n = n' - 1$ terms on the right-hand side of the above equation, we obtain

$$\hat{E}_n(y)\frac{da_n}{dt} = -i\frac{\mu_0\varepsilon_0\omega_n^2}{4\beta_n}\delta(y)\left[\hat{E}_{n-1}(y)e^{-i(\beta_{n-1}-\beta_n)x}a_{n-1} + \hat{E}_{n+1}(y)e^{-i(\beta_{n+1}-\beta_n)x}a_{n+1} \right]. \tag{A.24}$$

Applying the orthogonality condition results in the coupled mode equation for power exchange amongst adjacent eigenmodes in a modulated waveguide,

$$i\frac{da_n(x)}{dx} = C_{n,n-1}(x)a_{n-1}(x) + C_{n,n+1}(x)a_{n+1}(x), \tag{A.25}$$

where

$$C_{n,m}(x) = \frac{\varepsilon_0 \omega_n}{8} e^{-i(\beta_m - \beta_n)x} \int_{-\infty}^{\infty} dy \, \delta(y) \hat{E}_n(y)^* \hat{E}_m(y). \tag{A.26}$$

With an N-th term truncation, the coupled mode equation can be written in the form

$$\frac{d}{dx}\begin{bmatrix} a_{-N} \\ \vdots \\ a_0 \\ \vdots \\ a_N \end{bmatrix} = -i \begin{bmatrix} 0 & C_{-N,-N+1} & \cdots & \cdots & 0 \\ \vdots & \ddots & & & \vdots \\ 0 & C_{0,-1} & 0 & C_{0,1} & 0 \\ \vdots & & & \ddots & \vdots \\ 0 & \cdots & \cdots & C_{N,N-1} & 0 \end{bmatrix} \begin{bmatrix} a_{-N} \\ \vdots \\ a_0 \\ \vdots \\ a_N \end{bmatrix} \tag{A.27}$$

which can be represented as simply

$$\frac{da(x)}{dx} = -iK(x)a(x), \tag{A.28}$$

where $K(x) \in \mathbb{C}^{(2N+1)\times(2N+1)}$ is non-zero only along the off diagonal entries. Fortuitously, equation A.28 can be solved by applying 1D finite differences, where x is discretised with step size Δx, so that $x_n = x_0 + n\Delta x$. This allows for the calculation of how the amplitude of modes varies with x in a modulated region of a waveguide, given the coupling coefficients between modes (see Appendix B.1 for the *MATLAB* implementation).

Appendix B

MATLAB and Scheme code

In this appendix, *MATLAB* code written for the time and frequency domain simulations is presented, as well as the analytic mode solvers. For brevity, only the main functions have been included to show how the update equations are solved. Input files for the simulations are not listed and can be provided on request.

B.1   Finite Difference

```matlab
function [beta, kz, alpha, Ey, A, y_vec] = beta_sym(L0, wvlen, d, eps1, eps2, m, hy, pts)
%% This function implements the mode equation (4.20) for input wavelength, waveguide
      width, and permittivity.
%% It returns the propagation constant, k_z wavevector, and a normalised electric field
      profile
constants;         % Import constants
omega = 2*pi*c0 / wvlen;          %set frequency
kz_max = omega .* sqrt(u0 * e0 * (eps2 - eps1)); % Calculate k_z wavevector
alpha_z1 = @(kz) sqrt(kz_max^2 - kz.^2);         % Define function handles
alpha_z_even = @(kz) kz .* tan(kz * d);
alpha_z_odd = @(kz) kz .* tan(kz * d + pi/2);
trans_eqn_even = @(kz) alpha_z1(kz) - alpha_z_even(kz);
trans_eqn_odd = @(kz) alpha_z1(kz) - alpha_z_odd(kz);

if (mod(m, 2) == 0)
    % Even mode
    kz = eqn_solve(trans_eqn_even, (m/2)*pi/d, pi/2/d + (m/2)*pi/d);
else
    % Odd mode
    kz = eqn_solve(trans_eqn_odd, pi/2/d + (m-1)*pi/2/d, pi/d + (m-1)*pi/2/d);
end
beta = sqrt(omega^2 * u0*e0 * eps2 - kz^2);       % Propagation constant
alpha = sqrt(beta^2 - omega^2 * u0*e0 * eps1);
ylim = pts * hy;
y_vec = [-ylim+hy/2 : hy : ylim+hy/2]';
Ey_even = @(y) (y > d).*cos(kz*d) .* exp(-alpha * (y-d)) + ...
              (y < -d).*cos(kz*d) .* exp(alpha * (y+d)) + ...
              (abs(y)<d).*cos(kz*y);
Ey_odd = @(y) (y > d).*sin(kz*d) .* exp(-alpha * (y-d)) + ...
              (y < -d).*sin(kz*d) * (-1) .* exp(alpha * (y+d)) + ...
              (abs(y)<=d).*sin(kz*y);
if (mod(m, 2) == 0)
    Ey = Ey_even(y_vec);
else
    Ey = Ey_odd(y_vec);
end
%% Normalisation
mode_integral = sum(hy * Ey.^2);
A = sqrt(2 * omega * u0 / (beta * mode_integral));
Ey = A*Ey;
```

```matlab
39    end
```

```matlab
1    function [a, x] = cmt_coupling(beta, kp_vec, km_vec, a0, hx, xf)
2    %% This function implements the equation A.15 to describe power exchange under multiple
          modes in a modulated waveguide, given inputs of propagation constant, and coupling
          coefficients between modes
3    M = length(beta);     % Number of propagation constants
4    x = 0:hx:xf;          % Define x space with hz step
5    N = length(x);        % Obtain length of x
6    a = zeros(M, N);         % CMT results, for M couplings
7    del_beta = diff(beta);
8    kp_x = @(x) kp_vec .* exp(-1i * del_beta * x);  % Coupling up
9    km_x = @(x) km_vec .* exp(+1i * del_beta * x);  % Coupling down
10   K = @(x) diag(kp_x(x), 1) + diag(km_x(x), -1);  % K matrix (Eqtn A.14)
11   a(:, 1) = a0;
12   % Finite difference scheme
13   for i = 2:N
14       a(:, i) = a(:, i-1) - 1i*K(x(i)) * hx * a(:, i-1); % Eqtn A.15
15   end
16   end
```

B.1.1 Time domain

```matlab
1    %% This script calculates the time-marching equations for the FDTD method, and is
          presented for the optical AB waveguide.
2    %% Initialise
3    clc; clear all;
4    mode = 0;
5    constants;
6
7    %% Define grid
8    xrange = [0 5];                 % x boundaries in L0
9    yrange = [0 60];                % y boundaries in L0
10   NPML = [20 20 20 20];           % PML width
11   dx = 0.01; dy = 0.01;           % Spatial step
12   N = [ceil(diff(xrange)/dx) ceil(diff(yrange)/dy)];
13
14   %% Define source
15   wavelength = (1/0.129);          % Initial wavelength
16   wavelength_target = (1/0.199);   % Target wavelength
17   Omega = 2*pi*c0* (1/wavelength_target - 1/wavelength);
18   frequency = c0/wavelength;
19   frequency2 = c0/wavelength_target;
20   omeg = 2*pi/wavelength;
21   src_x = (ceil(1.95/dx):ceil(3.05/dx));
22   src_y = ceil(1/dy);
23
24   %% Pre-allocate material space
25   mu_space_xx = ones(N);  mu_space_yy = ones(N);  %permeability
26   eps_space = ones(N);            % eps_zz
27   eps_wg = 12.25;                 % eps_wg
28
29   %% Waveguide dimensions: defines initial permittivity
30   wg_upper = 3.05;                % W.g. of width 1.1 microns
31   wg_lower = 1.95;
32   within_wg = @(x, y) x > wg_lower & x < wg_upper;
33   central_guide = @(x, y) y>24.2 & y<35.8 & x >1.5 & x<3.5;
34   eps_space = assign_space(eps_space, xrange, yrange, within_wg, eps_wg);
35   eps_space = assign_space(eps_space, xrange, yrange, central_guide, eps_wg);
36
37   %% Modulation space: defines region of modulation
38   modLeft = @(x, y) y> 5.2 & y<24.2 & x > 2.5 & x < wg_upper;
39   modRight = @(x, y) y> 35.8 & y<54.8 & x > 2.5 & x < wg_upper;
40   modulation_array = {modLeft, modRight};
41   phase_array = [0, pi/2];
42
43   %% Compute source
44   dmin = min([dx dy]);
45   dt = dmin/(2*c0);
46
47   % Calculate modes using dispersion solver
48   [~, ~, ~, Ez_src, ~, ~] = beta_sym(L0, wavelength, (1.1/2), 1, eps_wg, 0, dx, 40);
49
50   %% Compute PML: (code adapted from R. Rumpf's lectures on FDTD)
51   Nx2 = 2*N(1); Ny2 = 2*N(2);
```

```matlab
52  sigx = zeros(Nx2,Ny2);
53  for nx = 1 : 2*NPML(1)
54      nx1 = 2*NPML(1) - nx + 1;
55      sigx(nx1,:) = (0.5*e0/dt)*(nx/2/NPML(1))^3;
56  end
57  for nx = 1 : 2*NPML(2)
58      nx1 = Nx2 - 2*NPML(2) + nx;
59      sigx(nx1,:) = (0.5*e0/dt)*(nx/2/NPML(2))^3;
60  end
61  sigy = zeros(Nx2,Ny2);
62  for ny = 1 : 2*NPML(3)
63      ny1 = 2*NPML(3) - ny + 1;
64      sigy(:,ny1) = (0.5*e0/dt)*(ny/2/NPML(3))^3;
65  end
66  for ny = 1 : 2*NPML(4)
67      ny1 = Ny2 - 2*NPML(4) + ny;
68      sigy(:,ny1) = (0.5*e0/dt)*(ny/2/NPML(4))^3;
69  end
70
71  %% Compute update coefficients (Adapted from R. Rumpf)
72  % Hx coefficients
73  sigHx = sigx(1:2:Nx2,2:2:Ny2); sigHy = sigy(1:2:Nx2,2:2:Ny2);
74  mHx0 = (1/dt) + sigHy/(2*e0);
75  mHx1 = ((1/dt) - sigHy/(2*e0))./mHx0;
76  mHx2 = - c0./mu_space_xx./mHx0;
77  mHx3 = - (c0*dt/e0) * sigHx./mu_space_xx ./ mHx0;
78  % Hy coefficients
79  sigHx = sigx(2:2:Nx2,1:2:Ny2); sigHy = sigy(2:2:Nx2,1:2:Ny2);
80  mHy0 = (1/dt) + sigHx/(2*e0);
81  mHy1 = ((1/dt) - sigHx/(2*e0))./mHy0;
82  mHy2 = - c0./mu_space_yy./mHy0;
83  mHy3 = - (c0*dt/e0) * sigHy./mu_space_yy ./ mHy0;
84  % Dz coefficients
85  sigDx = sigx(1:2:Nx2,1:2:Ny2); sigDy = sigy(1:2:Nx2,1:2:Ny2);
86  mDz0 = (1/dt) + (sigDx + sigDy)/(2*e0) + sigDx.*sigDy*(dt/4/e0^2);
87  mDz1 = (1/dt) - (sigDx + sigDy)/(2*e0) - sigDx.*sigDy*(dt/4/e0^2);
88  mDz1 = mDz1 ./ mDz0;
89  mDz2 = c0./mDz0;
90  mDz4 = - (dt/e0^2)*sigDx.*sigDy./mDz0;
91  % Ez coefficient
92  mEz1 = 1./eps_space;
93
94  %% Pre-allocate variable memory
95  % Electromagnetic fields (TE)
96  Hx = zeros(N); Hy = zeros(N);
97  Dz = zeros(N); Ez = zeros(N);
98  % Curls
99  CEx = zeros(N); CEy = zeros(N); CHz = zeros(N);
100 % Integration
101 ICEx = zeros(N); ICEy = zeros(N); IDz = zeros(N);
102
103 %% Minor pre-loop optimisations
104 f = 1i*2*pi*frequency;
105 Nx = N(1); Ny = N(2);
106 mod_array_length = length(modulation_array);
107 %% Calculation loop
108 for T=1:50000
109     % Curl Ex
110     CEx(1:Nx,1:Ny-1) = (Ez(1:Nx,2:Ny) - Ez(1:Nx,1:Ny-1))./dy;
111     CEx(1:Nx,Ny) = (Ez(1:Nx,1) - Ez(1:Nx,Ny))./dy;
112     % Curl Ey
113     CEy(1:Nx-1,1:Ny) = - (Ez(2:Nx,1:Ny) - Ez(1:Nx-1,1:Ny))./dx;
114     CEy(Nx,1:Ny) = - (Ez(1,1:Ny) - Ez(Nx,1:Ny))./dx;
115     % Ez source
116     ezsrc = real(Ez_src*exp(-f*(T-1)*dt));
117     CEx(src_x,src_y) = CEx(src_x,src_y) - ezsrc/dy;
118     % Integration terms
119     ICEx = ICEx + CEx;
120     ICEy = ICEy + CEy;
121     % Update Hx and Hy
122     Hx = mHx1.*Hx + mHx2.*CEx + mHx3.*ICEx;
123     Hy = mHy1.*Hy + mHy2.*CEy + mHy3.*ICEy;
124     % Curl Hz
125     CHz(1,1) = (Hy(1,1) - Hy(N(1),1))/dx - (Hx(1,1) - Hx(1,N(2)))/dy;
126     CHz(2:Nx,1) = (Hy(2:Nx,1) - Hy(1:Nx-1,1))./dx - (Hx(2:Nx,1) - Hx(2:Nx,Ny))./dy;
127     CHz(1,2:Ny) = (Hy(1,2:Ny) - Hy(Nx,2:Ny))./dx - (Hx(1,2:Ny) - Hx(1,1:Ny-1))./dy;
128     CHz(2:Nx,2:Ny) = (Hy(2:Nx,2:Ny) - Hy(1:Nx-1,2:Ny))./dx - (Hx(2:Nx,2:Ny) - Hx(2:Nx,1:(Ny-1)))./dy;
129     IDz = IDz + Dz;
130     Dz = mDz1.*Dz + mDz2.*CHz + mDz4.*IDz;
131     Ez = mEz1.*Dz;
```

```matlab
132
133         %% Modulate permittivity
134         for i = 1:mod_array_length
135             eps_space = assign_space(eps_space, xrange, yrange, modulation_array{i}, (eps_wg
                    + 0.1*eps_wg*cos(Omega * T * dt+phase_array(i))));
136         end
137         mEz1 = 1./eps_space;
138 end
```

B.1.2 Frequency domain

```matlab
 1 function [Ez, Hx, Hy, omega, A] = solve_frequency(L0, wvlen0, Omega, Nsb, xrange, yrange
      , eps_r, mod_reg, mod_phi, Jz0, Npml)
 2 %% This function performs an implementation of the MF–FDFD method described in section
      4.3.2. The inputs are the normalisation constant L0, initial wavelength wvlen0,
      modulation frequency Omega, matrices containing the x and y range of the simulation,
      and the permittivity and modulation matrices (eps_r, mod_reg)
 3 constants                          % Import constants file
 4 N = size(eps_r);                   % [N(1) N(2)]
 5 L = [diff(xrange) diff(yrange)];   % [Lx Ly]
 6 dL = L./(N);                       % [dx dy]
 7 M = prod(N);
 8
 9 omega0 = 2*pi*c0/wvlen0;           % Angular frequency
10 n_sb = -Nsb : 1 : Nsb;             % Sideband array
11 omega = omega0 + Omega*n_sb;       % Sideband frequency array
12 wvlen = 2*pi*c0./omega;            % Wavelength frequency array
13
14 %% Implement PML equations
15 Sxf = cell(2*Nsb+1, 1);
16 Sxb = cell(2*Nsb+1, 1);
17 Syf = cell(2*Nsb+1, 1);
18 Syb = cell(2*Nsb+1, 1);
19 for i = 1 : (2*Nsb + 1)
20     [Sxf{i}, Sxb{i}, Syf{i}, Syb{i}] = S_create(L0, wvlen(i), xrange, yrange, N, Npml);
21 end
22
23 %% Setup space
24 % Reshape epsilon and phi into 1D array
25 vector_eps = reshape(e0 * eps_r, M, 1); vec_phi = reshape(mod_phi, M, 1);
26 % Create T diags
27 T_eps = spdiags(vector_eps, 0, M, M); T_phi = spdiags(exp(1i*vec_phi), 0, M, M);
28
29 %% Build derivative matrices
30 for n = 0 : 1 : N(2)-1
31     block_y(1 + n*N(1) : (n+1)*N(1) , 1 + n*N(1) : (n+1)*N(1)) = -speye(N(1));
32     if (n < N(2) - 1)
33         block_y(1 + n*N(1) : (n+1)*N(1) , 1 + (n+1)*N(1) : (n+2)*N(1)) = speye(N(1));
34     else
35         block_y(1 + n*N(1) : (n+1)*N(1) , 1 : N(1)) = speye(N(1));
36     end
37 end
38 Dyf(1 : (1)*(N(1)*N(2)) , 1:(1)*(N(1)*N(2))) = 1/dL(2) * block_y;
39 Dyb = -transpose(Dyf);
40 block_x = -speye(N(1)) + circshift(speye(N(1)), -1);
41 for n = 0 : 1 : (N(2)*1 - 1)
42     Dxf(1 + n*N(1) : (n+1)*N(1), 1 + n*N(1) : (n+1)*N(1)) = 1/dL(1) * block_x;
43 end
44 Dxb = -transpose(Dxf);
45
46 %% Reshape Jz0 into a vector
47 jz0 = reshape(Jz0, M, 1);
48
49 %% Construct A matrix and b vector
50 A_i = cell(2*Nsb+1, 1);
51 for i = 1 : (2*Nsb + 1)
52     A_i{i} = Sxb{i}*Dxb * u0^-1 * Sxf{i}*Dxf + Syb{i}*Dyb * u0^-1 * Syf{i}*Dyf + omega(i
          )^2*T_eps;
53 end
54 b0 = 1i * omega(Nsb+1) * jz0;
55 b = zeros(M * (2*Nsb+1), 1);
56 b((Nsb*M)+1 : (Nsb+1)*M, 1) = b0;
57
58 %% Sideband coupling
59 if (Nsb > 0)
60     delta_vec = reshape(mod_reg, M, 1);
```

```matlab
61          T_delta = spdiags(delta_vec, 0, M, M);
62          Cn_np = cell(2*Nsb, 1);
63          Cn_nm = cell(2*Nsb, 1);
64          for i = 1 : (2*Nsb)
65              Cn_np{i} = 1/2 * omega(i)^2 * T_delta * conj(T_phi);
66              Cn_nm{i} = 1/2 * omega(i+1)^2 * T_delta * T_phi;
67          end
68          A = sparse((2*Nsb+1)*M, (2*Nsb+1)*M);
69          A(1:M, 1:M) = A_i{1};
70          A(1:M, M+1:2*M) = Cn_np{1};
71          A(2*Nsb*M+1 : (2*Nsb+1)*M, 2*Nsb*M+1 : (2*Nsb+1)*M) = A_i{(2*Nsb+1)};
72          A(2*Nsb*M+1 : (2*Nsb+1)*M, (2*Nsb-1)*M+1 : 2*Nsb*M) = Cn_nm{2*Nsb};
73          for i = 2 : 2*Nsb
74              A((i-1)*M+1 : i*M, (i-1)*M+1 : i*M) = A_i{i};
75              A((i-1)*M+1 : i*M, (i-2)*M+1 : (i-1)*M) = Cn_nm{i-1};
76              A((i-1)*M+1 : i*M, i*M+1 : (i+1)*M) = Cn_np{i};
77          end
78  else
79      A(1:M, 1:M) = A_i{1};
80  end
81
82  %% Solve
83  if all(b==0)
84          ez = zeros(size(b));
85  else
86          ez = A\b;
87  end
88
89  %% Extract field values
90  Ez = cell(2*Nsb+1, 1);
91  Hx = cell(2*Nsb+1, 1);
92  Hy = cell(2*Nsb+1, 1);
93
94  for i = 1 : (2*Nsb+1)
95      Ez{i} = ez((i-1)*M + 1 : i*M, 1);
96      Hx{i} = -1/(1i*omega(i)) * u0^-1 * Syf{i}*Dyf * Ez{i};
97      Hy{i} = 1/(1i*omega(i)) * u0^-1 * Sxf{i}*Dxf * Ez{i};
98
99      Ez{i} = reshape(Ez{i}, N);
100     Hx{i} = reshape(Hx{i}, N);
101     Hy{i} = reshape(Hy{i}, N);
102 end
103 end
```

Bibliography

[1] C. Coulais, D. Sounas, and A. Alù, "Static non-reciprocity in mechanical meta-materials," *Nature*, vol. 542, no. 7642, pp. 461–464, 2017.

[2] L. Deák and T. Fülöp, "Reciprocity in quantum, electromagnetic and other wave scattering," *Annals of Physics*, vol. 327, no. 4, pp. 1050–1077, 2012.

[3] Buehler, "Characterizing earthquake location uncertainty in North America using source-receiver reciprocity and USArray," *Bulletin of the Seismological Society of America*, vol. 106, pp. 2395–2401, 2016.

[4] M. Scalerandi, C. L. E. Bruno, A. S. Gliozzi, and P. G. Bocca, "Break of reciprocity principle due to localized nonlinearities in concrete," *Ultrasonics*, vol. 52, no. 6, pp. 712–719, 2012.

[5] M. Scalerandi, A. S. Gliozzi, and C. L. E. Bruno, "Detection and location of cracks using loss of reciprocity in ultrasonic waves propagation," *The Journal of the Acoustical Society of America*, vol. 131, no. 1, EL81–85, 2012.

[6] C. Caloz and S. Tretyakov, "Nonreciprocal metamaterials: A global perspective," 2016, pp. 76–78.

[7] S. Hua, J. Wen, X. Jiang, Q. Hua, L. Jiang, and M. Xiao, "Demonstration of a chip-based optical isolator with parametric amplification," *Nature Communications*, vol. 7, p. 13 657, 2016.

[8] D. Huang, P. Pintus, C. Zhang, Y. Shoji, T. Mizumoto, and J. E. Bowers, "Electrically driven and thermally tunable integrated optical isolators for silicon photonics," *IEEE Journal on Selected Topics in Quantum Electronics*, vol. 22, no. 6, 2016.

[9] L. Bi, J. Hu, P. Jiang, H. S. Kim, D. H. Kim, M. C. Onbasli, G. F. Dionne, and C. A. Ross, "Magneto-optical thin films for on-chip monolithic integration of non-reciprocal photonic devices," *Materials*, vol. 6, no. 11, pp. 5094–5117, 2013.

[10] C. Doerr, L. Chen, and D. Vermeulen, "Tandem-phase-modulator-based optical isolator in silicon," *39th European Conference and Exhibition on Optical Communication (ECOC 2013)*, no. 1, pp. 1230–1232, 2013.

[11] C. R. Doerr, L. Chen, and D. Vermeulen, "Silicon photonics broadband modulation-based isolator.," *Optics express*, vol. 22, no. 4, pp. 4493–8, 2014.

[12] R. El-Ganainy, A. Eisfeld, M. Levy, and D. N. Christodoulides, "On-chip non-reciprocal optical devices based on quantum inspired photonic lattices," *Applied Physics Letters*, vol. 103, no. 16, 2013.

[13] L. Bi, J. Hu, P. Jiang, D. H. Kim, G. F. Dionne, L. C. Kimerling, and C. A. Ross, "On-chip optical isolation in monolithically integrated non-reciprocal optical resonators," *Nature Photonics*, vol. 5, no. December, pp. 758–762, 2011.

[14] J. D. Joannopoulos, P. R. Villeneuve, and S. Fan, "Photonic crystals: putting a new twist on light," *Nature*, vol. 386, no. 6621, pp. 143–149, 1997.

[15] D. S. Wiersma, "Disordered photonics," *Nature Photonics*, vol. 7, no. 3, pp. 188–196, 2013.

[16] R. J. Potton, "Reciprocity in optics," *Reports on Progress in Physics*, vol. 67, no. 5, p. 717, 2004.

[17] A. B. Khanikaev and A. Alù, "Silicon photonics: One-way photons in silicon," *Nature Photonics*, vol. 8, no. 9, pp. 680–682, 2014.

[18] F. Yilmaz, F. N. Ünal, and M. Ö. Oktel, "Evolution of the Hofstadter butterfly in a tunable optical lattice," *Physical Review A*, vol. 91, no. 6, p. 063 628, 2015.

[19] Z. Wang and S. Fan, "Suppressing the effect of disorders using time-reversal symmetry breaking in magneto-optical photonic crystals: An illustration with a four-port circulator," *Photonics and Nanostructures - Fundamentals and Applications*, vol. 4, no. 3, pp. 132–140, 2006.

[20] D. Jalas, A. Petrov, M. Eich, W. Freude, S. Fan, Z. Yu, R. Baets, M. Popović, A. Melloni, J. D. Joannopoulos, M. Vanwolleghem, C. R. Doerr, and H. Renner, "What is — and what is not — an optical isolator," *Nature Photonics*, vol. 7, no. 8, pp. 579–582, 2013.

[21] L. Feng, M. Ayache, J. Huang, Y.-L. Xu, M.-H. Lu, Y.-F. Chen, Y. Fainman, and A. Scherer, "Nonreciprocal Light Propagation in a Silicon Photonic Circuit," *Science*, vol. 333, no. 6043, pp. 729–733, 2011.

[22] F. Monticone and A. Alù, "Metamaterial, plasmonic and nanophotonic devices," *Reports on Progress in Physics*, vol. 80, no. 3, p. 036 401, 2017.

[23] K. Fang, Z. Yu, and S. Fan, "Realizing effective magnetic field for photons by controlling the phase of dynamic modulation," *Nature Photonics*, vol. 6, no. 11, pp. 782–787, 2012.

[24] P. Rabl, "Controlling photons with phonons: optomechanically induced non-reciprocity," *National Science Review*, nww074, 2016.

[25] Y. Shoji and T. Mizumoto, "Magneto-optical non-reciprocal devices in silicon photonics," *Science and Technology of Advanced Materials*, vol. 15, no. 1, p. 014 602, 2014.

[26] E. Li, B. J. Eggleton, K. Fang, and S. Fan, "Photonic Aharonov-Bohm effect in photon-phonon interactions," *Nature Communications*, vol. 5, p. 3225, 2014.

[27] J. Zaleśny, "Propagation of photons in resting and moving media," *Physical Review E*, vol. 63, no. 2, p. 026 603, 2001.

[28] L. D. Tzuang, K. Fang, P. a. Nussenzveig, S. Fan, and M. Lipson, "Observation of an effective magnetic field for light," *Cleo: 2014*, no. c, STu2M.3, 2014.

[29] J. Dalibard, "Introduction to the physics of artificial gauge fields," *arXiv:1504.05520 [cond-mat]*, 2015.

[30] J. Dalibard, F. Gerbier, G. Juzeliūnas, and P. Öhberg, "Colloquium: Artificial gauge potentials for neutral atoms," *Reviews of Modern Physics*, vol. 83, no. 4, pp. 1523–1543, 2011.

[31] S. Walter and F. Marquardt, "Classical dynamical gauge fields in optomechanics," *New Journal of Physics*, vol. 18, no. 11, 2016.

[32] Z. Yang, F. Gao, Y. Yang, and B. Zhang, "Strain-Induced Gauge Field and Landau Levels in Acoustic Structures," *Physical Review Letters*, vol. 118, no. 19, p. 194 301, 2017.

[33] M.-A. Miri, F. Ruesink, E. Verhagen, and A. Alù, "Optical Nonreciprocity Based on Optomechanical Coupling," *Physical Review Applied*, vol. 7, no. 6, p. 064 014, 2017.

[34] Z. Yang, F. Gao, X. Shi, and B. Zhang, "Synthetic-gauge-field-induced Dirac semimetal state in an acoustic resonator system," *New Journal of Physics*, vol. 18, no. 12, p. 125 003, 2016.

[35] K. Fang, *Creating effective magnetic field for photons : principles and applications*, 2013.

[36] S. Fan, Y. Shi, Z. Yu, Q. Lin, and L. Yuan, "Recent advances on non-reciprocal light manipulation from dynamic modulation," 2015, pp. 400–402.

[37] Z. Wang, Y. Chong, J. D. Joannopoulos, and M. Soljačić, "Observation of uni-directional backscattering-immune topological electromagnetic states," *Nature*, vol. 461, no. 7265, pp. 772–775, 2009.

[38] A. V. Poshakinskiy, A. N. Poddubny, L. Pilozzi, and E. L. Ivchenko, "Radia-tive topological states in resonant photonic crystals," *Physical Review Letters*, vol. 112, no. 10, 2014.

[39] M. C. Rechtsman, Y. Plotnik, J. M. Zeuner, D. Song, Z. Chen, A. Szameit, and M. Segev, "Topological Creation and Destruction of Edge States in Photonic Graphene," *Physical Review Letters*, vol. 111, no. 10, p. 103 901, 2013.

[40] S. Raghu and F. D. M. Haldane, "Analogs of quantum-Hall-effect edge states in photonic crystals," *Physical Review A - Atomic, Molecular, and Optical Physics*, vol. 78, no. 3, 2008.

[41] S. Barik, H. Miyake, W. Degottardi, E. Waks, and M. Hafezi, "Two-dimensionally confined topological edge states in photonic crystals," *New Journal of Physics*, vol. 18, no. 11, 2016.

[42] W.-J. Chen, S.-J. Jiang, X.-D. Chen, B. Zhu, L. Zhou, J.-W. Dong, and C. T. Chan, "Experimental realization of photonic topological insulator in a uniaxial metacrystal waveguide," *Nature Communications*, vol. 5, p. 5782, 2014.

[43] Y. Lumer, Y. Plotnik, M. C. Rechtsman, and M. Segev, "Self-localized states in photonic topological insulators," *Physical Review Letters*, vol. 111, no. 24, 2013.

[44] Y. Zhang, Z. Wu, M. R. Beli?? H. Zheng, Z. Wang, M. Xiao, and Y. Zhang, "Pho-tonic Floquet topological insulators in atomic ensembles," *Laser and Photonics Reviews*, vol. 9, no. 3, pp. 331–338, 2015.

[45] D. Leykam, M. C. Rechtsman, and Y. D. Chong, "Anomalous Topological Phases and Unpaired Dirac Cones in Photonic Floquet Topological Insulators," *Physical Review Letters*, vol. 117, no. 1, 2016.

[46] L. J. Maczewsky, J. M. Zeuner, S. Nolte, and A. Szameit, "Observation of pho-tonic anomalous Floquet Topological Insulators," *Arxiv preprint*, vol. 8, pp. 1–7, 2016.

[47] A. B. Khanikaev, S. H. Mousavi, W.-K. Tse, M. Kargarian, A. H. MacDonald, and G. Shvets, "Photonic topological insulators.," *Nature materials*, vol. 12, no. 3, pp. 233–9, 2013.

[48] T. Ozawa, H. M. Price, N. Goldman, O. Zilberberg, and I. Carusotto, "Synthetic dimensions in integrated photonics: From optical isolation to four-dimensional quantum Hall physics," *Physical Review A*, vol. 93, no. 4, p. 043 827, 2016.

[49] R. O. Umucalılar and I. Carusotto, "Artificial gauge field for photons in coupled cavity arrays," *Physical Review A*, vol. 84, no. 4, p. 043 804, 2011.

[50] W. Bogaerts, P. De Heyn, T. Van Vaerenbergh, K. De Vos, S. Kumar Selvaraja, T. Claes, P. Dumon, P. Bienstman, D. Van Thourhout, and R. Baets, "Silicon microring resonators," *Laser & Photonics Reviews*, vol. 6, no. 1, pp. 47–73, 2012.

[51] K. Fang, Z. Yu, and S. Fan, "Photonic Aharonov-Bohm Effect Based on Dynamic Modulation," *Physical Review Letters*, vol. 108, no. 15, p. 153 901, 2012.

[52] Y. Aharonov and D. Bohm, "Significance of Electromagnetic Potentials in the Quantum Theory," *Physical Review*, vol. 115, no. 3, pp. 485–491, 1959.

[53] R. G. Chambers, "Shift of an Electron Interference Pattern by Enclosed Magnetic Flux," *Physical Review Letters*, vol. 5, no. 1, pp. 3–5, 1960.

[54] K. Fang, Z. Yu, and S. Fan, "Experimental demonstration of a photonic Aharonov-Bohm effect at radio frequencies," *Physical Review B*, vol. 87, no. 6, p. 060 301, 2013.

[55] K. Fang and S. Fan, "Controlling the Flow of Light Using the Inhomogeneous Effective Gauge Field that Emerges from Dynamic Modulation," *Physical Review Letters*, vol. 111, no. 20, p. 203 901, 2013.

[56] F. D. M. Haldane and S. Raghu, "Possible Realization of Directional Optical Waveguides in Photonic Crystals with Broken Time-Reversal Symmetry," *Physical Review Letters*, vol. 100, no. 1, p. 013 904, 2008.

[57] Q. Lin and S. Fan, "Resonator-free realization of effective magnetic field for photons," *New Journal of Physics*, vol. 17, no. 7, p. 075 008, 2015.

[58] Z. Wang, Y. Chong, J. D. Joannopoulos, and M. Soljačić, "Observation of unidirectional backscattering-immune topological electromagnetic states.," *Nature*, vol. 461, no. 7265, pp. 772–5, 2009.

[59] W.-R. Lee and W.-K. Tse, "Dynamical Quantum Anomalous Hall Effect in Strong Optical Fields," *arXiv:1703.00510 [cond-mat]*, 2017.

[60] M. Vieira, A. M. d. M. Carvalho, and C. Furtado, "Aharonov-Bohm effect for light in a moving medium," *Physical Review A*, vol. 90, no. 1, p. 012 105, 2014.

[61] U. Leonhardt and P. Piwnicki, "Optics of Nonuniformly Moving Media," *Physical Review A*, vol. 60, no. 6, pp. 4301–4312, 1999.

[62] ——, "Light in moving media," *Contemporary Physics*, vol. 41, no. 5, pp. 301–308, 2000.

[63] U. Leonhardt, "Relativistic Effects of Light in Moving Media with Extremely Low Group Velocity," *Physical Review Letters*, vol. 84, no. 5, pp. 822–825, 2000.

[64] D. A. Genov, "General relativity: Optical black-hole analogues," *Nature Photonics*, vol. 5, no. 2, pp. 76–78, 2011.

[65] L. D. Tzuang, K. Fang, P. Nussenzveig, S. Fan, and M. Lipson, "Non-reciprocal phase shift induced by an effective magnetic flux for light," *Nature Photonics*, vol. 8, no. 9, pp. 701–705, 2014.

[66] M. C. Rechtsman, J. M. Zeuner, Y. Plotnik, Y. Lumer, D. Podolsky, F. Dreisow, S. Nolte, M. Segev, and A. Szameit, "Photonic Floquet topological insulators," *Nature*, vol. 496, no. 7444, pp. 196–200, 2013.

[67] N. H. Lindner, G. Refael, and V. Galitski, "Floquet topological insulator in semiconductor quantum wells," *Nature Physics*, vol. 7, no. 6, pp. 490–495, 2011.

[68] S. Fedortchenko, S. Huppert, A. Vasanelli, Y. Todorov, C. Sirtori, C. Ciuti, A. Keller, T. Coudreau, and P. Milman, "Output squeezed radiation from dispersive ultrastrong light-matter coupling," *Physical Review A*, vol. 94, no. 1, p. 013 821, 2016.

[69] M. Hirokawa, J. S. Møller, and I. Sasaki, "A mathematical analysis of dressed photon in ground state of generalized quantum Rabi model using pair theory," *Journal of Physics A: Mathematical and Theoretical*, vol. 50, no. 18, p. 184 003, 2017.

[70] L. Yuan and S. Fan, "Topologically nontrivial Floquet band structure in a system undergoing photonic transitions in the ultrastrong-coupling regime," *Physical Review A*, vol. 92, no. 5, p. 053 822, 2015.

[71] S.-C. Zhang and J. Hu, "A Four-Dimensional Generalization of the Quantum Hall Effect," *Science*, vol. 294, no. 5543, 2001.

[72] H. M. Price, T. Ozawa, and N. Goldman, "Synthetic dimensions for cold atoms from shaking a harmonic trap," *Physical Review A*, vol. 95, no. 2, p. 023 607, 2017.

[73] T. Y. Saito and S. Furukawa, "Devil's staircases in synthetic dimensions and gauge fields," *Physical Review A*, vol. 95, no. 4, p. 043 613, 2017.

[74] S. Barbarino, L. Taddia, D. Rossini, L. Mazza, and R. Fazio, "Synthetic gauge fields in synthetic dimensions: interactions and chiral edge modes," *New Journal of Physics*, vol. 18, no. 3, p. 035 010, 2016.

[75] B. K. Stuhl, H.-I. Lu, L. M. Aycock, D. Genkina, and I. B. Spielman, "Visualizing edge states with an atomic Bose gas in the quantum Hall regime," *Science*, vol. 349, no. 6255, 2015.

[76] O. Boada, A. Celi, M. Lewenstein, and J. I. Latorre, "Quantum simulation of an extra dimension," *Physical Review Letters*, vol. 108, no. 13, pp. 2–7, 2011.

[77] M. Ła,cki, H. Pichler, A. Sterdyniak, A. Lyras, V. E. Lembessis, O. Al-Dossary, J. C. Budich, and P. Zoller, "Quantum Hall Physics with Cold Atoms in Cylindrical Optical Lattices," *Physical Review A*, vol. 93, no. 1, 2015.

[78] T.-S. Zeng, C. Wang, and H. Zhai, "Charge Pumping of Interacting Fermion Atoms in the Synthetic Dimension," *Physical Review Letters*, vol. 115, no. 9, 2015.

[79] L. Yuan, Y. Shi, and S. Fan, "Achieving the gauge potential for the photon in a synthetic space," 2016, pp. 1–2.

[80] C. Qin, F. Zhou, Y. Peng, H. Chen, X. Zhu, B. Wang, J. Dong, X. Zhang, and P. Lu, "Frequency manipulation of light by photonic gauge potentials," *arXiv:1705.07296 [physics]*, 2017.

[81] S. Gupta, R. Juneja, R. Shinde, and A. K. Singh, "Topologically nontrivial electronic states in CaSn 3," *Journal of Applied Physics*, vol. 121, no. 21, p. 214 901, 2017.

[82] B. Z. Spivak and A. V. Andreev, "Magnetotransport phenomena related to the chiral anomaly in Weyl semimetals," *Physical Review B*, vol. 93, no. 8, 2016.

[83] J. Noh, S. Huang, D. Leykam, Y. D. Chong, K. P. Chen, and M. C. Rechtsman, "Experimental observation of optical Weyl points and Fermi arc-like surface states," *Nature Physics*, vol. 13, no. 6, pp. 611–617, 2017.

[84] M. Xiao, Q. Lin, and S. Fan, "Hyperbolic Weyl Point in Reciprocal Chiral Metamaterials," *Physical Review Letters*, vol. 117, no. 5, p. 057 401, 2016.

[85] Z. Yang and B. Zhang, "Acoustic Type-II Weyl Nodes from Stacking Dimerized Chains," *Physical Review Letters*, vol. 117, no. 22, 2016.

[86] W. Gao, B. Yang, M. Lawrence, F. Fang, B. Béri, and S. Zhang, "Photonic Weyl degeneracies in magnetized plasma," *Nature Communications*, vol. 7, no. May, p. 12 435, 2016.

[87] Q. Lin, M. Xiao, L. Yuan, and S. Fan, "Photonic Weyl Point in a 2D Resonator Array with a Synthetic Frequency Dimension," *Conference on Lasers and Electro-Optics*, Washington, D.C.: OSA, 2017, FM3G.5.

[88] L. Lu, Z. Wang, D. Ye, L. Ran, L. Fu, J. D. Joannopoulos, and M. Soljačić, "Experimental observation of Weyl points," *Science*, vol. 349, no. 6248, 2015.

[89] M. C. Rechtsman, J. M. Zeuner, A. Tünnermann, S. Nolte, M. Segev, and A. Szameit, "Strain-induced pseudomagnetic field and photonic Landau levels in dielectric structures," *Nature Photonics*, vol. 7, no. 2, pp. 153–158, 2013.

[90] H. M. Price, O. Zilberberg, T. Ozawa, I. Carusotto, and N. Goldman, "Four-Dimensional Quantum Hall Effect with Ultracold Atoms," *Physical Review Letters*, vol. 115, no. 19, p. 195 303, 2015.

[91] M. Hafezi, S. Mittal, J. Fan, A. Migdall, and J. Taylor, "Imaging topological edge states in silicon photonics," *Nature Photonics*, vol. 7, no. 12, pp. 1001–1005, 2013.

[92] M. Mansuripur and A. R. Zakharian, "Maxwell's macroscopic equations, the energy-momentum postulates, and the Lorentz law of force," *Physical Review E*, vol. 79, no. 2, 2009.

[93] J. J. Sakurai, *Modern Quantum Mechanics, Revised Edition*, 1. 1995, vol. 63, p. 93.

[94] J. N. Winn, S. Fan, J. D. Joannopoulos, and E. P. Ippen, "Interband transitions in photonic crystals," *Physical Review B*, vol. 59, no. 3, pp. 1551–1554, 1999.

[95] Z. Yu and S. Fan, "Complete optical isolation created by indirect interband photonic transitions," *Nature Photonics*, vol. 3, no. 2, pp. 91–94, 2009.

[96] F. Halzen, *Quarks and Leptons: An Introductory Course in Modern Particle Physics*, 1985.

[97] A. T. Paxton, "An Introduction to the Tight Binding Approximation – Implementation by Diagonalisation," *Methods*, vol. 42, pp. 145–176, 2009.

[98] TU Delft, *Tight-binding models in a magnetic field: Peierls substitution*, 2014.

[99] N. J. Champagne, J. G. Berryman, and H. Buettner, "FDFD: A 3D Finite-Difference Frequency-Domain Code for Electromagnetic Induction Tomography," *Journal of Computational Physics*, vol. 170, no. 2, pp. 830–848, 2001.

[100] K. S. Yee, "Numerical solution of initial boundary value problems involving Maxwell's equations in isotropic media," *IEEE Transactions on Antennas and Propagation*, vol. 14, no. 3, pp. 302–307, 1966.

[101] A. Taflove and S. C. Hagness, *Computational Electrodynamics: The Finite-Difference Time-Domain Method, Third Edition*. 2005, p. 1038.

[102] J.-P. Berenger, "A perfectly matched layer for the absorption of electromagnetic waves," *Journal of Computational Physics*, vol. 114, no. 2, pp. 185–200, 1994.

[103] F. Rana, *ECE303 Electromagnetic Fields and Waves*, 2017.

[104] S. Johnson and J. Joannopoulos, "Block-iterative frequency-domain methods for Maxwell's equations in a planewave basis," *Optics Express*, vol. 8, no. 3, p. 173, 2001.

[105] W. Shin and S. Fan, "Choice of the perfectly matched layer boundary condition for frequency-domain Maxwell's equations solvers," *Journal of Computational Physics*, vol. 231, no. 8, pp. 3406–3431, 2012.

[106] Y. Shi, W. Shin, and S. Fan, "Multi-frequency finite-difference frequency-domain algorithm for active nanophotonic device simulations," *Optica*, vol. 3, no. 11, p. 1256, 2016.

[107] B.-T. Lee and S.-Y. Shin, "Mode-order converter in a multimode waveguide.," *Optics letters*, vol. 28, no. 18, pp. 1660–2, 2003.

[108] Y. Jiao, S. Fan, and D. A. B. Miller, *Demonstration of systematic photonic crystal device design and optimization by low-rank adjustments: an extremely compact mode separator*, 2005.

[109] G. T. Reed, G. Mashanovich, F. Y. Gardes, and D. J. Thomson, "Silicon optical modulators," *Nature Photonics*, vol. 4, no. 8, pp. 518–526, 2010.

[110] F. Gao, Y. Wang, G. Cao, X. Jia, and F. Zhang, "Reduction of sidewall roughness in silicon-on-insulator rib waveguides," *Applied Surface Science*, vol. 252, no. 14, pp. 5071–5075, 2006.

[111] F. Ren, S. J. Pearton, J. R. Lothian, C. R. Abernathy, and W. S. Hobson, "Reduction of sidewall roughness during dry etching of SiO2," *Journal of Vacuum Science & Technology B: Microelectronics and Nanometer Structures*, vol. 10, no. 6, p. 2407, 1992.

[112] A. F. Oskooi, D. Roundy, M. Ibanescu, P. Bermel, J. D. Joannopoulos, and S. G. Johnson, "Meep: A flexible free-software package for electromagnetic simulations by the FDTD method," *Computer Physics Communications*, vol. 181, no. 3, pp. 687–702, 2010.

[113] R. E. Bank and T. F. Chan, "An analysis of the composite step biconjugate gradient method," *Numerische Mathematik*, vol. 66, no. 1, pp. 295–319, 1993.

[114] R. W. Freund and N. M. Nachtigal, "QMR: a quasi-minimal residual method for non-Hermitian linear systems," *Numerische Mathematik*, vol. 60, no. 1, pp. 315–339, 1991.